SYNTHESIS, GROWTH, SELF-ASSEMBLY AND PHOTOCATALYTIC PROPERTIES OF TIO_2 NANOPARTICLES PREPARED WITH

Barbara Horvat

Doctoral Dissertation
Jožef Stefan International Postgraduate School
Ljubljana, Slovenia, June 2013

Evaluation Board:

Assist. Prof. Dr. Saša Novak Krmpotič, Chairman, Jožef Stefan Institute, Jamova 39, 1000 Ljubljana, Slovenia

Assist. Prof. Dr. Srečo D. Škapin, Member, Jožef Stefan Institute, Jamova 39, 1000 Ljubljana, Slovenia

Dr. Andreja Gajović, Member, Ruđer Bošković Institute, Bijenička 54, Zagreb, Croatia

MEDNARODNA PODIPLOMSKA ŠOLA JOŽEFA STEFANA
JOŽEF STEFAN INTERNATIONAL POSTGRADUATE SCHOOL

Barbara Horvat

SYNTHESIS, GROWTH, SELF-ASSEMBLY AND PHOTOCATALYTC PROPERTIES OF TiO_2 NANOPARTICLES PREPARED WITH A HYDROTHERMAL ROUTE

Doctoral Dissertation

SINTEZA, RAST, SAMOUREJANJE IN FOTOKATALITSKE LASTNOSTI TiO_2 NANODELCEV PRIPRAVLJENIH S HIDROTERMALNO SINTEZO

Doktorska disertacija

Supervisor: Assist. Prof. Dr. Goran Dražić

Ljubljana, Slovenia, June 2013

Index

Abstract

The consumption of clean, drinkable water grows with the increasing number of the world's population, consequently also the amount of waste and grey water is increased. As the need for clean, drinkable water increases and its supplies are limited and reducing, it is reasonable to recycle grey water to the point where it would be useful at least for showering, washing dishes and clothes, re-flushing toilets, maybe even for drinking. It is also necessary to clean waste water from toxic substances that are harmful to humans and to the environment.

The perfect solution is a green house where TiO_2 would be built in the exterior of the house, mainly as a photocatalyst in the anatase crystal form. Photocatalytic TiO_2 degrades bonds in hazardous organic compounds and turns them into less or even non-hazardous compounds. Surfaces coated with TiO_2 can become superhydrophilic after radiation with light, i.e. selfcleaning with rain, which reduces the use of other cleaning chemicals.

We used various types of synthesises for preparation of photocatalytic titania, from sol-gel, hydrothermal, solvothermal synthesis, to calcination. We prepared different TiO_2 nanomaterials, followed their growth and assembly. We observed and explained for the first time the non-ideal growth of nanoanatase bipyramids. We were also the first who published 3D reconstruction from HRTEM micrographs of the growing titania crystals, where intermediate morphologies are asymmetrical most probably due to local nonequilibrium conditions inside the autoclave vessel. These crystals showed relatively good photocatalytic activity.

With self-assembly of synthesised nanoparticles in glycerol we prepared for the first time amorphous μ-sized flower-like structures growing in the geodes, while in the literature at comparable conditions they always got crystalline material. Because of the flower-like material sedimented fast, that suggests that it can be easily removed from water.

We were also first who used assisted assembly to enrich amorphous μ-sized flower-like structures with nanoanatase crystals and at the same time created bulk material full of μ-pores consisted of nanoanatase which give the bulk structure ~3-times bigger BET specific surface area when compared to commercial powder P25.

Povzetek

Z naraščanjem svetovne populacije raste poraba čiste, pitne vode, s tem seveda tudi količina odpadne in sive vode. Ker je tudi potreba po čisti, pitni vodi vedno večja, zaloge le-te pa omejene in v zmanjševanju, je smotrno reciklirati sivo vodo do točke, ko bo vsaj uporabna za tuširanje, pranje posode in perila, vnovično splakovanje v straniščih, če ne celo za pitje. Ravno tako je potrebno onesnaženo vodo očistiti strupenih snovi, nevarnih tako za človeka kot za okolje.

Odlična rešitev je zelena hiša kjer bi bil TiO_2 vgrajen v zunanjost hiše predvsem kot fotokatalizator v anatazni obliki, saj s pomočjo sonca razgradi vezi nevarnih organskih spojin in jih spremeni v manj ali celo nenevarne spojine. Površine premazane s TiO_2 postanejo po obsevanju s svetlobo lahko tudi superhidrofilne, torej samočistilne s pomočjo dežja, kar pa zmanjša porabo ostalih kemikalij namenjenih čiščenju.

Uporabili smo vrsto različnih sintez za pripravo fotokatalitičnega titanovega dioksida. Vse od sol-gel, hidrotermalne, solvotermalne sinteze, pa do žganja. Pripravili smo več različnih TiO_2 nanomaterialov, sledili njihovo rast ter urejanje. Prvi smo opazili in razložili neidealno rast nanoanataznih bipiramid. Prav tako smo bili prvi, ki smo objavili 3D rekonstrukcijo iz HRTEM slik rastočih TiO_2 kristalov, kjer so vmesne morfologije asimetrične, kar je po vsej verjetnosti posledica neravnovesnih pogojev znotraj reakcijske posode v avtoklavu. Ti kristali so pokazali relativno dobro fotokatalitsko aktivnost.

S pomočjo samourejanja v glicerolu smo prvi pripravili mikronske strukture rastoče v geodah v obliki rožic, medtem ko so v literaturi pri podobnih pogojih vedno dobili kristaliničen material. Rožast material se je hitro posedel, po čemer sklepamo, da je lahko odstranljiv iz vode.

Bili smo tudi prvi, ki smo s pomočjo vsiljenega urejanja dodali dodano vrednost amorfnemu mikronskemu rožastemu materialu, ki smo ga fotokatalitsko obogatili z nanoanataznimi kristali, in hkrati naredili mikro-porozne milimetrske-aglomerate sestavljene iz 100 nm velikih agregatov, ki so sestavljeni iz 10 nm anataznih kristalov. Rožast in porozni material sta imela skupaj ~3-krat večjo specifično površino BET v primerjavi s P25, ki je dostopen na tržišču in velja za referenco glede fotokatalitičnih lastnosti materialov.

Abbreviations

α	=	angle in the unit cell between a and b edges of the unit cell
α	=	absorption coefficient in band gap measurements
β	=	angle in the unit cell between a and c edges of the unit cell
γ	=	angle in the unit cell between b and c edges of the unit cell
γ_j	=	specific surface free energy of the j-th crystal face
Γ	=	Γ–point is the centre of the crystal in reciprocal space
ΔG_{SA}	=	Gibbs free energy
ΔG_i	=	Gibbs free energy of the i-th crystal
ΔH_{SA}	=	enthalpy change
Δm_j	=	mass of the caffeine sampled on the j-th step
Δm_j^D	=	mass of the degraded caffeine with photocatalysis before j-th
ΔS_{SA}	=	entropy change
ΔV	=	volume of the photocatalytically tested sample taken for analysis
ΔV_{izh_j}	=	volume of the evaporated distilled water on the j-th step
λ	=	wavelength of the light
ν	=	frequency of the light
ω	=	angular momentum
ρ	=	mass density
θ	=	Braggs angle
a	=	"x" edge of the unit cell
$\mathbf{a}_i$	=	unit cell vectors in the real space, vectors of the Bravais lattice
$A(\lambda)$, $A(\hbar\omega)$	=	absorbance spectrum
APW	=	augmented plane wave method to calculate the band gap
ATR	=	attenuated total reflectance
b	=	"y" edge of the unit cell
B	=	line broadening at half of the maximum intensity
BET	=	Brunauer–Emmett–Teller theory to determine specific surface area
$\mathbf{b}_i$	=	vectors of the reciprocal lattice
c	=	"z" edge of the unit cell
c_N^A	=	concentration of the resazurin after N-th sampling (photolysis)
c_N^B	=	concentration of the caffeine before N-th sampling (photolysis)
C_N^A	=	concentration of the caffeine after N-th (photocatalysis)
C_N^B	=	concentration of the caffeine before N-th sampling (photocatalysis)
d	=	average size of the crystals
d_1	=	diameter of crystallites building up the flower-like structure
d_2	=	diameter of the crystals on the surface of the flower-like structure
d_3	=	diameter of crystals in surroundings of the flower-like structure
d_a	=	aggregate size building up the porous material
d_b	=	crystal size building up the aggregate
d_{hkl}	=	spacing between planes
D	=	diameter of flower-like structure
D_p	=	pore's diameter
DFT	=	density-functional theory for calculating the band gap

DLS	=	Dynamic Light Scattering
e^-	=	electron
E	=	electric field
E_g	=	energy of the band gap
EDXS	=	Energy-Dispersive X-ray Spectroscopy
SAED	=	electron-diffraction pattern
EHMOC	=	extended Hückler molecular orbital calculations for the band gap
f_j	=	atomic factor
f_O	=	atomic factor of O
f_{Ti}	=	atomic factor of Ti
FEGSEM	=	Field Emission Gun Scanning Electron Microscope
FFT	=	fast Fourier transform
FTIR	=	Fourier transform Infrared Spectroscopy
G_0W_0	=	a full-frequency-dependent scheme for calculating the band gap
h	=	Planck's constant, $6.626\ 10^{-34}$ J=$4.135\ 10^{-15}$ eV
ħ	=	reduced Plancks constant, $1.054\ 10^{-34}$ Js=$6.582\ 10^{-16}$ eVs
h^+	=	hole
h_j	=	central distance of the j-th crystal face
h, k, l	=	Miller index representing planes in the real space of the crystal
HRTEM	=	High Resolution Transmission Electron Microscope
HSE06	=	Heyd, Scuseria and Ernzerhof method to calculate the band gap
HT	=	hydrothermal
I4(1)/amd	=	space group of the anatase
K	=	Scherrer constant, shape factor, 0.89
K	=	reciprocal vector
k-space	=	reciprocal space
KKR	=	Korriga, Kahn and Rostoker method to calculate the band gap
KS	=	Kohn-Sham method to calculate the band gap
L	=	length of flower-like structure's leaf
L_p	=	pore's length
m_0	=	mass of the caffeine before photolysis/photocatalysis
m_1, m_2, m_3	=	integers in the reciprocal lattice
n	=	refractive index
OPW	=	orthogonalized plane wave method
P25	=	commercial TiO_2 powder used from photocatalytic comparison
P4(2)/mnm	=	space group of the rutile
PBE	=	Perdew, Burke and Ernzerhof method to calculate the band gap
QP	=	quasiparticle corrections to calculate the band gap
$\mathbf{r}_j$	=	basis vector of an ion in the unit cell
S	=	structure factor
S_j	=	surface of the j-th crystal face
SA	=	self-assembly
SAED	=	selected area electron diffraction
SCOLCAO	=	self-consistent orthogonalized linear combination of atomic orbitals for the band gap
SEM	=	Scanning Electron Microscope
ST	=	solvothermal
TEM	=	Transmission Electron Microscope
TiO_2	=	Titanium dioxide, Titania
TiO_2(II)	=	one of the crystal modifications of TiO_2
TiO_2(R)	=	one of the crystal modifications of TiO_2

TiO_2(H)	=	one of the crystal modifications of TiO_2
TiO_2(R)	=	one of the crystal modifications of TiO_2
TiO_2-OI	=	one of the crystal modifications of TiO_2
TiO_2-OII	=	one of the crystal modifications of TiO_2
T_m	=	temperature of the melting point
T_t	=	transformation temperature of the crystal modifications of TiO_2
TO	=	Titanium (IV) Isopropoxide
u	=	distance parameter
U_i	=	Whyckoff site
UV	=	Ultra violet light
V	=	unit cell volume
V_0	=	volume of the solution before photolysis/photocatalysis sampling
Vis	=	visible part of light spectrum
W	=	width of flower-like structure's leaf
W_g	=	band gap
W_S	=	surface energy of the crystal's plane
XRD	=	X-Ray Diffraction
Z	=	number of Ti atoms in the unit cell

1 Introduction

Number of world's population is more than 7 billion and rapidly growing[1], while the amount of clean, drinkable water is now just 1 % of all earth's water and reducing[2]. Usage of and need for the water is growing with the world's population, so is the amount of waste and grey waters. The only solution in this situation is to clean the waste and grey water from harmful ingredients and use the same water again. Water and air purification can be done with photocatalytic titanium dioxide.

Titanium dioxide, also known as titanium (IV) oxide or titania, is the naturally occurring oxide of titanium with chemical formula TiO_2. It is also known as a pigment, called titanium white, Pigment White 6 or CI 77891 and as food additive E171. This oxide is not used and studied just because of use in the food industry or as wall paint, but also because of its extensive use on many other areas: besides photocatalysis it is used also for solar energy conversion, sensors, mesophorous membranes, cosmetics, medicine etc.

In nature TiO_2 was found so far in 5 different crystal modifications: as anatase, brookite, rutile, on the rutile's twin boundaries as α-PbO_2 type TiO_2(II)[3,4], and as baddeleyite-like TiO_2(III)[5,6]. All 5 were synthesised in the laboratory, TiO_2(II) and TiO_2(III) just under high-pressure[7]. Till now there were even 7 more crystal modifications synthesised in the laboratory: TiO_2(B)[8], hollandite-like TiO_2(H)[9], ramsdellite-like TiO_2(R)[10], TiO_2(OI)[11], cubic TiO_2[12], $PbCl_2$ type TiO_2(OII)[13]. For detailed data on TiO_2 crystals[14,15], their symmetries, unit cell parameters, see Table 1.

Table 1: *Crystallographic properties of TiO_2 crystals*. Till now 11 TiO_2 crystal-types were found in nature or synthesized in the laboratory. The majority are high pressure phases, except from rutile, anatase and brookite. a, b, c and β represent unit cell parameters.

Crystal	structure	symmetry	space group	a [Å]	b [Å]	c [Å]	β [°]
rutile		tetragonal	$P4_2/mnm$	4.594	4.594	2.958	
anatase		tetragonal	$I4_1/amd$	3.785	3.785	9.514	
brookite		orthorhombic	Pbca	9.184	5.447	5.145	
TiO_2(B)		monoclinic	C_2/m	12.18	3.741	6.525	107.29
TiO_2(H)	hollandite	tetragonal	I4/m	10.18	10.18	2.996	
TiO_2(R)	ramsdellite	orthorhombic	Pbnm	4.901	9.453	2.958	
TiO_2(II)	columbite	orthorhombic	Pbcn	4.61	5.43	4.87	
TiO_2(III)	baddeleyite	monoclinic	$P2_1/c$	4.65	4.93	4.96	99.2
TiO_2	fluorite	cubic	Fm3m	4.516	4.516	4.516	
TiO_2(OI)	pyrite	orthorhombic	Pa3	4.86	/	/	
TiO_2(OII)	cotunnite	orthorhombic	Pnma	5.163	2.989	5.966	

The most studied crystal modifications are rutile and anatase, followed by brookite, which is very hard to synthesise as a pure form[16]. All other crystals are even harder to synthesise as they are high-pressure forms.

1.1 Crystal modifications of TiO_2

Among all 11 crystal modifications of TiO_2 we have synthesized just anatase, brookite and rutile.

Rutile is usually prismatic, often slender to acicular, rarely pyramidal. As bulk, it was found in several different colours, i.e. as reddish brown, red, pale yellow, pale blue, violet, rarely grass-green and black. As powder, rutile is usually white. The streak, i.e. the trace left on the surface by the crystal, is greyish black, pale brown, light yellow. Twinning is common on {011}, or {031} planes.[17]

Anatase is commonly acute bipyramidal, see Figure 1a and b, with outer {011} planes, obtuse pyramidal or tabular on {001} planes, less typically prismatic in [001] direction, with {110}, {010} outer planes. As bulk crystal in nature it was found in several colours, i.e. in brown, pale yellow or reddish brown, indigo, black, see Figure 1a and b, pale green, pale lilac, grey, rarely nearly colourless, brown, yellow-brown, pale green and blue. As powder, anatase is usually white, see Figure 1c. The streak it leaves on the surface is white to pale yellow. Twinning is rare and it is on {112} planes.[17]

Brookite is usually tabular on {010} planes, striated parallel in [001] direction and elongated, pyramidal with {111} outer planes, pseudohexagonal with equally developed outer planes {120} and {111}, prismatic in [001] direction with prominent outer plane {120}, rarely tabular with {001} as outer planes. As bulk crystal, it was found in several colours, i.e. in brown, yellowish brown, reddish brown, dark brown to iron-black, yellowish brown to dark brown. As powder, it is usually white. Its streak is white to greyish white or yellowish white. Twinning is not certain on {120}.[17]

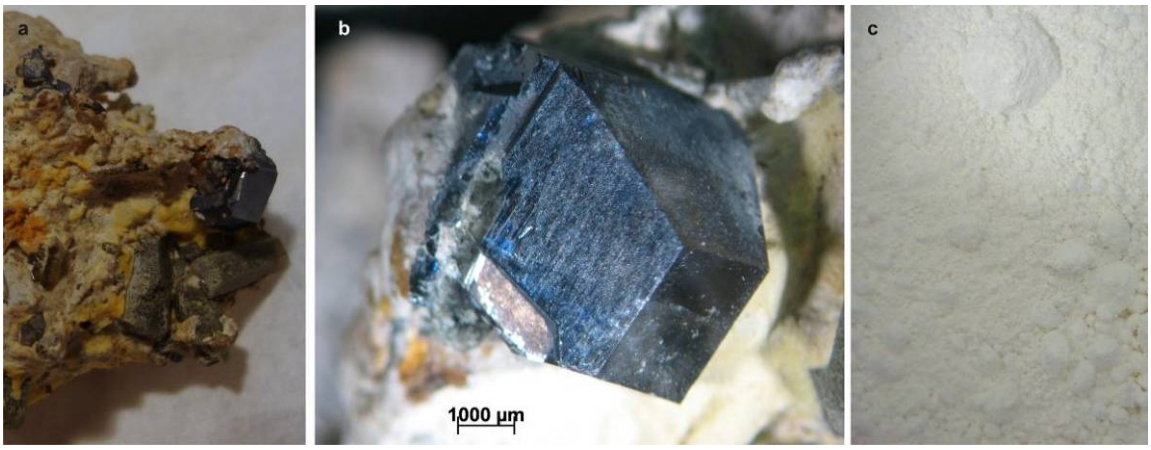

Figure 1: *Anatase as bulk and as powder*. a, b) Anatase in nature is usually in bipyramidal form, with well expressed {011} planes, as also {001} planes. Here it is shown in black colour; we used modular stereo microscope Stereo Discovery.V8, from Zeiss. c) Anatase in powder form is usually white.

Rutile (see Table 1) crystallises in tetragonal unit cell, with point group D_{4h} (dihedral non Abelian group which contains 4-fold rotational axis perpendicular to the 2-folded primary rotational axis, and mirror plane perpendicular to the 4-fold axes), in the space group $P4_2/mnm$ (4/mmm), and is the smallest among all 3 prepared titania, with only 9 titanium and 6 oxygen atoms, see Figure 2.

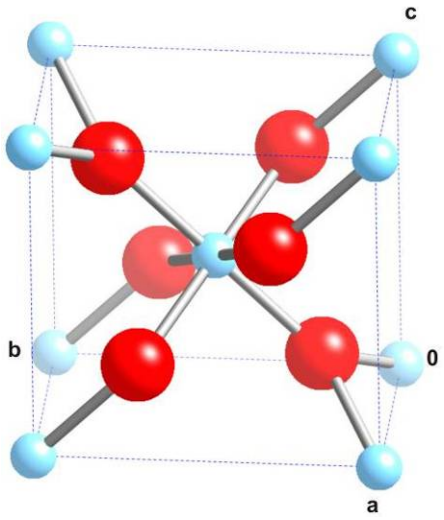

Figure 2: *Unit cell of the rutile*. Tetragonal unit cell of the most common TiO_2 crystal, rutile. Red spheres represent O atoms, blue spheres Ti atoms. Axes are labeled by unit cell parameters: a (for x), b (for -y), c (for z). 0 represents the centre of the coordinate system.

Titanium atoms are building a body-centred tetragonal unit cell, while all 6 oxygen atoms are between the unit cell's centre and all 6 corners. Unit cell parameters used in the thesis are[15] a=b=4.59373 Å, c=2.95815 Å, angles α=β=γ=90 °, number of Ti atoms in the unit cell Z=2, unit cell volume V=62.423 Å, mass density ρ=4.249 g/m^3, Whyckoff sites for Ti are $U_x=U_y=U_z=0$, and for O are $U_x=U_y=0.3053$ Å, $U_z=0$. We have simplified the results of the atoms' coordinates which can be calculated from Whyckoff sites and space group symmetry, with defining new distance parameter u=0.894 Å. The simplified atoms' coordinates are listed in Table 2.

Table 2: *Positions of the rutile atoms*. We wrote position of the rutile atoms with 4 unit cell parameters: a=b=4.59373 Å, c=2.95815 Å, u=0.894 Å.

Element	x [Å]	y [Å]	z [Å]
O	a/2-u	a/2-u	0
O	a/2+u	a/2+u	0
O	a-u	u	c/2
O	u	a-u	c/2
O	a/2-u	a/2-u	c
O	a/2+u	a/2+u	c
Ti	0	0	0
Ti	a/2	a/2	c/2
Ti	a	0	0
Ti	0	a	0
Ti	a	a	0
Ti	0	0	c
Ti	a	0	c
Ti	0	a	c
Ti	a	a	c

Anatase (see Table 1), same as the rutile, crystallises in the tetragonal unit cell, with point group D_{4h}. Its space group is $I4_1/amd$ (4/mmm), unit cell bigger than the rutile, with 13 titanium and 18 oxygen atoms, see Figure 3.

Titanium atoms are building a face-centred tetragonal unit cell with a base. Unit cell

parameters used in the thesis are[15] a=b=3.7845 Å, c=9.5143 Å, angles α=β=γ=90 º, number of Ti atoms in the unit cell Z=4, unit cell volume V=136.268 Å, mass density ρ=3.892 g/m^3, Whyckoff sites for Ti are U_x=U_y=U_z=0, for O U_x=U_y=0, U_z=0.2081 Å. If we define a new distance parameter u=0.399 Å, the atom coordinates can be written in a shorter form without numbers, see Table 3.

Table 3: *Positions of the anatase atoms*. We wrote position of the rutile atoms with 4 unit cell parameters: a=b=3.7845 Å, c=9.5143 Å, u=0.399 Å.

Element	x [Å]	y [Å]	z [Å]
O	0	0	c/4-u
O	a/2	a/2	3c/4-u
O	0	a/2	u
O	a/2	0	c/2+u
O	0	0	3c/4+u
O	a/2	a/2	c/4+u
O	0	a/2	c/2-u
O	a/2	0	c-u
O	a	0	c/4-u
O	a	a/2	u
O	a	0	3c/4+u
O	a	a/2	c/2-u
O	0	a	c/4-u
O	a/2	a	c/2+u
O	0	a	3c/4+u
O	a/2	a	c-u
O	a	a	c/4-u
O	a	a	3c/4+u
Ti	0	0	0
Ti	a/2	a/2	c/2
Ti	0	a/2	c/4
Ti	a/2	0	3c/4
Ti	a	0	0
Ti	a	a/2	c/4
Ti	0	a	0
Ti	a/2	a	3c/4
Ti	a	a	0
Ti	0	0	c
Ti	a	0	c
Ti	0	a	c
Ti	a	a	c

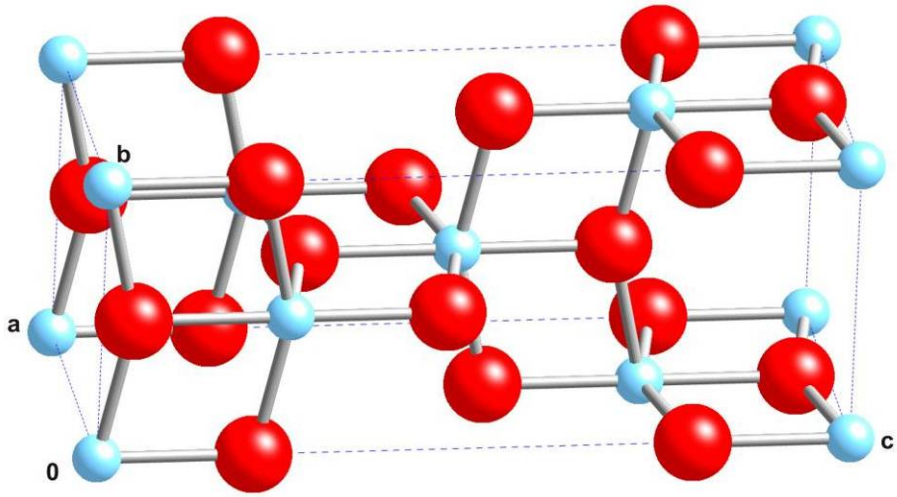

Figure 3: *Unit cell of the anatase*. Tetragonal unit cell of the second most common TiO_2 crystal, anatase. Red spheres represent O atoms, blue spheres Ti atoms. Axes are labeled by unit cell parameters: a (for x), b (for y), c (for z). 0 represents the centre of the coordinate system.

Brookite (see Table 1) on the other hand crystallises in orthorhombic unit cell, with point group D_{2h} (dihedral non Abelian group which contains 2-fold rotational axis perpendicular to the 2-folded primary rotational axis, and mirror plane perpendicular to the 2-fold axis). Its space group is Pbca (mmm), unit cell among all three in nature most common titania is the biggest, with 8 titanium and 16 oxygen atoms, see Figure 4.

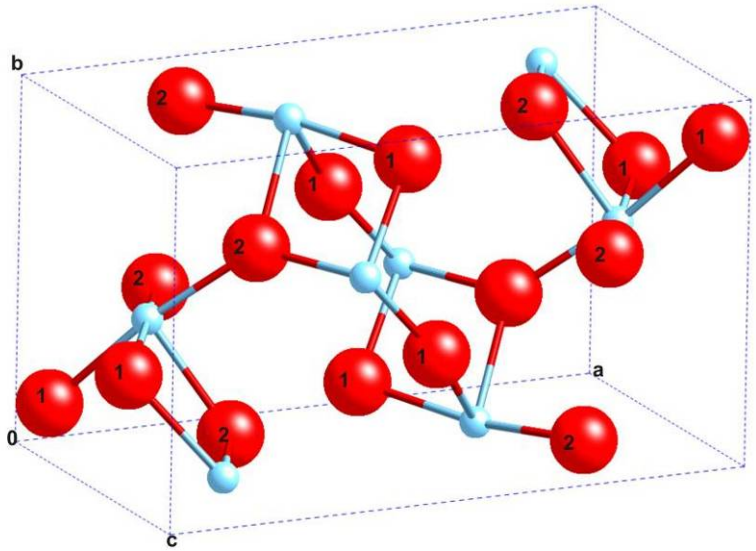

Figure 4: *Unit cell of the brookite*. Orthorhombic unit cell of the third most common TiO_2 crystal, brookite. Red spheres represent O atoms, blue spheres Ti atoms. Axes are labeled by unit cell parameters: a (for x axis), b (for y axis), c (for z axis). 0 represents the centre of the coordinate system. O atoms labeled by 1 or 2 define which Whyckoff sites are used for each O atom.

Unit cell parameters used in the thesis are[15] a=9.184 Å , b=5.447 Å, c=5.145 Å, angles α=β=γ=90 °, number of Ti atoms in the unit cell Z=8, unit cell volume V=257.380 Å, mass density ρ=4.126 g/m^3, Whyckoff sites for Ti are U_x=0.1290 Å , U_y=0.0972 Å , U_z=0.8629 Å, for O U_x^1=0.0101 Å ,U_y^1=0.1486 Å, U_z^1=0.1824 Å, and U_x^2=0.2304 Å ,U_y^2=0.1130 Å, U_z^2=0.5371 Å. Due to insimplicity of the unit cell, i.e. the reduction of the symmetry, it is impossible to write coordinates of the atoms in brookite's unit cell in any easier way, see Table 4.

Table 4: *Positions of the brookite atoms*. Position of the brookite atoms cannot be written with few parameters due to the complexity of the unit cell i.e. brookite has 9 Whyckoff sites. For O atoms labeled by [1], Whyckhoff sites U_x^1,U_y^1 and U_z^1 are used, while for O atoms labeled by [2], Wyckoff sites U_x^2,U_y^2 and U_z^2 are used in calculations of atoms coordinates.

Element	x [Å]	y [Å]	z [Å]
O^1	0.101	1.175	0.391
O^1	0.071	3.974	0.447
O^1	9.165	5.753	2.182
O^1	9.196	2.954	2.126
O^1	4.662	1.875	0.137
O^1	4.632	4.674	0.081
O^1	4.604	5.053	2.710
O^1	4.635	2.254	2.654
O^2	2.051	2.817	0.591
O^2	2.210	0.996	1.755
O^2	7.215	4.111	3.164
O^2	7.056	5.932	0.818
O^2	6.562	4.902	1.381
O^2	6.751	3.081	0.666
O^2	2.704	2.026	4.254
O^2	2.545	3.847	1.907
Ti	1.062	4.326	1.246
Ti	1.229	2.570	1.260
Ti	8.205	2.602	3.819
Ti	8.037	4.358	1.313
Ti	5.684	3.306	1.077
Ti	5.852	1.550	1.429
Ti	3.582	3.623	3.650
Ti	3.415	5.379	1.144

1.1.1 Properties and differences

The Ti-Ti, Ti-O distances in TiO_2 crystals are different, even if the type of the crystal's unit cell is the same, i.e. Ti-Ti distances in anatase are larger, and the Ti-O distances on the other hand are shorter when compared to rutile. Results of minimal distances between atoms in TiO_2 most common crystals are listed in Table 5, and calculated using Figure 2-3 and Table 2-4.

Table 5: *Minimal Ti-O and Ti-Ti distances in TiO_2 crystals*. Even if the type of the crystal's unit cell is the same, the distances between Ti-Ti and Ti-O atoms are different. We have listed minimal distances between them.

Crystal	symmetry	$d(Ti\text{-}Ti)_{min}$ [Å]	$d(Ti\text{-}O)_{min}$ [Å]
rutile	D_{4h}	2.956	1.946
anatase	D_{4h}	3.039	1.934
brookite	D_{2h}	3.064	1.865

Each O ion in anatase, rutile and brookite is coordinated by 3 Ti, and each Ti ion by 6 O. All common TiO_2 can be represented with distorted octahedrons, where Ti atom is in the middle, 6 O atoms are in the corners. In the rutile, each octahedron is in contact with 10 distorted TiO_6 octahedrons (TiO_6 octahedral share with adjacent octahedral 2 edges, 4 single corners, where there are just 2 octahedrons in the contact, 2 double corners, where there are 3 octahedrons in the contact), see Figure 5a. In the anatase, each octahedron is in contact with 8 distorted TiO_6 octahedrons (TiO_6 octahedral share with adjacent octahedral 4 edges, 4 single corners), see Figure 5b. In the brookite, which has the weakest symmetry among all three crystals, each octahedron shares 3 edges with adjacent octahedrons, Figure 5c.

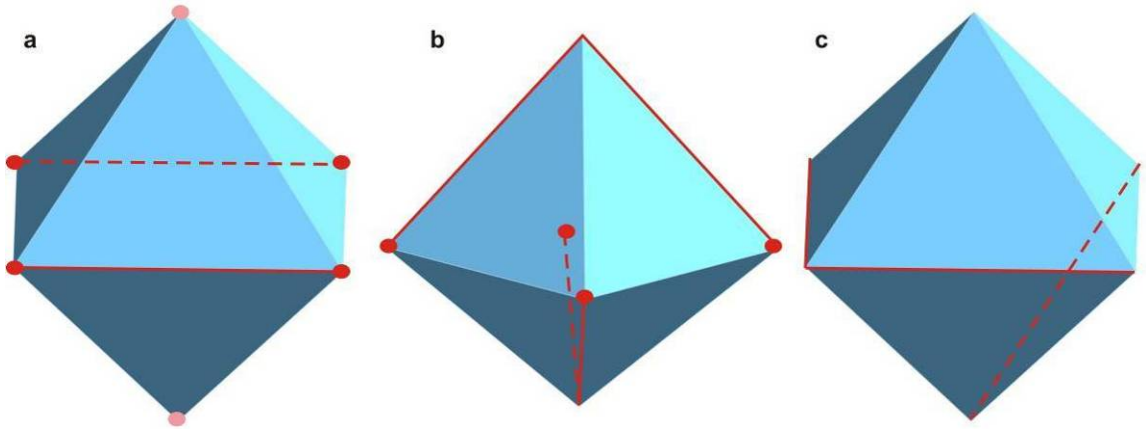

Figure 5: *TiO_6 octahedrons*. a) Rutile octahedron shares 2 edges with adjacent octahedrons (red lines), 4 single corners (red dots), and 2 double corners (pink dots). b) Anatase octahedron shares 4 edges with adjacent octaherons (red lines) and 4 single corners (red dots). c) Brookite octahedron shares with adjacent octahedrons 3 edges (red lines) and a few corners.

Difference in the number of the shared adjacent octahedron edges with the rule: "*The presence of shared edges, and particularly of shared faces, in a coordinated structure decreases its stability. This effect is large for cations with large valence and small coordination number.*"[18], tells that the most stable TiO_2 structure among anatase, rutile and brookite, is rutile, with only 2 shared octahedron edges, followed by brookite with 3 shared octahedron edges, followed by the least stable anatase, with 4 shared octahedral edges. In this manner, only rutile has a melting point[19], T_m, while metastable anatase and brookite only transform into each other or into rutile under specific conditions, see Table 6.

Table 6: *Melting point of TiO_2 crystals*. Melting point of the crystal is in accordance with the rule of the shared edges, i.e. the more edges the crystal has, the lower the stability of the crystal. Brookite and anatase can therefore transform only into each other at milder conditions, and finally into rutile, which has a melting point.

Crystal	shared edges [/]	T_m [°C]
rutile	2	1830–1850
anatase	4	transforms into rutile
brookite	3	transforms into rutile

Different transformation temperatures among metastable TiO_2 crystals, anatase and brookite, which are common TiO_2 crystals in nanoscale range, and into rutile, the most thermodynamically stable phase, are found in the literature, see Table 7. It was observed that synthesis of nanomaterial produced anatase and/or brookite, which transformed into

rutile upon heating, which grew much faster compared to anatase. Conclusion on the rutile and anatase thermodynamical phase stability was that anatase was more stable for particle size below 14 nm.[20,21] It was found out that the crystal modification depended on the synthesis. Anatase was more stable below 50 nm, and transformed into rutile at ~700 °C.[22] For particle size below 11 nm anatase was found to be the most stable, for particle size above 35 nm rutile, for particle size between 11 nm and 35 nm brookite.[23] It was proposed that transformation from anatase to rutile starts at surface and migrates into the bulk,[24] that transformation depends on temperature, impurities, grain size, reaction atmosphere and synthesis conditions.[25]

Table 7: *Transformations among TiO_2 crystals*. When heating TiO_2 crystals, different transformations were observed.[25]

Before	after	T_t [°C]	note
Brookite[26]	anatase	< 780	slowly with crystal growth
brookite	anatase to rutile	780 < T < 850	fast transformation
rutile	rutile	>850	fast crystal growth
brookite[27]	rutile	> 700	
anatase	rutile	> 700	
anatase	rutile	700< T < 800	size of the particles increases

Differences in structures of TiO_2 crystals is also different electronic band structure[28], i.e. different band gaps, E_g, see Table 8. For determining the band gap in crystals (see Chapter 1.4) there are several methods: nearly free electron approximation, mean field approximation, tight binding model, muffin-tin potentials, augmented plane wave (APW) method, Hubbard model, density-functional theory (DFT)[28], many-body theorem/Green's function (Korriga, Kahn and Rostoker, KKR) method, GW approximation, many body perturbation theory, orthogonalized plane wave (OPW) method, pseudopotentials, cellular method, combined methods etc. Landmann et.al.[28] improved DFT with standard generalized gradient approximation (GGA) exchange-correlation (XC) functional according to Perdew, Burke and Ernzerhof (PBE), and a nonlocal, range-separated, screened Columb potential hybrid density functional according to Heyd, Scuseria and Ernzerhof (HSE06). They have also included in a full-frequency-dependent G_0W_0 scheme the quasiparticle (QP) corrections within the GW approximation. Others performed extended Hückler molecular orbital calculations (EHMOC)[29], self-consistent orthogonalized linear combination of atomic orbitals (SCOLCAO)[30], Kohn-Sham method (KS)[31].

Band gap is usually determined with help of diffuse reflectance measurements (see Figure 20) from the tangent lines of Kubelka-Munk function versus the energy of the light. In the case of the brookite[16], measurements of the band gap are different (see Table 8) because some are calculated for the direct and some for the indirect band gap.

From DFT rutile's and brookite's band gaps are direct (momentum of holes and electrons is the same in the conduction and in the valence band, see Figure 19a), while anatase has indirect band gap (electron cannot emit the photon directly, but transfers momentum to the crystal lattice, see Figure 19b).[28]

Because light is absorbed in the near UV solar spectrum, electrons, e^-, are excited from valance into conduction band leaving behind positive charge carriers, h^+. Exciton, pair $e^-:h^+$, with oxidizing influence on the surroundings, is the reason for the light induced semiconductor properties. It destroys organic bonds, which is a problem in the pigment industry, on the other hand it is a reason for photocatalysis (see Chapter 1.4 that is one of the properties, for which TiO_2 is being praised for.[19]

Table 8: *Electronic properties of TiO_2 crystals*. Measured, and calculated band gap values with different methods at Γ-point (the centre of the momentum crystal space), of all 3 most common TiO_2 crystals.

	E_g [eV]		
Method\crystal	rutile	anatase	brookite
measurement	3.02[32]	3.2[32]	3.1-3.4[16]
EHMOC[29]	3.02	3.23	3.14
SCOLCAO[30]	1.78	2.04	2.20
KS[31]	/	/	2.1
DFT-PBE[28]	1.88	1.94	1.86
DFT-HSE06[28]	3.39	3.60	3.30
G_0W_0-PBE[28]	3.46	3.45	3.45
G_0W_0- HSE06[28]	3.73	3.68	3.68

Also different optical properties are result of different crystal structures of TiO_2, i.e. all crystal modifications of TiO_2 have different refractive indexes, see Table 9. Rutile and anatase have both uniaxial anisotropy (anatase was found also as biaxial in deeply coloured crystals), where 1 crystal axis, the optic axis, is different from the other 2 axes, which are equal. Linear polarization parallel to the optic axis has extraordinary refractive index, n_e, while linear polarization perpendicular to the optic axis has ordinary refractive index, n_o. Both crystals are uniaxial birefringent, $\Delta n=n_e-n_o\neq 0$, where refractive index of the ordinary and extraordinary depends on the polarization of the incident light. The difference between anatase and rutile is that in the case of the anatase the birefringence is negative, $\Delta n=-0.073$, i.e. anatase is a "negative crystal", while rutile is a "positive crystal", $\Delta n=0.287–0.294$.

Brookite on the other hand has biaxial anisotropy and is trirefringent with 3 different refractive indexes, therefore it is not invariant under any rotation around any axis. The refractive index can be written as a tensor with 3 different eigenvalues: n_α, n_β, n_ρ. Maximal birefringence is $\Delta n=0.117$.

All 3 most common crystal modifications of TiO_2 are weakly pleochron, i.e. the crystals seem to be differently coloured when observed under different angles with polarized light. Tetragonal anatase and rutile can show only 2 different colours, while orthorhombic brookite can show 3.[33]

Table 9: *Optical properties of TiO_2 crystals*. Refractive indexes of all 3 most common TiO_2 crystals.[17,34]

Crystal	anisotropy	n_e [/]	n_o [/]	n_α [/]	n_β [/]	n_γ [/]
rutile	uniaxial (+)	2.899–2.908	2.605–2.621	/	/	/
anatase	uniaxial (-)	2.488	2.561	/	/	/
brookite	biaxial (+)	/	/	2.583	2.584	2.700

Due to different structures of TiO_2 crystals, they have different "finger prints", i.e. X-Ray diffraction patterns (XRD) for rutile, anatase and brookite are different (see Figure 6), also selected area electron diffraction patterns (SAED) are different (see Figure 7), Raman spectra (see Figure 9) are different etc.

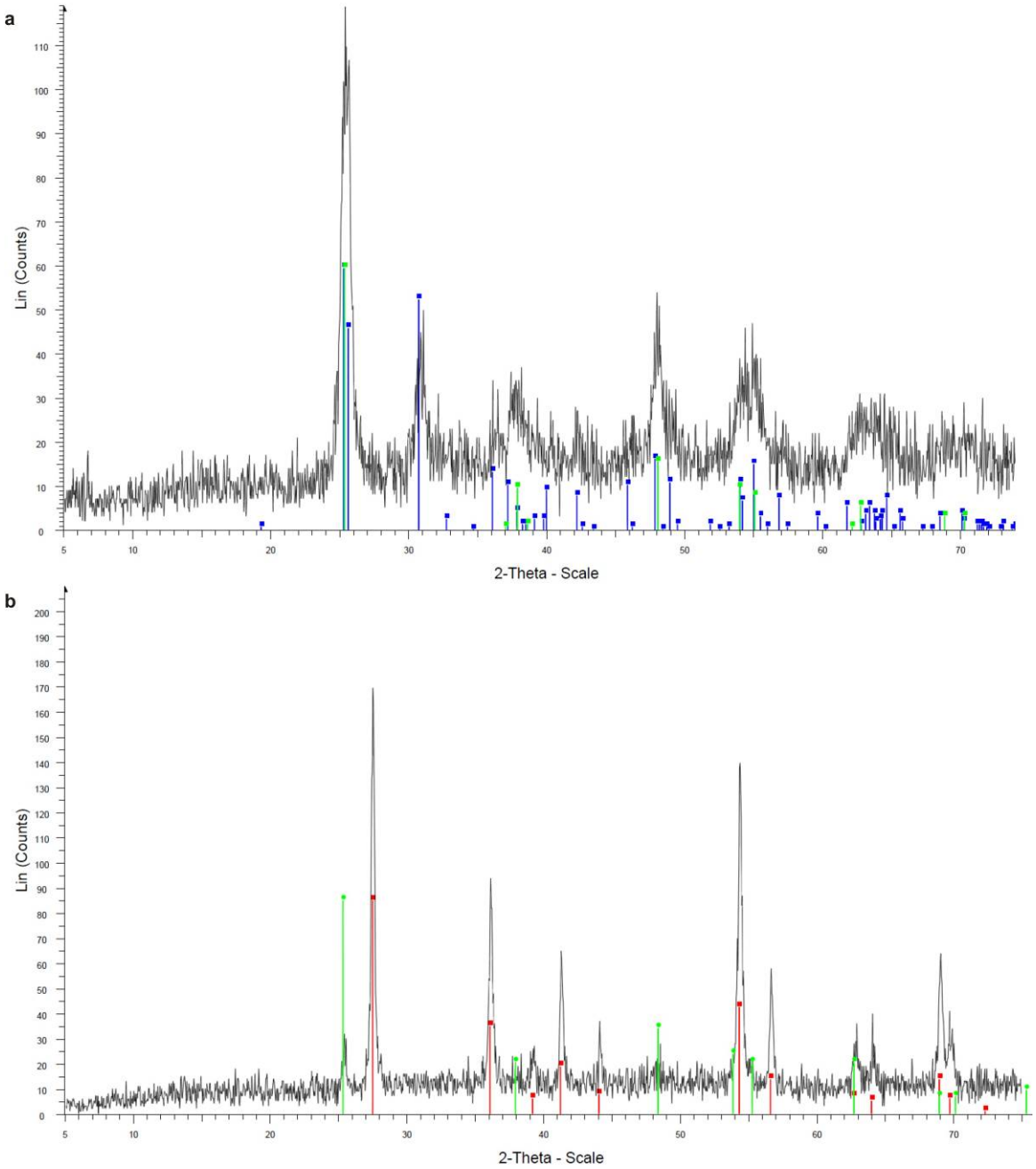

Figure 6: *XRD of rutile, anatase and brookite*. a) XRD measurement of a sample containing anatase and brookite, and sample containing b) anatase and rutile. Calculated patterns of anatase peaks are represented by green lines, of brookite peaks by blue lines, of rutile peaks by red lines.

From XRD pattern we can determine if the material is amorphous (no peaks in the pattern, just noise) or crystalline (there are peaks in the pattern). From the position and the relative intensities of the peaks we can determine which crystal form it is, and if the crystals are smaller than 100 nm, we can determine also their size from the width of the peaks using Scherrer equation[35], see Equation 1.

$$d = \frac{K\lambda}{B\cos\theta} \tag{1}$$

d is the average size of the crystal in the specific direction, defined by the measured peak (each peak represents certain set of planes, certain direction), K is the Scherrer constant or the shape factor, 0.89 in this work, B is the ful width on the half of the

maximum of the peak, measured in 2θ scale in radians, θ is the Braggs angle of the maximum of the peak, λ is the wavelength of the incident X-rays.

x-axis in Figure 6 is represented in Braggs units, i.e. in 2θ units, which can be transformed into d_{hkl} units, where d_{hkl} is the distance between planes, using Braggs equation, see Equation 2.

$$d_{hkl} = \frac{\lambda}{2\sin\theta} \tag{2}$$

Also from electron diffraction (SAED) we can determine whether the material is amorphous or crystalline. If the material is amorphous, the diffraction pattern consists of diffuse and very broad rings with low intensity. When the material is polycrystalline with particle size in the range of few nm the pattern consists of parallel uniform circles with different intensity. At an even bigger particle size (5–20 nm) individual dots could be resolved in the parallel circles (Figure 7). Monocrystalline diffraction pattern is characterised with individual dots, ordered in some specific pattern, represent the 2D projection of the reciprocal lattice of the crystal (Figure 8).

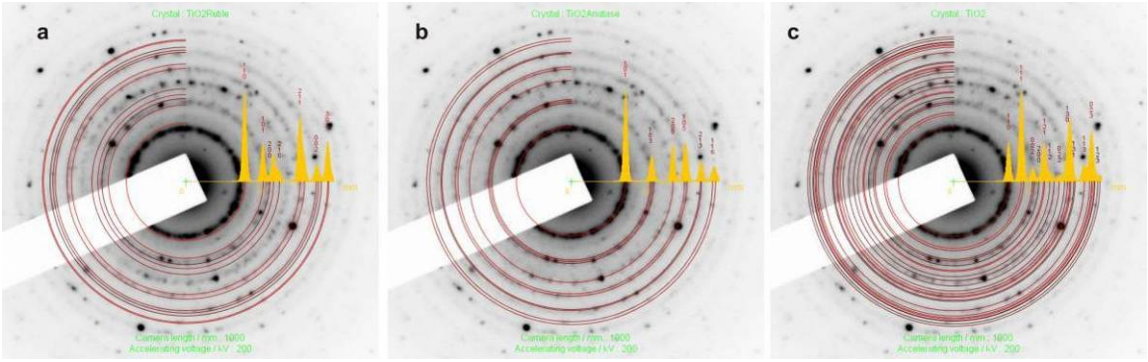

Figure 7: *SAED of rutile, anatase and brookite*. SAED measurement of anatase with small amount of brookite, with theoretical models (red circles) of a) rutile b) anatase and c) brookite, with peaks intensities (yellow graph).

From the diffraction peaks it is possible to determine whether we are dealing with smaller or bigger particles i.e. as the nanoparticle size increases, the diffraction peaks narrow.[36]

In Figure 8 it is seen that not all dots in the diffraction pattern have the same intensity, even more, some cannot even be seen (they are so-called forbidden). This is due to the structure factor S(**K**), which we calculated for anatase and rutile (results are in Table 11), see Equation 3.

$$S(\vec{K}) = \sum_{j=1}^{s} e^{-i\pi\vec{K}\cdot\vec{r}_j} f_j \tag{3}$$

Summation goes over different ions (in TiO_2 over Ti and O). **K** is the vector of the reciprocal lattice, see Equation 4, $\mathbf{r}_j$ is the basis vector. f_j is the atomic factor, which is the same for the same atoms, different for different atoms.

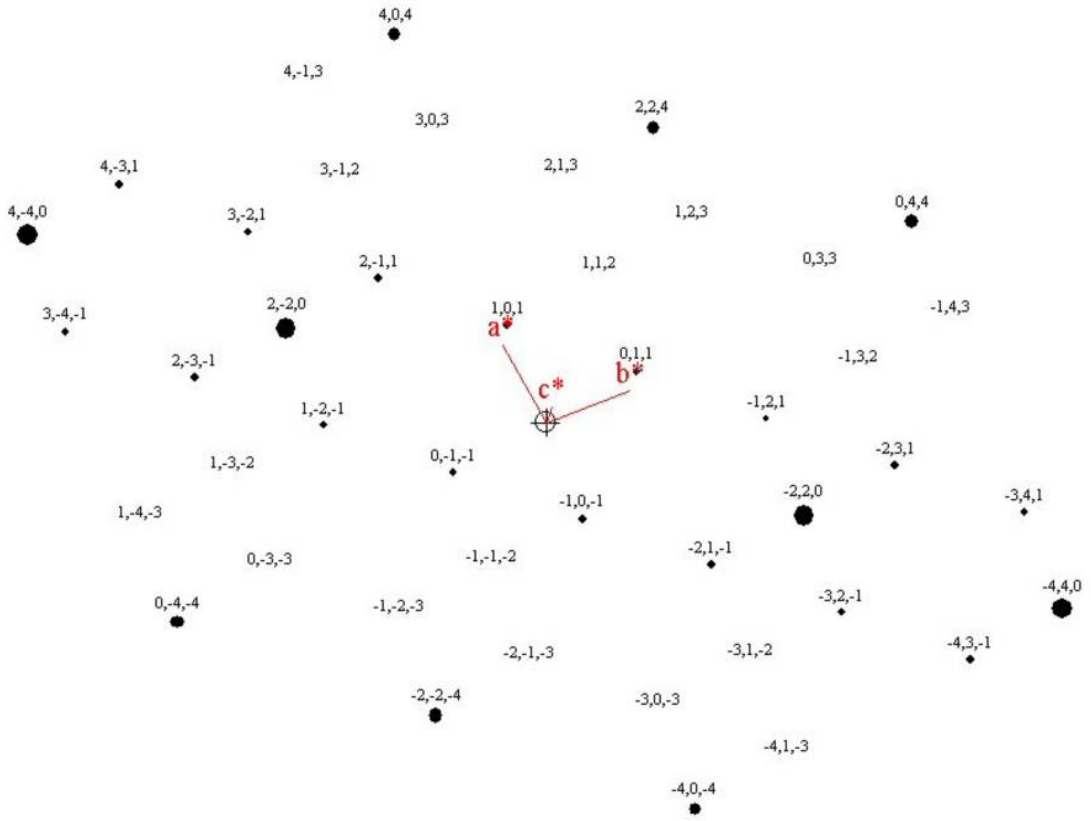

Figure 8: *SAED simulation of anatase monocrystal*. SAED simulation of anatase monocrystal in the zone axis [-1, -1, 1]. Some intensities are zero (no dot on the diffraction pattern), some are weak (small dot on the diffraction pattern), some are obvious (big black dots on the diffraction pattern).

Vector of reciprocal lattice can be written as:

$$\vec{K} = m_1\vec{b}_1 + m_2\vec{b}_2 + m_3\vec{b}_3 \tag{4}$$

Where $m_i \in Z$, $\mathbf{b}_i$ are vectors of reciprocal lattice, see Equation 5, written using the cyclic permutation of i, j, k:

$$\vec{b}_i = 2\pi \frac{\vec{a}_j \times \vec{a}_k}{|(\vec{a}_1, \vec{a}_2, \vec{a}_3)|} \tag{5}$$

$\mathbf{a}_i$ are vectors of Bravais lattice, with which the unit cell is described. For the rutile, anatase and brookite Bravais vectors are presented in Equation 6:

$$\begin{aligned} \vec{a}_1 &= a(1,0,0) \\ \vec{a}_2 &= b(0,1,0) \\ \vec{a}_3 &= c(0,0,1) \end{aligned} \tag{6}$$

a, b and c are unit cell parameters from Table 1, i.e. a=b for anatase and brookite. Basis for rutile contains 4 O and 2 Ti ions, see Table 10, for anatase 8 O and 4 Ti ions, see Table 10, for brookite 16 O and 8 Ti ions.

Table 10: *Basis vectors of rutile and anatase*. Basis vectors of rutile and anatase crystals $\mathbf{r}_i$ used in calculations of their structure factors S(**K**).

Rutile crystal			
Atom	x	y	z
Ti	0	0	0
Ti	a/2	a/2	c/2
O	a/2-u	a/2-u	0
O	a/2+u	a/2+u	0
O	a-u	u	c/2
O	u	a-u	c/2
Anatase crystal			
Atom	x	y	z
Ti	0	0	0
Ti	a/2	a/2	c/2
Ti	a/2	0	c/4
Ti	0	a/2	3c/4
O	a/2	0	u
O	0	a/2	c-u
O	0	0	c/4-u
O	0	0	3c/4+u
O	a/2	a/2	c/4+u
O	a/2	a/2	3c/4-u
O	a/2	0	c/2-u
O	0	a/2	c/2+u

Reciprocal vectors for the rutile, anatase and brookite, using Equation 5 and Equation 6, are written in Equation 7:

$$\begin{aligned}\vec{b}_1 &= \frac{2\pi}{a}(1,0,0)\\ \vec{b}_2 &= \frac{2\pi}{b}(0,1,0)\\ \vec{b}_3 &= \frac{2\pi}{c}(0,0,1)\end{aligned} \tag{7}$$

Structure factor of the rutile, see Equation 8, can be written using Equation 3, 4 and 7 with appropriate basis vectors from Table 10:

$$S(\vec{K}) = f_{Ti}(1+(-1)^{m_1+m_2+m_3}) + f_O(2(-1)^{m_1+m_2} + 2(-1)^{m_3}) \tag{8}$$

Structure factor of the anatase, see Equation 9, can be written using Equation 3, 4 and 7 with appropriate basis vectors from Table 10:

$$\begin{aligned}S(\vec{K}) &= f_{Ti}(1+(-1)^{m_1+m_2+m_3} + (-1)^{m_1+\frac{1}{2}m_3} + (-1)^{m_2+\frac{3}{2}m_3}) +\\ &+ f_O((-1)^{m_1} + (-1)^{m_2+2m_3} + (-1)^{\frac{1}{2}m_3} + (-1)^{m_1+m_3} + (-1)^{m_2+m_3})\end{aligned} \tag{9}$$

Knowing that m_i is an integer, it is possible to write first order structure factors (vector

(m_1, m_2, m_3) in the shortest way in the specific direction and different from 0) for rutile and anatase, see Table 11, as well as the intensities for different Bragg reflections, I(**K**), which is proportional to the square of the absolute value of the structure factor ($I(\mathbf{K}) \propto |S(\mathbf{K})|^2$).

Table 11: *Structure factor and intensities of Bragg reflections for rutile*. Calculated structure factor, S(**K**), and intensities of Bragg reflections for rutile, where f_{Ti} and f_O are atomic factor for Ti and O ions respectively; $n \in Z$.

Rutile				
m_1	m_2	m_3	S(**K**)	I(**K**)
even	even	even	$2f_{Ti}+4f_O$	$4f_{Ti}^2+8f_{Ti}f_O+16f_O^2$
even	odd	even	0	0
odd	even	even	0	0
odd	odd	even	$2f_{Ti}+4f_O$	$4f_{Ti}^2+8f_{Ti}f_O+16f_O^2$
odd	odd	odd	0	0
odd	even	odd	$2f_{Ti}-4f_O$	$4f_{Ti}^2-8f_{Ti}f_O+16f_O^2$
even	odd	odd	$2f_{Ti}-4f_O$	$4f_{Ti}^2-8f_{Ti}f_O+16f_O^2$
even	even	odd	0	0
Anatase				
m_1	m_2	m_3	S(**K**)	I(**K**)
even	even	even, 4n	$4f_{Ti}+5f_O$	$16f_{Ti}^2+40f_{Ti}f_O+25f_O^2$
		even, ≠4n	$3f_O$	$9f_O^2$
even	odd	even, 4n	f_O	f_O^2
		even, ≠4n	$-f_O$	f_O^2
odd	even	even, 4n	f_O	f_O^2
		even, ≠4n	$-f_O$	f_O^2
odd	odd	even, 4n	$-3f_O$	$9f_O^2$
		even, ≠4n	$4f_{Ti}-5f_O$	$16f_{Ti}^2-40f_{Ti}f_O+25f_O^2$
odd	odd	odd, 4n+1	if_O	f_O^2
		odd, ≠4n+1	$-if_O$	f_O^2
odd	even	odd, 4n+1	$2f_{Ti}-i(2f_{Ti}-f_O)$	$8f_{Ti}^2-4f_{Ti}f_O+f_O^2$
		odd, ≠4n+1	$2f_{Ti}+i(2f_{Ti}-f_O)$	$8f_{Ti}^2-4f_{Ti}f_O+f_O^2$
even	odd	odd, 4n+1	$2f_{Ti}+i(2f_{Ti}+f_O)$	$8f_{Ti}^2+4f_{Ti}f_O+f_O^2$
		odd, ≠4n+1	$2f_{Ti}-i(2f_{Ti}+f_O)$	$8f_{Ti}^2+4f_{Ti}f_O+f_O^2$
even	even	odd, 4n+1	if_O	f_O^2
		odd, ≠4n+1	$-if_O$	f_O^2

Due to the complexity of the unit cell of the brookite, the explanation of the calculation of the structure factors is not given. Throughout the thesis we used computer code EMS[37] for diffraction pattern simulation.

Miller indexes, hkl, for all 3 most common crystalline TiO_2, plane spacings d_{hkl}, observed intensities of the TiO_2 fingerprint peaks, XRD and SAED, are gathered in Table 12.

Table 12: *Miller indexes and plane spacings for rutile, anatase and brookite*. Rutile, anatase and brookite have different crystal structures, therefore have different plane spacings, d_{hkl}, which react with different intensities upon Braggs experiment.[17]

Rutile				
d_{hkl} [Å]	h	k	l	Estimated intensity [%]
3.2413	1	1	0	100
2.4824	1	0	1	50
2.2920	2	0	0	/
2.1829	1	1	1	40
Anatase				
d_{hkl} [Å]	h	k	l	Intensity [%]
3.5098	1	0	1	100
2.4267	1	0	3	10
2.3752	0	0	4	20
2.3280	1	1	2	/
Brookite				
d_{hkl} [Å]	h	k	l	Intensity [%]
4.6055	2	0	0	/
3.5235	2	1	0	100
3.4798	1	1	1	80
2.9118	2	1	1	90

Inelastic scattering of a photon happens with much smaller probability as the elastic scattering. However, TiO_2 crystals are known as a strong Raman scatterers.[38] Different Raman spectra of rutile, anatase and brookite, see Figure 9, comes from the differences in the crystal structure. Even if anatase and rutile belong to the same point group, they have different degrees of freedom (3N) due to different number of ions (N) in the unit cell. 3 degrees of freedom belong to translations, 3 to rotations, all remaining belong to vibrations, from which Raman active vibrations can be observed by Raman spectroscopy. If nanoparticles size decreases, Raman peaks broaden.[36]

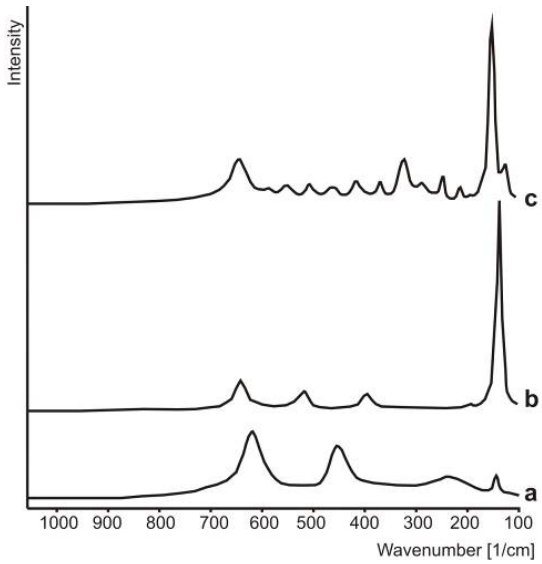

Figure 9: *Raman spectra of TiO_2 most common crystals*. Raman spectra of a) rutile, b) anatase, c) brookite.

For heterogeneous catalysis the shape of the crystals of catalyst is very important, namely reactions proceed differently on different crystal surfaces[39], to determine the equilibrium shape of the crystals, the Wulff construction can be used.[40]

Wulff showed that the normal distance from a common centre of a small crystal to a surface facet is proportional to the surface energy of the facet, see Equation 10.

$$\frac{\gamma_i}{h_i} = const. \tag{10}$$

γ_i is specific surface free energy, h_i distance from the centre of the i-th crystal plane.

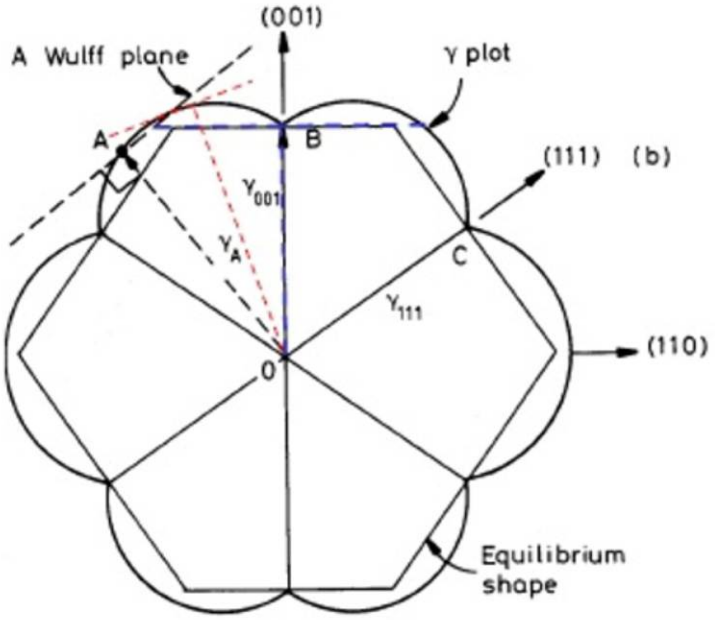

Figure 10: Scheme of *Wulff construction of equilibrium shape of the 2-dimensional crystal*. Outer curve represents surface free energy γ, inner envelope the equilibrium crystal shape.[41]

To draw the crystal equilibrium shape surface free energy was plotted as a function of angle (0:2π) from the Wulff point (centre of the crystal). The black outer curve was got in Figure 10. The normal lines to the radius vectors were drawn at intersections of the polar plot (red line in Figure 10) at all orientations. Intersections of normal lines were connected and the equilibrium crystal shape was got.

The energies of the crystal planes used in the plot are minimized free Gibbs energies from Equation 11.

$$\Delta G_i = \sum_j \gamma_j S_j \tag{11}$$

In Equation 11 the sum goes over all crystal faces of the i-th crystal, Sj is surface of the j-th crystal face.

1.1.2 Use of the anatase and other crystal modifications

TiO_2 exists in many different crystal modifications. Two of them, rutile and anatase, are quite common due to mild condition synthesis and accessibility in the nature. Rutile has been used as a white pigment for decades because of its high refractive index and high reflectance in Vis spectrum, which makes it a good white powder pigment.[42] Its white colour also does not change under UV irradiation. Therefore, it is a preferred material in the paints, in protective coatings, it is used also in plastics, paper, cosmetics, food etc.[43]

On the other hand, anatase became very interesting for different applications since the discovery of superhydrophilicity phenomenon of glass coated with TiO_2 and exposed to the sun light. TiO_2 in anatase form is nowadays incorporated in the outdoor building materials[44] and paints, which reduce concentrations of airborne pollutants[45] and the need to use conventional cleaning chemicals, because beside being superhydrophilic it is also photocatalytic[46,47], therefore it has abilities to decompose organic species, therefore the material is treated as self-cleaning.[44,48] It is used in anti-fogging coatings[44], for self-cleaning and antimicrobial surfaces[49], etc. It is also used for sterilization of the surfaces[44], especially in the medicine[44], for waste and grey water detoxification[50,51,52,53], soil detoxification[54] etc.

There are several interesting applications: deposited on SiO_2 beads can be used for odour-eliminating process in cat litter[55], for catching mosquitoes along with cleaning and deodorizing the indoor air[56], on medical implants to annihilate the bacteria on the surface[57], in dental bleaching products[58], in refrigerators to decompose ethylene[59], on sound barriers at highways to decompose NO_x gases[60].

It shows also great potential for use in dye-sensitive solar cells[61], smart sensors, actuators,[62] fast electrochromic system[63], multifunctional devices[64], mesophorous membranes[65], food[66], cosmetics[67] etc.

1.2 Synthesis of the material

Synthesis of the material is the most important part in the field of research and development of new materials. But to understand the synthesis itself, it would not be just “shake and make”, “mix and wait” or “heat and beat”.[68] Understanding of the materials creation is nowadays the crucial element for creating smart materials for modern applications.

1.2.1 Sol-gel synthesis

When dealing with nanomaterials, it is good to take precaution already at the synthesis stage, i.e. for health reasons it is best to deal with nanomaterials suspended in some liquid phase. Sol-gel syntheses of nanomaterials, i.e. one of the wet chemical syntheses, offer low processing temperature and creation of thermodynamically metastable materials.

Sol-gel synthesis consists of hydrolysis and condensation (see Figure 24), which are usually multi-step processes, of precursors, which can be metal alkoxides or salts. Solvents used are usually organic or aqueous.[69]

Procedure 1: *Sol-gel synthesis.* Wet chemical synthesis of nanomaterials can be characterized by several steps.[70]

Step 1: formation of sol
Step 2: gelation
Step 3: aging of the gel
Step 4: drying of the gel
Step 5: dehydration of the gel
Step 6: densification and decomposition of the gel

In the Procedure 1[70] are all the possible steps of sol-gel synthesis. The first step is the formation of stable colloidal solution of the alkoxides, in the second step the formation of oxide-bridged network takes place by polycondensation. This step is accompanied by increase in the viscosity of the solution. The next step is the polycondensation reactions, which continue until the gel transforms into a solid mass. At the same time Ostwald ripening and phase transformation take place. The fourth step is the removing of all volatile liquids, followed by the removal of surface-bound –OH groups, usually by calcination at high temperature (up to 800 °C). The last step is taking place at temperatures higher than 800 °C, when the pores of the gel collapse, remained organic species are burned. Products of sol-gel synthesis can be amorphous or crystalline.

1.2.2 Hydrothermal and solvothermal synthesis

Hydrothermal and solvothermal syntheses are one of the most important and nowadays very popular techniques for advanced material synthesis. The origin of the word "hydrothermal" is geological, describing the action of water at elevated temperatures and pressures, leading to the creation of crystals. When water is replaced by other solvents, the synthesis is called solvothermal.

Hydrothermal/solvothermal synthesis, see Figure 27, is a heterogeneous reaction in aqueous/non-aqueous solvents under high pressure and temperature conditions that can dissolve and recrystallize materials that are insoluble under normal conditions (TiO_2 is insoluble in water under ordinary conditions).[71]

During synthesis the pressure can become very high, so special instrumentation is needed. In the market are several different reactors, called autoclaves, pressure vessels, and even high-pressure bombs. The basic autoclave, see Figure 26, consists of outer metallic vessel, with inner Teflon cartridge.

Ideal hydrothermal autoclave should satisfy the following requirements[71]: it should be inert to acids, bases, oxidizing agents; it should be easy to assemble and disassemble; it should be leak-proof to the required temperature and pressure; in the gradient autoclaves the length should be sufficient to obtain the desired temperature gradient; it should withstand high pressure and temperatures for long periods of time without any damage.

If autoclave with no safety backups, or with no high-pressure barometer is used, the filling of the autoclave should always be in the safety zone, where the pressure will not start rising dramatically, i.e. if the highest working temperature is 200 °C, the filling of the autoclave should not exceed 80 % of the inner vessel.

Products of hydro/solvo thermal synthesis can be amorphous or crystalline in the form of nanocrystals or big monocrystals, of all different morphologies. Size of the monocrystal is limited with the size of the cartridge.

There are numerous papers concerning the crystal growth of TiO_2 via hydrothermal synthesis for which various growth models were proposed. Cho et al.[72] proposed a

growth model for bipyramidal anatase crystals, synthesized in alkaline conditions at 200 °C for 2 to 16 h and at 240 °C for 32 to 64 h. They suggested that anatase crystals grow by oriented attachment along [001] direction which is followed by thickening with Ostwald's ripening. They observed that the longer the time and the higher the temperature of hydrothermal synthesis, the more defined and larger the final bipyramidal crystals are. Deng et al.[73] described the growth of large bipyramidal anatase single crystals in the range of a few microns produced by hydrothermal synthesis at 200 °C for 48 h at pH values between 5.6 to 11.0. They observed that formed anatase nuclei had truncated bipyramidal morphology. The fastest growth rate was observed on the high-energy {001} faces, and the crystal elongation was ob-served along the <001> directions, which eventually resulted in the elimination of high-energy surfaces {001} and the formation of acute anatase bipyramids. They observed that the size and shape of the crystals depends on the pH value. The higher the pH, the larger and more regular in shape are the anatase bipyramids. They observed that at pH 10.5 and 200 °C better defined and larger bipyramidal crystals appear when the time of the hydrothermal synthesis is longer. Wang et al.[74] investigated the formation of octahedral bipyramids and nanosheets prepared with hydrothermal synthesis from tetrabutyl titanate and a HF solution at 200 °C and 24 h. They found that with an increase of HF concentration to the optimal value, at which poorly photocatalytic cubic $TiOF_2$ still does not appear, bipyramidal crystals trans-form into nanosheets (plate-like crystals) and the fraction of high-energy {001} facets in-creases. This is due to preferential growth along the a-axis, whilst growth along the c-axis is inhibited. Chen et al.[75] prepared monodispersed, well-aligned, TiO_2 nanosquares in large quantities from $Ti(OBu)_4$. The colloidal liquid was hydrothermally treated from 120 °C to 190 °C for different times in the presence of TMAOH, which accelerated the formation of anatase and modified the particle shape to nanocubes. At 160 °C and after 4 h of hydrothermal synthesis, anatase nanosquares started to form. If the time was longer or if the temperature was higher, the crystals became elongated. Barnard et al.[76] investigated the effects of surface chemistry on the morphology and phase stability of TiO_2 nanoparticles using a thermodynamic model based on surface free energies and surface tensions. They found that acidic or alkaline conditions have a significant influence on the shape of the nanocrystals and to the anatase-to-rutile transformation. They defined a ratio between the lengths B and A of truncated bipyramidal crystals, where A is the length of the edge of the basal square cross-section (in the middle of the bipyramid), and B is the edge of the small pinacoidal {001} facets (the top and bottom surfaces of truncated bipyramids). With this ratio they defined the degree of truncation. They minimized the total Gibbs free energy with respect to the B/A ratio and found that if the surface was oxygenated, the ratio was larger compared to the case when the surface was hydrogenated.

1.2.3 Treatment with ultrasound

Treatment with ultrasound radiation from 20 KHz to 10 MHz with acoustic cavitations, see Figure 28, is used for breaking the bonds in the aggregates, without destruction of the material. Acoustic energy is concentrated in a small volume, where temperature is several 1000 K, pressures in GPa, local acceleration 12 orders higher than gravity [77], conditions proper for the break of the bonds.

1.2.4 Calcination

Calcination, Figure 29, is a thermal treatment in air used to remove organic compounds, for phase transformation, thermal decomposition or reaction of two or more substances due to enhanced diffusion. Temperatures are lower than the melting point.

1.3 Assembly of the materials

Nanomaterials could be synthesised ordered via 2 different paths, i.e. with bottom-up, and top-down approach, see Figure 11.[78] In top-down approach, nanoparticles are formed from the bulk, in bottom-up approach nanoparticles are created from atoms/molecules.

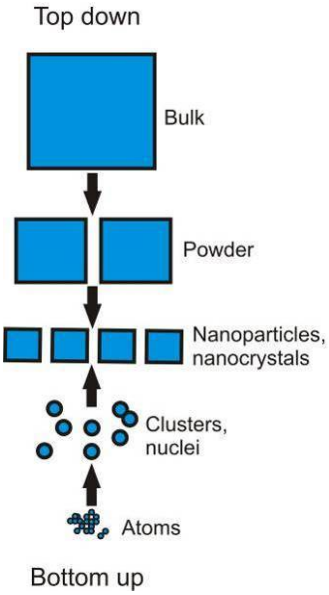

Figure 11: *Top-down and bottom-up approach*. Different approaches towards ordered nanoparticles. Top-down goes from bulk material, through powder to nanoparticles, bottom-up approach starts with atoms/molecules, which arrange into clusters that are building blocks of the nanoparticles.[79]

Top-down approach can happen only with physical help from the surroundings, i.e. with cutting, machining, milling, mechanical grinding, annealing, evaporation, sublimation, thermolysis template synthesis, arc discharge, laser ablation, ion milling, electron beam evaporation, pyrolysis, high-energy sonification, chemical etching, erosion, lithography, hydrolysis, volcanic activity etc. On the other hand bottom-up approach happens with chemical vapour deposition, atomic layer deposition, thermolysis, aerosol techniques, gas phase condensation, gas phase agglomeration, molecular self-assembly, nucleation and sol-gel processes, chemical precipitation, single crystal growth, electrolysis, supercritical fluid expansion, scanning tunnelling microscope writing, protein synthesis, crystal formation methods, self-assembly etc.[78]

Assembly is a process with which from smaller components we get bigger. It can be done by itself on all scales (from nanomaterials to planetary system), or with the human intervention, but just on a smaller scale. When there is no human intervention, the assembly is self-assembly, otherwise it is called assisted-assembly, which is always consuming energy.

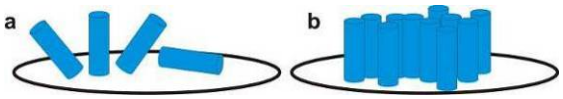

Figure 12: *Assembly*. With both types of assembly, self-assembly and assisted-assembly, particles in a) disordered state and in b) ordered state.

1.3.1 Self-assembly

Self-assembly represents the cheapest method of forming organized structures in disordered systems. "*Self-assembly is the autonomous organisation of components into patterns without human intervention.*"[80] Static self-assembly is spontaneous aggregation of particles without the influence of any external forces, where the system is trying to reach equilibrium and minimize the Gibbs free energy (minimization of repulsive and maximization of attractive interactions):

$$\Delta G_{SA} = \Delta H_{SA} - T\Delta S_{SA} \tag{12}$$

Equation 12 represents thermodynamics of the self-assembly (SA), where ΔG_{SA} is Gibbs free energy, ΔH_{SA} is the enthalpy change, and ΔS_{SA} is the entropy change. Self-assembly is spontaneous, if ΔG_{SA} is negative, i.e. if enthalpy is negative and bigger from the entropy part. If enthalpy and entropy terms are equal, the spontaneous self-assembly will not take place.[81]

The self-assembly is governed by the nucleation and growth. Small assemblies are formed because the attractive interactions between their components lower the Gibbs free energy. Gibbs free energy continues to drop, assemblies continue to grow until they become stable.[81]

All building parts self-assemble on a local level, under weak local forces: Coulomb interactions, van der Waals interactions, hydrogen bonds, π interactions, short range strong repulsion (Pauli exclusion principle) etc.[82] The weakness of forces enables system to adjust initial position even after aggregation enabling the system to find the position with lowest free energy. However, it is possible to govern the self-assembly by changing the functionality of side groups of nanoparticles, and their characteristics like hydrophilicity or hydrophobicity.[83]

1.3.2 Assisted-assembly

Assisted-assembly, externally directed self-assembly, dynamic self-assembly, self-organisation, is happening mainly in chemical solutions. Its product can be thermodynamically metastable and dependent on external conditions.[81]

There are several ways to force nanoparticles to assemble. One way is with diffusion-limited aggregation (DLA), which takes place in diluted suspension and results in creation of fractals. Even if the suspension is in concentration's equilibrium, there is always random, Brownian motion present (diffusion), with which assembling parts bump into each other and stick (glue) together with certain affinity, see Figure 13.

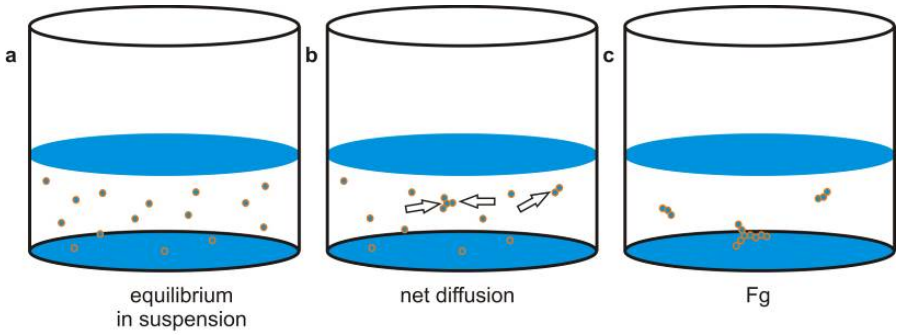

Figure 13: *Assembly in suspension with DLA*. a) Even if suspension is in equilibrium, Brownian motion is always present. b) Therefore, particles can bump into each other also in the diluted suspension, just one at a time. c) Bigger aggregates have higher probability to catch new particles until they sediment due to the gravitational force F_g.

If the sticking probability is the same everywhere the same, it is more likely that a single-particle bump on a straight edge of the aggregate catches a wandering particle due to more unoccupied neighbours, see Figure 14.

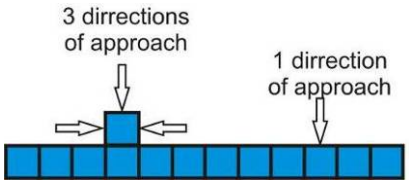

Figure 14: *Sticking probability*. Probability that a new particle is bound on a bump is 3 times bigger than that the new particle is bound on a straight edge.

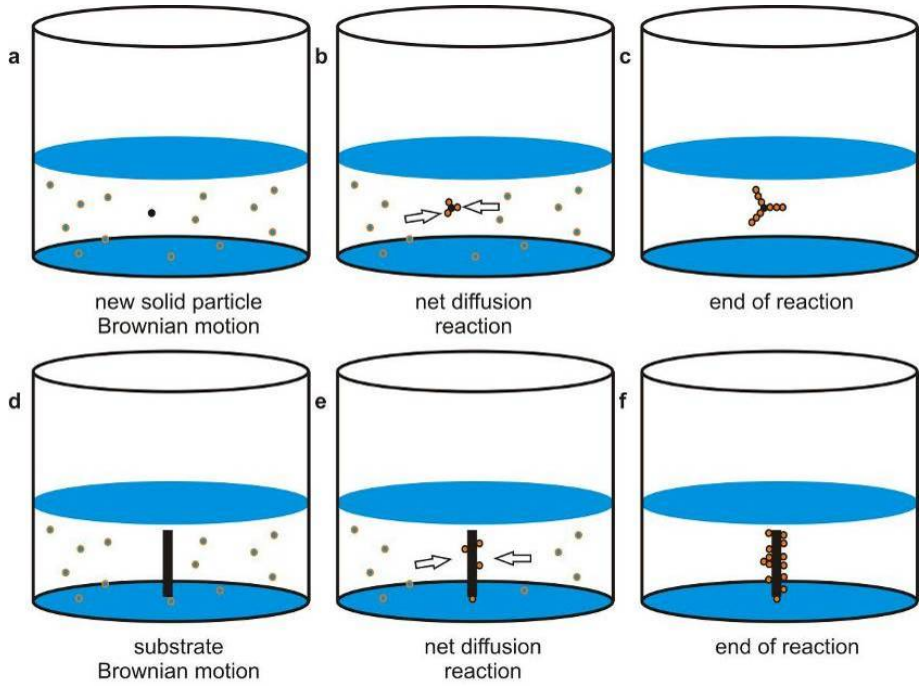

Figure 15: *Assembly in solution with the substrate*. a-c) Aggregation on a nuclei, d-f) aggregation on a substrate. When the soluted material precipitates on the surface of the b) nuclei, e) substrate, concentration of the solution changes and diffusion takes place towards less concentrated part, towards precipitates. c, f) If precipitation takes place with prompt crystallisation, perfect or meso-crystals grow[84]. If precipitation is not connected with crystallisation, there is just aggregation taking place.

Assisted assembly takes place also when introducing a different additional material into the system. This new material functions as the nuclei or/and substrate, where nanoparticles prefer to aggregate or grow from, see Figure 15. If precipitation takes place only on a few crystal planes or if self-assembly can take place after precipitation, perfect crystals can grow (Figure 15c). Otherwise we create only aggregates.

If particles we want to assemble are sensitive to the electromagnetic field, it is possible to use it and assemble material with parallel-plate model capacitor in liquid media, usually in DC circuits, see Figure 16. Problem with this method can be that after electromagnetic field is turned off, assembly falls apart. If assisted assembly is followed by self-assembly, i.e. minimizing the free energy, aggregation is finished in an ordered and thermodynamically stable form.[85]

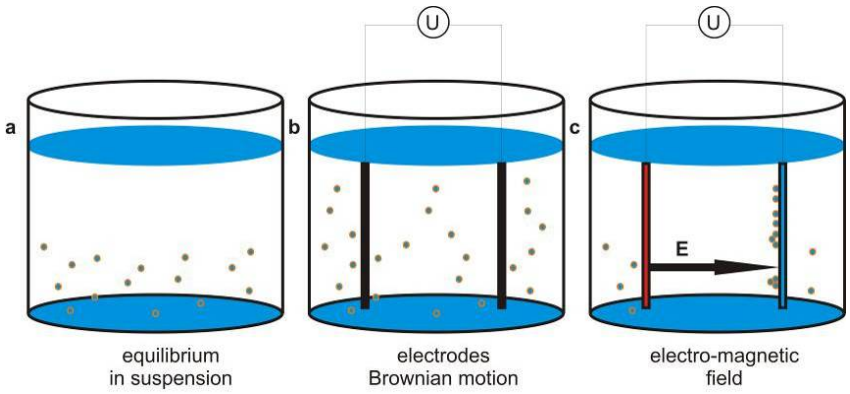

Figure 16: *Assembly in suspension with electro-magnetic fields*. a, b) In the beginning suspension is in equilibrium, and stays in equilibrium until c) the electromagnetic field (**E**) is turned on.

1.3.3 Reported assembly

In the literature can be found several articles on TiO_2 mimicking different organised structures found in nature: from large corals[86], sea urchins[87,88,89,90], cactuses[91], flowers[92,93,94,95], through multi-facet spheres[96] to basic bipyramidal nano anatase crystals[97] and porous materials[98,99,100,101].

F. Guo et.al.[91] prepared with hydrothermal synthesis, at 180 °C for 8 h and titanium n-butoxide as a titanium precursor, cactus-like structures grown on fluorine-doped tin oxide coated glass substrates composed of rods 1 μm to 3 μm long. Glass surface became superhydrophobic when modified with stearic acid and showed non-sticking properties. G. Tian et. al.[92] prepared titanium glycerolate 3D flower-like structures with solvothermal synthesis at 180 °C for 0.5 h to 24 h following the formation and growth from the spheres to the flower-like structures, in ethanol:glycerol (in ratio 3:1) with tetrabutyl titanate as titania precursor, followed by calcination at 450 °C for 3 h along with anatase formation. Average flower's diameter was 1.5 μm. Material showed enhanced photocatalytic activity compared with commercial powder Degussa (Evonik) P25[102]. After 0.5 h of solvothermal synthesis they got amorphous material, titanium oxyhydrate. After 24 h of synthesis there was one sharp peak at cca. 10° on XRD pattern, followed by few weaker peaks. In the JCPDS database there was no know structure containing titanium, but there were some similar to Co etc. - based glycerols. They followed the gradual reaction with glycerol via peak splitting and ratio changes in intensity in XRD measurements. Q. Li et.al.[93] synthesised anatase rods and from rods selfassembled rutile crysanthemums from prepared titanium glycolate rods heated at 400 °C for 4 h in air and in vacuum respectively. Titanium glycolate rods were prepared with

heating the titanium alkoxides in ethylene glycol at 170 °C for 2 h. Diameters of crysanthemus are 150 μm to 200 μm, diameters of rods 1 to 20 μm, rods' length 80 to 100 μm. Y. Masuda et.al.[94] reported self-assembly of flower-like multineedeled TiO_2 structures, measuring 200 nm to 400 nm in diameter, on substrate in mild aqueous conditions with ammonium hexafluorotitanate, boric acid and prepared silicon wafers dried on 50 °C for 19 h and 7 days. Needles were monocrystals of anatase grown along c-axis, with 3.2 eV big band gap, 178 m^2/g. M. Ye et.al.[95] prepared hierarchical rutile TiO_2 flower clusters on a transparent conducting fluorine-doped tin oxide substrate with hydrothermal synthesis on 140 °C for 9 h with addition of cation salt. They observed dependence of the film's thickness and density on the growth time, initial concentration of precursors, growth temperature etc. S. S. Mali et.al.[86] synthesised TiO_2 nanocoral-like thin films on the glass and on the fluorine doped tin oxide coated glass substrates with multi-step hydrothermal synthesis at 120 °C for 3 h to 12 h using titanium chloroalkoxide as a precursor. Corals' average size was 480 nm, average coral polyps' diameter was 30 nm. They observed improved charge transport through TiO_2. J. Wu et.al.[96] reported synthesis of multi-facet anatase spheres of etched single-crystalline anatase by immersing metallic Ti plates in an HF solution under hydrothermal conditions at 180 °C for 1 h to 5 h. The spheres' diameter was approximately 2 μm. X. Wang et.al.[98] studied photocatalysis in gas-phase medium of porous titania structures prepared using titanium tetraisopropoxide as a precursor in aqueous solution of decaoxyethyl ether, aged in autoclave at 80 °C for 24 h, calcinated in static air at 350 °C to 800 °C for 4 h. They found out that porous channels successfully harvest the light and increase the photocatalytic effect. X. Wang et.al.[99] described different preparations of porous titania material i.e. soft templating, hard templating and template-free approaches. Result of soft templating done in different surfactants (ionic liquids, bi-block co-polymers etc.) is TiO_2 with low thermal stability and poor crystallinity, which is not suitable for the photocatalytic applications. Hard templating performed using mesoporous silica materials, carbon nanotubes etc. results in crystalline TiO_2 with specific pore structure and morphology. With template-free procedure mesophorous material is created from TiO_2 aggregates through recrystallization into denser crystalline phase or using entrapped gases. A. Collins et.al.[100] synthesized ordered macroporous amorphous titania with template-free assembly which was achieved by dropping of titanium alkoxides to aqueous ammonia. Pores had diameter from 1 μm to 10 μm and were up to 100 μm long. They proposed mechanisms of creating template-free porous titania if coupling sol-gel reactions with microphase separation, transient hydrodynamic gradients or time dependent diffusion gradients. B. J. Yu et.al.[101] fabricated template-free amorphous hierarchical macro-/mesoporous titania at room tem-perature by the dropwise addition of tetrabutyl titanate to pure water. Material was afterwards calcinated from 300 °C to 800 °C. At 300 °C material transformed into anatase, at 700 °C transformation into rutile was seen, at 800 °C material completely transformed into rutile. Material that was calcinated on 300 °C showed highest photocatalytic activity. The photocatalytic activity of acetone in air greatly decreases when the calcination temperature is higher than 500 °C because of the destruction of porous material and the decrease of specific surface area. Hayashi et.al.[87] synthesised sea urchin-shaped rutile with abundant {110} surfaces at 60 °C for 72 h allowing slow nucleation and crystal growth. There average diameter was 420 nm containing needle-like rutile monocrystal grown from a single nucleus. The material showed better photocatalysis than commercial rutile with the same specific surface area. Wang et.al.[88] hydrothermally prepared tubular nanostructures from TiO_2 powder in NaOH on 160 °C for 30 h. Template-free selfassembly of the nanotubes led to micrometer-scale sea urchin like structures, which were annealed on 300 °C in air. Material had large surface area and ordered electron conduction network when compared

to structures in random arrangement. E.-H. Kong et.al.[89] prepared with solvothermal synthesis see urchin rutile composed from nanowires. Material was tested in quantum dot sensitized solar cell where there was noticeable improvement in power conversion efficiency due to higher photocurrent density. Q. Cheng et.al.[90] hydrothermally synthesised hollow TiO_2 sea urchin like microspheres at 150 °C for 12 h using potassium titanium oxide as a Ti source. Specific surface area 251.2 m2 g-1 (pure TiO_2 particles have 1.5 m2 g^{-1}). Sea urchin like spheres measured approximately in diameter 3 μm, its rhombic building blocks 100 nm.

1.4 Photocatalysis

Photocatalysis is an accelerated photoreaction with a catalyst that, by definition, unlike other substances in the reaction, does not change. It is also not consumed by the reaction itself and can participate as catalysts multiple times. When Fujishima and Honda in 1972 discovered the photocatalytic splitting of water on TiO_2 electrodes[103] research on semiconductive nano TiO_2 spread.

Photocatalysis can be homogeneous or heterogeneous. In the homogeneous photocatalysis, the reactants and photocatalysts are in the same phase, while in the heterogeneous photocatalysis the phase of the catalysts is different from the reactants. When doing photocatalysis with TiO_2, the reaction is always heterogeneous and happens with creation of the radicals with help of the electron-hole pair on photocatalysts surface.

TiO_2 crystals, at least rutile, anatase and brookite, are semiconductors. In Figure 17 all types of materials are compared according to the density of states and their electronic structures. Semiconductor's band gap (Figure 17c-e), dividing the valance and conduction band, is still small enough that electrons can be excited from the valance into conductive band with thermal energy or photoexcitation, while in the case of the insulators that cannot happen due to too high band gap between both bands (see Figure 17f). In the case of the conductors, the valence and conduction bands overlap, so they conduct in their intrinsic state (see Figure 17a, b).

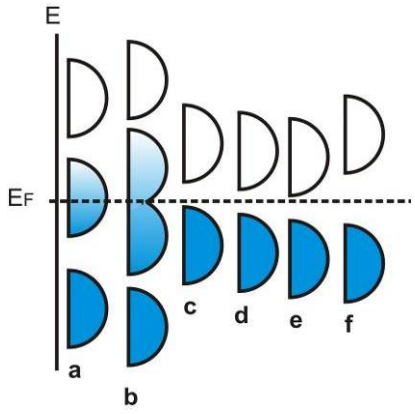

Figure 17: *Density of states in different materials*. Density of states in relation to Fermi level (E_F) in a) metal, b) semimetal, c) p-type of semiconductor, d) intrinsic semiconductor, e) n-type semiconductor and f) in insulator.

There are 3 types of semiconductors depending on the distance between the Fermi level (E_F) and the maximum of the valance band, and the Fermi level and the minimum of the conduction band. If distances are equal, the semiconductor is intrinsic, if the distance between the Fermi level and the maximum of the valance band is smaller than the distance between the Fermi level and the minimum of the conduction band, the

semiconductor is of p-type, otherwise it is n-type. N-type and p-type of the semiconductor can also be prepared with doping of intrinsic semiconductor with new elements.

Anatase was found to be a n-type semiconductor (see Figure 17e) due to its tendency for O vacancies in its lattice. In the laboratory anatase was prepared also as a p-type semiconductor (see Figure 17c) with Ti vacancies.[104]

TiO_2 becomes a photocatalysts after being irradiated with light with energy equal or larger to its bandgap (see Equation 13):

$$h\nu > E_g \tag{13}$$

Where h is a Planck's constant, ν is the frequency of the light and E_g is the band gap. In Table 8 the lowest energies of impact photons, measured and calculated, are listed, which are needed to excite electrons from valance to unoccupied conducting band leaving behind positive holes, see Figure 18. These photons come from UV part of the solar spectrum (387.5 nm for anatase[105]).

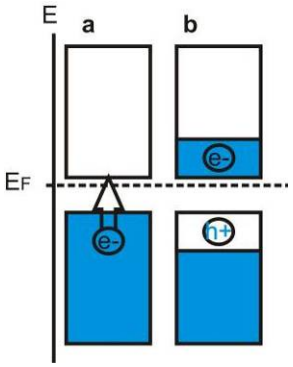

Figure 18: *Conduction of semiconductor*. a) Semiconductor in basic state does not conduct due to unfilled conduction band gap. b) After excitation of electrons (e^-) into conduction band, leaving behind positive holes (h^+), semiconductor begins to conduct.

It was calculated at the centre of the unit cell Γ that band gap, E_g, of the anatase is indirect (Figure 19b), while rutile and brookite have direct band gaps (Figure 19a).[28]

Photon can directly emit the electron only when the band gap is direct. When the band gap is indirect, the electron still gains the required energy to get into the excited state from the photon, but the electron also has to interact with the lattice to gain or loose momentum. This transition is called phonon assisted transition.

Recombination, like excitation, proceeds at a much slower rate in case of the indirect band gap, giving the electron-hole pair of the anatase longer life-time when compared to brookite and rutile.

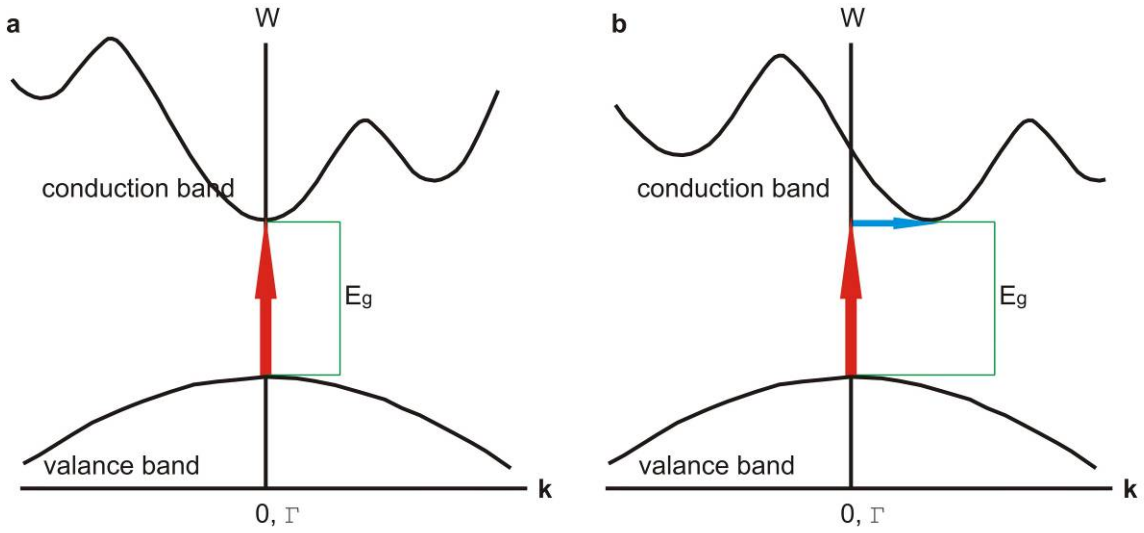

Figure 19: *Band gap of a semiconductor*. a) Direct band gap, E_g, where **k** vectors of valance and conduction band are the same, and b) indirect bang-gap, E_g, where **k** vectors of valance and conduction band are different.

Semiconductor exhibits minimal optical absorption for photons with energies smaller than the bandgap and high absorption for photons with energies greater than the bandgap[106], as can be seen in Figure 20. The result is a sharp increase in absorption at energies close to the bandgap which can be estimated from Equation 14 and 15:

$$\alpha\hbar\omega \propto (\hbar\omega - E_g)^{1/2} \quad (14)$$

$$\alpha\hbar\omega \propto (\hbar\omega - E_g)^{2} \quad (15)$$

Where α is an absorption coefficient, measured in Figure 20, ħ is a reduced Planck's constant ($\hbar=h/(2\pi)$), ω is an angular momentum ($\omega=2\pi\nu$, where ν is light frequency), E_g is the energy of the band gap.

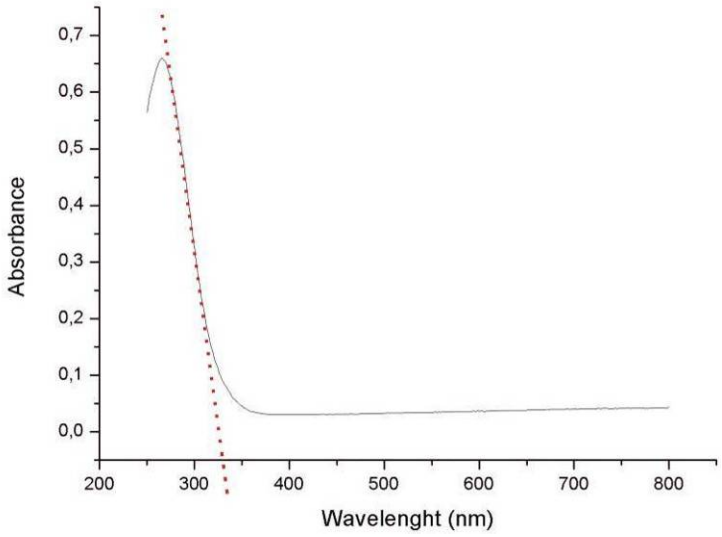

Figure 20: *Band gap measurement*. Band gap can be estimated from the absorption spectrum from tangent line versus the energy of the light.

Negative electron (e^-) in conductive band and positive hole (h^+) in valance band represent charge carriers. They can recombine nonradiatively, radiatively (heat) or get

trapped and react with electron donors or acceptors absorbed on the surface of the photocatalyst. If charge separation is maintained, the electrons and holes can migrate to the catalyst surface where they participate in redox reactions with adsorbed species. In particular, hole h^+ may combine with H_2O or OH^- to produce the hydroxyl radical ($HO^\bullet$), see Equation 16:

$$H_2O + h^+_{VB} \rightarrow HO^\bullet_{ads} + H^+_{ads} \tag{16}$$

e^- in conduction band (e_{CB}^-) can be picked up by oxygen (O_2) to generate superoxide radicals ($O_2^{\bullet-}$) which can in turn generate hydroperoxide ($HO_2^{\bullet-}$) and hydrogen peroxide (H_2O_2), decomposed at the semiconductor surface into hydroxyl radicals ($HO^\bullet$), see Equation 17:

$$\begin{aligned} &O_{2(ads)} + e^-_{CB} \rightarrow O^{\bullet-}_{2(ads)} \\ &O^{\bullet-}_{2(ads)} + H^+_{ads} \rightarrow HO^{\bullet-}_{2(ads)} \\ &HO^{\bullet-}_{2(ads)} + e^-_{CB} + H^+_{ads} \rightarrow H_2O_{2(ads)} \rightarrow 2HO^\bullet_{ads} \end{aligned} \tag{17}$$

These very reactive radicals can oxidize the adsorbed organic pollutants to achieve complete decomposition, i.e. decomposition into minerals, H_2O and CO_2.[107]

Photocatalytic activity (γ), in units (mol m^2)/(g s W), is proportional to the concentration of the pollutant (C) in units mol/l, inversely proportional to the irradiation time of UV light (t), to the concentration of TiO_2 particles (m), in units g/l, and to the intensity of adsorbed UV light (I), in units W/m^2,see Equation 18[108]:

$$\gamma = \frac{C}{3tmI} \tag{18}$$

The photocatalytic properties of TiO_2 are affected by several factors: crystal structure, morphology and surface area. The highest photoactivity among all 3 most common and pure TiO_2 crystal structures shows anatase. Proper mixture of anatase and rutile TiO_2 gives however higher photocatalytic activity than pure anatase.[109]

If TiO_2 is doped with metal oxide it becomes photocatalytic under visible light, where the intensity of the light is much higher than in the UV part of the solar spectrum.[109,110,111,112,113,114,115] There are even some new materials (TiOBCN) related to TiO_2 which have even bigger photoreactive spectral span of light.[116]

The efficiency of photocatalysis depends also on the pH of the reaction solution. The surfaces charge properties of TiO_2 change with pH. In acid conditions, the surface of TiO_2 is positively charged, in alkaline negatively.[117]

TiO_2 does not show only photocatalytic capability but also photocorrosion stability which is needed to perform reactions.[118]

2 Aims and Hypothesis

The aim of the doctoral thesis was to explore the processes of nucleation and crystal growth during the hydrothermal synthesis of TiO_2 and thus control the composition, structure and surface properties with the optimization of the preparation parameters. We tried to produce crystals of different sizes, shapes and morphologies, with good photocatalytic properties. Our purpose was to build larger structures through the assembly of these crystals, which would not have negative impact on environment and health, but would still be useful for photocatalysis.

TiO_2 represents nowadays the material which is used for self-cleaning of indoor and outdoor surfaces. Problem after and between the self-cleaning procedure can represent weak attachment of TiO_2 nanoparticles on the surface, which leads to unnecessary pollution of environment with health-risk nanomaterial. Even if TiO_2 is used as photocatalysts in liquid media, removing nanoparticles after photocatalysis can represent a major problem.

As crystalline nano TiO_2 on one hand degrades organic volatile and dangerous compound, if left uncontrolled in the environment, it can create even more volatile compounds, not reach the complete degradation or even it can degrade nonharmful or even for life useful organic compounds to toxic ones. If there is no way of complete isolation or removal of nano TiO_2 particles from the environment, there is a danger not just due to nanoparticles toxicity but also the possibility that we lose the control over its photocatalytic activity.

To avoid additional pollution with nano TiO_2, material has to be firmly bonded on larger surfaces (substrates) or it has to be grown or aggregated in the way that the clusters are big enough to be easily filtered, sedimented with gravity, etc. At the same time, aggregates have to be hard to break apart and still they should have large specific surface area.

With the control of the nucleation and growth of the nano-crystals of TiO_2, with a certain morphology and size, we can tailor the physical properties such as the photocatalytic effect. {001} planes have the highest surface energy in anatase crystals [119], so we expect that the particles with the largest share of planes {001} are the most photocatalytic, see Figure 21.

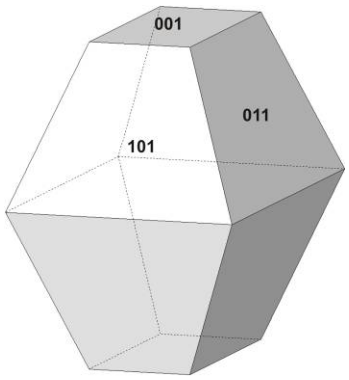

Figure 21: *Truncated bipyramidal anatase*. Truncated bipyramidal anatase with labelled outer planes: (101), (011), which are equal, and (001) which has the highest surface energy.

With assisted assembly or with self-assembly of the correspondingly shaped nanoparticles of TiO_2 it might be possible to prepare larger ordered structures which still have the desired properties like photocatalytic ability, see scheme in Figure 22.

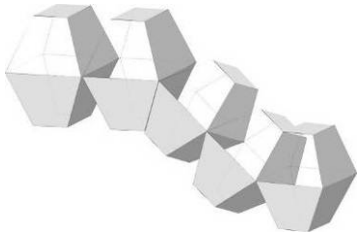

Figure 22: *Assembly of truncated bipyramidal anatase crystals*. Scheme of assembly of TiO_2 nanoparticles.

However, with assembly the surface-volume ratio should not get too small, because the photocatalytic properties are then lost, due to less surface becoming available for interactions with the degrading substances, see Figure 23, where volume is constant, and only surface increases with particles getting smaller.[120]

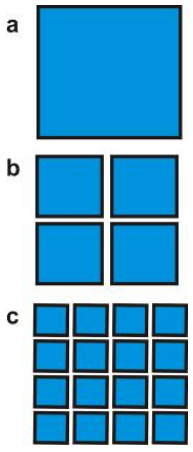

Figure 23: *Nano and macro particles*. a) Bulk material with surface "4a", where "a" represents 2D surface area in 2D model, volume $V=a^2$, b) smaller bulk material with surface "8a", volume $V=a^2$, towards c) nanomaterial with surface "16a", volume $V=a^2$.

3 Materials and Methods

For preparation of TiO_2 crystals, we used different solvents, solutes, additives (surfactants) and techniques of synthesis, like sonochemical treatment, sol-gel synthesis, low-temperature synthesis and hydrothermal treatment at different conditions (temperature, pressure, time of synthesis).

After synthesis we performed microstructural and photocatalytic analyses with different techniques and instruments. Shape, surface area, degree of crystallinity and crystal modification were determined by electron microscopes (transmission and scanning). Defects in the crystal structure and the surface of the particles were studied with the atomic level methods of high-resolution transmission electron microscopy (HRTEM) and microanalysis, i.e. energy-dispersive X-ray spectroscopy (EDXS) and selected area electron diffraction (SEAD). Photocatalytic properties were measured using irradiation chamber and UV-Vis spectrophotometer. Crystal modification and the size of the crystals were determined besides the electron microscopy also with the X-ray powder diffraction (XRD). Size of the agglomerates was measured by dynamic light scattering (DLS).

3.1 Materials

We started our first experiments using commercial TiO_2 powders, which were impossible to reduce in size, to assemble in ordered bigger structures and to change its properties, especially the photocatalysis. With the lack of information about their synthesis, which would help us to overcome our experimental difficulties with those powders, it was logical to start preparing our own powders from the liquid precursors.

Basic precursor in our experiments was Ti (IV) isopropoxide, $Ti(OR)_4$, (TO), 98+ %, from Acros Organics. It immediately hydrolyses in water, see Chapter 2.3. Distilled water (home prepared), was our basic solvent. Besides distilled water we also used methanol for analysis, from Merck, absolute anhydrous ethanol, from Carlo Erba, which both contained traces of water (the hydrolysis took place immediately), 2-propanol, 99.8+ % from Sigma Aldrich, which was used to dilute TO, and glycerol, 99.5+ %, from Sigma-Aldrich

For testing photocatalysis we used resazurin, dye content 92 % from Sigma-Aldrich, along with hydroxyethyl-cellulose from Sigma-Aldrich; and caffeine, 99.0+ % from Sigma-Aldrich.

3.2 Modified sol-gel synthesis

When starting from the TO, it always followed sol-gel synthesis (except in 2-propanol, which just diluted the TO and gave possibility to dip coat thinner films). We modified the sol-gel synthesis by stopping the sol-gel part of synthesis before gelation (second step in Procedure 1, Figure 24c), allowing only hydrolysis to take place.

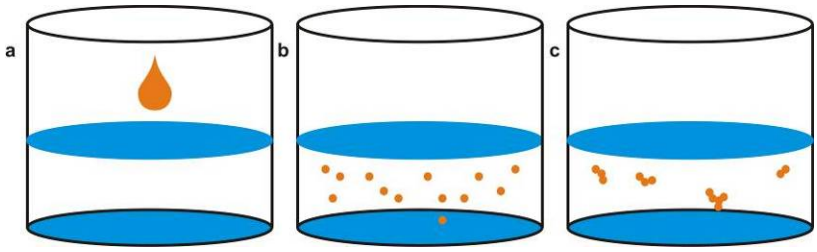

Figure 24: *Sol-gel synthesis*. Sol-gel synthesis takes place in several steps. a) mixing compounds, b) formation of the sol, c) which gels with time.

The experiment, where we tested the aging effect in the amorphous suspension was also performed. The suspension was kept in a closed vessel in dark at the room temperature. We followed that experiment for 9 months.

Preparation of nanoanatase crystals started with the addition of up to 100 ml of distilled water to up to 5 ml of TO, which were mixed and then stirred at room temperature. Isopropoxide immediately hydrolysed, forming an amorphous precipitate, see Equation 19:

$$\begin{aligned} Ti(OR)_4 + 4H_2O &\rightarrow Ti(OH)_4 + 4ROH \\ Ti(OH)_4 &\rightarrow TiO_2 + 2H_2O \end{aligned} \qquad (19)$$

In the first step titanium hydroxide ($Ti(OH)_4$) monomers are formed and in the second step the formation of TiO_2 occurs with nucleation and crystal growth.[121]

The suspension was repeatedly centrifuged, filtered and washed with distilled water until constant conductivity and pH values <5 were reached (Knick Portamess 913(X) instrument was used for conductivity and pH measurements. Finally, after the last filtration, distilled water was added, filling up the volume of filtrate to 50 ml, for hydrothermal (HT) experiments.

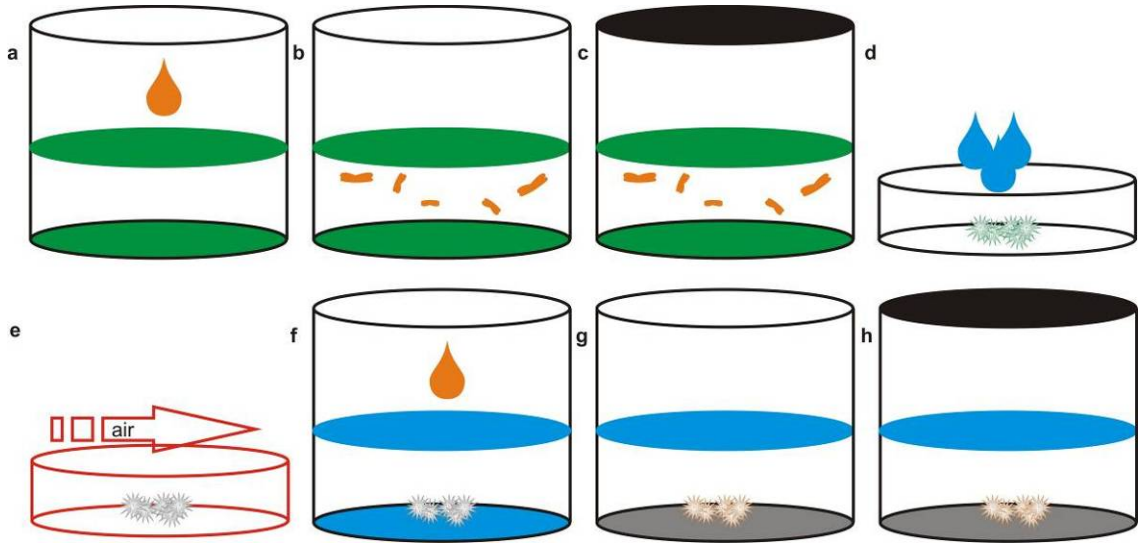

Figure 25: *Experimental procedure for preparation of flower-like TiO_2 structures coated with nanoanatase*. a) TO was poured into glycerol. b) Slow hydrolisation of TO. c) Solvothermal synthesis was performed d) Material was washed with distilled water and ethanol, filtered, dried in air and e) calcined in air up to 600 °C. f) To the prepared material in the distilled water we added TO and g) hydrolysis. h) Hydrothermal synthesis.

When preparing micro flower-like TiO_2 structures, see Figure 25a-e, 5 ml of TO was

injected into 50 ml of glycerol that was already in the autoclave's Teflon vessel. After 5 minutes, 2 ml of distilled water were added during stirring. The solution was solvothermally treated and afterwards washed, filtered, dried and calcined.

Attachment of anatase crystals on flower-like TiO_2 structures, see Figure 25f-h, started with adding of 0.01g to 0.1 g of calcined flower-like powders, and 0.5 ml of TO to the 50 ml of distilled water, which was already in the autoclave's Teflon vessel. After the addition, the TO immediately hydrolyzed. The suspension was hydrothermally treated.

3.3 Hydrothermal synthesis

Hydrothermal experiments were performed in a metallic autoclave with inner 110 ml Teflon vessel and heated in the furnace APT. line™ FED with R3.1 controller from Binder, see Figure 26. The parameters we changed were the conditions of the synthesis (time, temperature, i.e. pressure). The filling of the vessel was 50 volume % in all experiments.

Figure 26: *Autoclave*. Metallic autoclave (on the inset) with inner Teflon cartridge in the furnace.

When preparing nanoanatase crystals from aqueous suspension of amorphous TiO_2, hydrothermal synthesis, see Figure 27, at temperatures from 20 to 200 °C was used. The estimated heating rate was 10 °C/min and the heating time was from 50 to 200 hours. The autoclave was spontaneously cooled down to room temperature in a furnace within 24 hours.

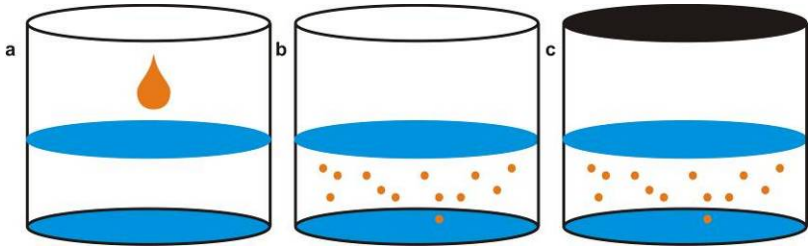

Figure 27: *Hydrothermal synthesis*. a) After mixing compounds in the Teflon vessel, and after b) creation of a sol, c) the vessel is well closed and put into furnace for hydrothermal synthesis.

In one set of experiments we used a cyclic approach, see Table 13, where particles, synthesized at one temperature were used as an input material for another experiment at a 10 °C higher temperature (processing times for all cycles were 100 hours). The synthesis

started at room temperature, increasing the temperature up to 100 °C in steps of 10 °C. After each step we cooled closed autoclave to room temperature, took out a sample for TEM studies and returned the rest of the material for the next HT cycle at higher temperature. In last two experiments the material was heated at 150 and 200 °C for 100 hours. The autoclave was cooled down to room temperature in furnace within 24 hours spontaneously.

Table 13: *Cyclic hydrothermal synthesis*. Starting the experiment from 20 °C, with steps of 10 °C, until 100°C. In the last two experiments the material was heated at 150 and 200 °C for 100 hours.

No. synthesis	T [°C]	t [h]
1.	20	100
2.	30	100
3.	40	100
4.-8.	50-90	100
9.	100	100
10.	150	100
11.	200	100

The synthesis of hierarchical structures based on flower-like particles, enriched with nanoanatase TiO_2, hydrothermal synthesis, that followed the sol-gel synthesis, was performed in a steal autoclave in Binder APT lineTM FED furnace at 120 and 200 °C for 12 h. The autoclave was cooled down spontaneously to room temperature in furnace within 24 hours.

3.4 Solvothermal synthesis

Solvothermal synthesis was performed in the same route as hydrothermal synthesis, but instead of the distilled water we used nonaqueous solvents.

When preparing flower-like TiO_2 structures, the sol-gel procedure was followed by solvothermal treatment in a steal autoclave with 110 ml inner Teflon vessel at 180 °C and 200 °C for 24 h in the furnace Binder APT. lineTM FED. Obtained white viscose suspension was mixed with 50 ml of distilled water and centrifuged at 5000 rpm for 5 min. White supernatant was removed. Cleaning procedure with distilled water was repeated 5 times and 5 times with ethanol. Suspension was dried for 24 h at 60 °C.

3.5 Treatment with ultrasound

We used ultrasound see Figure 28, to break the bonds in the aggregates before doing microstructural analysis and characterisation, especially for TEM investigation. Ultrasounds were created in ultrasonic bath Sonis 4, from Iskra pio d.o.o., and with more powerful UP400S Ulrtasonic processor, from Hielsher.

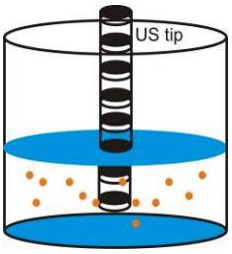

Figure 28: *Sonochemical synthesis*. After mixing compounds, suspension is exposed to pulsed microwave radiation coming out from the ultrasonic (US) tip in the middle of the suspension.

3.6 Calcination

Remnant from solvothermal synthesis was calcined, see Figure 29, in air in Nabertherm P330 furnace at 300, 350, 400, 450, 500, 550 and 600 °C for 48 h. The as-prepared material was afterwards used as additive for hydrothermal synthesis.

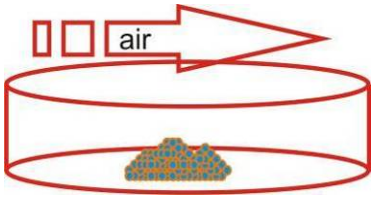

Figure 29: *Calcination*. Material in Al_2O_3 vessels is put into furnace with air flow.

3.7 Microstructural analysis and characterisation

The shape, morphology, degree of crystallinity, crystal modification and crystal growth were determined by electron microscopes (transmission, TEM, and scanning, SEM). Defects in the crystal structure and the surface of the particles were studied at the atomic level with high-resolution transmission electron microscopy (HRTEM). With high resolution TEM images, the shape of crystals was reconstructed. Chemical microanalysis was performed with energy dispersive X-ray spectroscopy (EDXS), selected area electron diffraction (SAED) was used for crystal structure determination.

Crystal modification and the size of the crystals were determined also with the X-ray powder diffraction (XRD). The size of agglomerates was measured by dynamic light scattering (DLS). Organic compound remediation was followed by Fourier transform infrared spectroscopy (FTIR).

3.7.1 SEM

TiO_2 nanoparticles and hierarchical structures were investigated under the scanning electron microscope (SEM), presented in Figure 30.

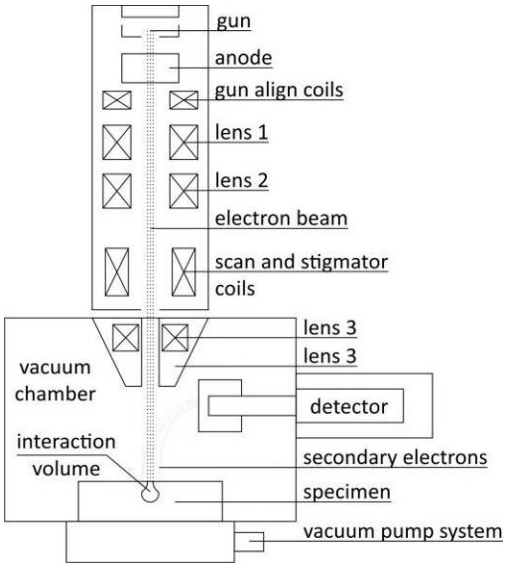

Figure 30: *SEM*. All parts of scanning electron microscope (SEM). Courtesy of Janez Zavašnik.

Powders were diluted in ethanol or distilled water and the suspension was dropped onto the glass or graphite support. When the sample dried, we sputtered gold or carbon thin film onto the surface using Balzers SCD 050 (Bal-Tec) or Gatan 682 PECS sputter coaters.

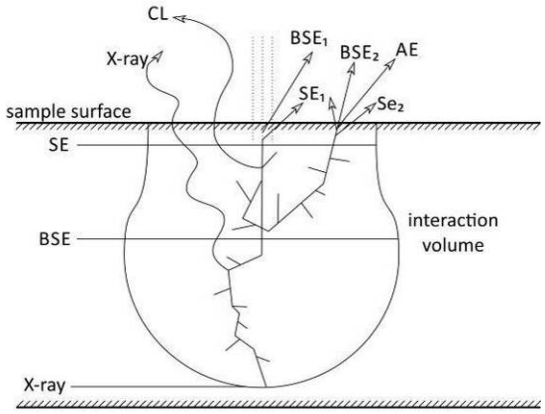

Figure 31: *Interaction volume*. Interaction volume depends on the energy of incoming electrons. Secondary electrons show mainly the surface of the investigated material, back-scattered electrons carry information regarding the atomic number of elements present and are coming from deeper parts of the interaction volume. X-rays could penetrate from even deeper parts and are used for the identification of the elements present. Courtesy of Janez Zavašnik.

Gold was sputtered if we focused on sample's surface. If we wanted to focus on the chemical elements present in the interaction volume (Figure 31) using energy-dispersive X-ray spectroscopy (EDXS), carbon was sputtered on the samples surface, because peaks of Ti and Au overlap.

We used 2 different conventional scanning electron microscopes with tungsten ion source JXA-840A from JEOL with secondary and back–scattered electrons (SE-BSE) detectors and EDXS, WDXS system, TN 5600, from Tractor Northern, and JSM-5800 from JEOL, with SE-BSE detectors and EDXS system ISIS 300 from Oxford Instruments.

3.7.2 FEG-SEM

For high magnifications we used SEM with more powerful electron source, i.e. filed-emission gun scanning electron microscope (FEG-SEM) JSM-7600F from JEOL with EDXS system INCA from Oxford Instruments. With FEG-SEM we investigated surface and shape of prepared nanoparticles.

3.7.3 TEM

When preparing samples for investigation by transmission electron microscope (TEM), which is presented in Figure 32, we diluted powders in ethanol for quicker drying and broke bonds in aggregates with ultrasound.

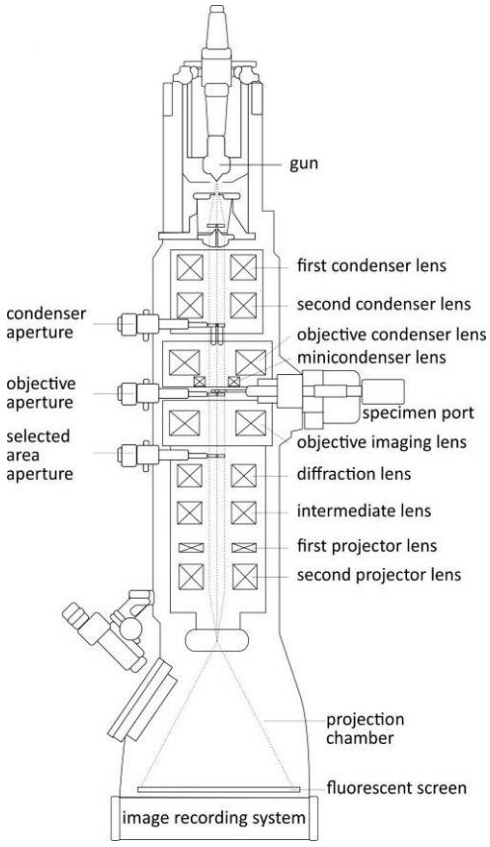

Figure 32: *TEM*. Parts of transmission electron microscope (TEM). Courtesy of Janez Zavašnik.

Maximal time in the ultrasonic bath was 15 min, maximal time in ultrasonic processor just 5 min, with 0.5 amplitude. A drop was deposited onto the holy carbon-coated Cu-grids (for heating experiment we used Ni-grids), which was in a petri dish. We let the ethanol to dry in air.

Samples were investigated by TEM JEM-2010F from JEOL with field-emission electron source and EDXS system ISIS 300 from Oxford Instruments, and with TEM JEM-2100 from JEOL, with LaB6 source and with EDXS system from JEOL. With JEM-2100 we performed also the heating experiment with double tilt heating holder model 652 from Gatan, with Smart set hot stage controller model 901 from Gatan, and with water cooling unit from Gatan, which is needed when temperatures exceed 500 °C.

Material was investigated at spot size 1 and using biggest condenser aperture. If we

observed a specific part of crystalline TiO_2 for a longer time, the damage was seen on the material.

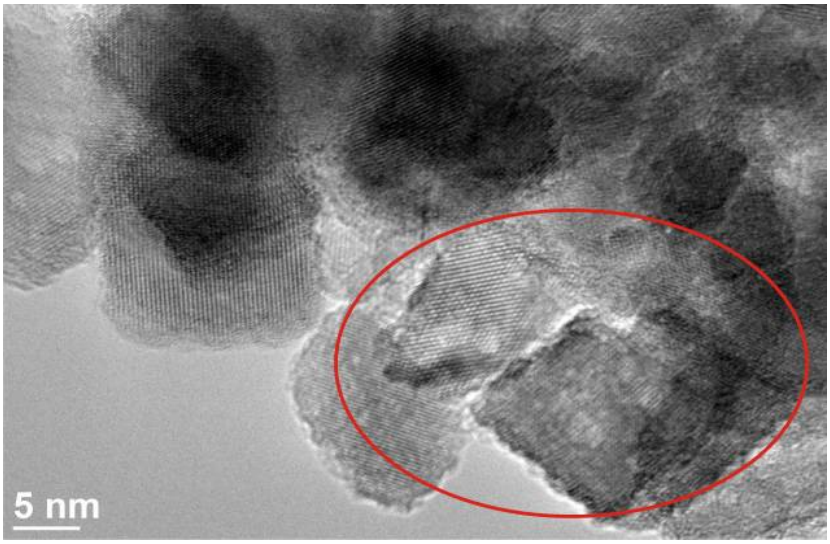

Figure 33: *TEM damage on the material*. When material was observed under TEM (this photo was taken in HRTEM mode) for too long at harsh conditions, the damage made by electron beam was observed in the material.

To avoid the damage created under too harsh conditions for the material with electron beam, we had to change spot size to 2 or 3 and/or decrease the brightness (spread the radius of the electron beam which falls onto the specimen).

3.7.4 HRTEM

In TEM with sufficient resolution, when magnification is higher than ~400 000, the crystal lattice image could be obtained. This imaging mode is called high resolution TEM and is produced due to the interference of the diffracted electron beams. In this mode, if crystals were oriented in the way that the atom columns were parallel to the electron beam, we could see atomic structure and determine the planes using fast Fourier transformation (FFT). With such imaging we can recreate (reconstruct) a 3D model of the crystal.

Conditions needed to work in HRTEM mode and not damage the material were spot size 2 or 3 or/and decrease of brightness, if we were investigating one area of the material for a longer time. Usually we decreased the brightness and after the damage happened, we searched for another area to work on. This was possible because our material was in powder form with a lot of crystals on the grid, so we could find other similar areas.

3.7.5 SAED

Selected area electron diffraction can be performed using TEM. As a result we get the projection of the reciprocal space of the thin specimen.

From the diffraction pattern we can determine whether the sample is amorphous (wide foggy circles), crystalline (dots or circles), polycrystalline (circles) or if we are dealing with a monocrystal (dots). We can identify the crystal structure (measuring the d-values of different crystal planes), determine the symmetry and study crystal defects (precipitates, planar defects, dislocations, stacking faults), etc.

3.7.6 EDXS

All used TEM and SEM microscopes are equipped with energy dispersive X-ray spectroscopy (EDXS) units which we used for elemental chemical analysis.

With EDXS equipped SEM we performed analysis on a bigger area, when doing analysis with EDXS installed on TEM, the analysis was far more precise.

With this analysis we were able to determine possible impurities inside the titania.

3.7.7 XRD

X-ray powder diffraction (XRD) was performed with PANalytical X'Pert PRO system. The method was used to determine the TiO_2 crystal phase (or if the material was amorphous) and to estimate the size of the crystals in (hkl) directions which correspond to (hkl) detected peaks using Scherrer equation, see Equation 1. XRD patterns were collected measured from 5° to 75°, in step of 0.04°, where step time was 1 s at temperature 25 °C. The step time was bigger if nanoparticles had average diameter below 10 nm.

3.7.8 FTIR

Organic compound decomposition was followed by Fourier transform infrared spectroscopy (FTIR) with PerkinElmer 2000 FTIR spectrometer. Peaks in the FTIR spectrum correspond to vibrations of bonds between the atoms in the molecule or as in our case, in the unit cell. These vibrations are measured with following the absorption of the light in dependence of its wavelength.

3.7.9 DLS

Size of agglomerates in suspension was measured by dynamic light scattering (DLS) with Vasco S/N instrument from Corduan technologies. Monochromatic light beam causes Doppler shift on spherical particles in Brownian motion. Change of the wavelength is related to the particle size.

3.8 Photocatalysis

Photocatalytic activity of prepared materials was tested with resazurin and caffeine. We always performed a blank experiment, where we checked the photolysis (degradation under UV light without catalyst, i.e. without TiO_2), and a test with the commercial Degussa P25 TiO_2 powder containing rutile, anatase and amorphous phase[102], for the comparison of the photocatalytic effect.

Test with blue oxidized redox-dye resazurin was mainly performed to test the photocatalytic activity at site due to the quick reaction from blue resazurin into pink resorufin and due to the change of the colour in the visible part of the light spectrum, see Figure 34a. This is a quick experiment with which we choose samples for further and

more precise tests with colourless caffeine. Degradation of the caffeine can be followed just by instrumental measurements, because there is no change in colour in visible part of the spectrum.

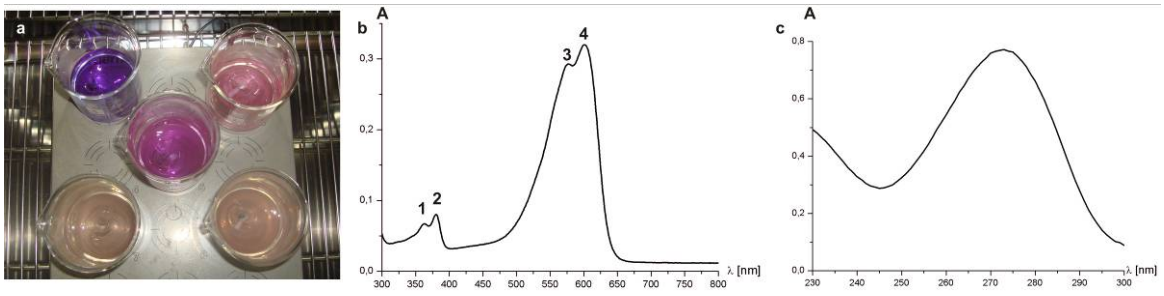

Figure 34: *Blue resazurin, pink resorufin and caffeine*. a) Blue resazurin changes into resorufin with photocatalysis. Pink resorufin degrades further on into colourless substance. b) UV-Vis spectrum showing the conversion of resazurin into resorufin (1, 2 and 4 peaks correspond to resazurin and 3 to resorufin), λ is wavelength of the light, A is the absorbance. c) UV-Vis spectrum of the caffeine.

Resazurin was prepared from 0.01 g of resazurin powder, 0.4 g of sacrificial electron donor glycerol, 0.06 g of aqueous polymer hydroxyethyl-cellulose, 3.9 g of distilled water, and stirred for 30 min.

10 ppm caffeine solution was prepared from caffeine powder in distilled water.

When doing tests with resazurin, we added 0.02 g of tested material (TiO_2) into constantly stirred 50 ml of distilled water and 100 µl of prepared resazurin. When testing photocatalytic effect with caffeine, 0.01 g of tested powder was added into constantly stirred 30 ml of 10 ppm solution of caffeine, see Figure 35a.

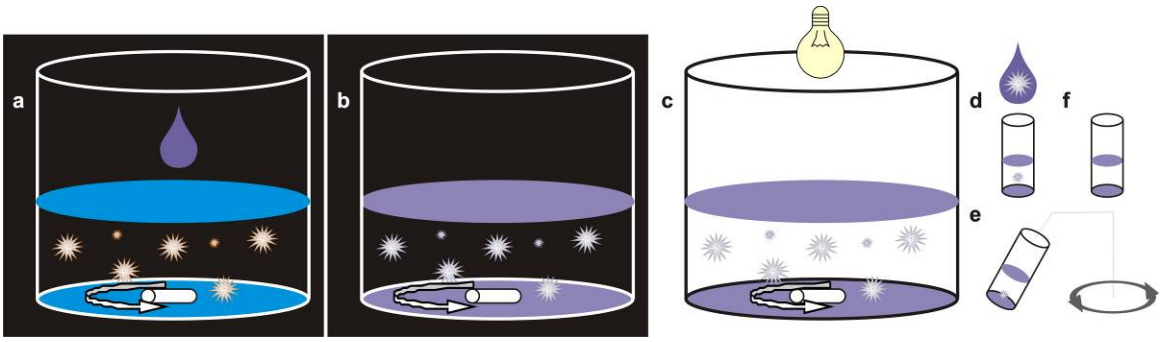

Figure 35: *Photocatalytic experiment*. a) To constantly stirred suspension containing photocatalysts resazurin/caffeine was added. b) The adsorption/desorption of resazurin/caffeine on the photocatalytic powder was in equilibrium after 30 min in the dark. c) Light was turned on and the photocatalysis started. d) Samples with resazurin/caffeine and photocatalysts were taken, e) and were immediately centrifuged to f) remove the photocatalysts and end the photocatalysis before testing the remained concentration with UV-Vis spectrophotometer.

We left suspension stirring in the dark, see Figure 36b, in UV - irradiation chamber (incubator I-265 CKUV from Kambič), i.e. chamber with cooling and heating possibility, equipped with different bulbs (300 W Ultra Vitalux lamp with solar spectrum without UVC, Osram L18/73 with the Gauss spectrum with the peak around 375 nm, and Osram HNS 25 W OFR with 264 nm delta function), at 20 °C for 30 min to let the resazurin/caffeine adsorption/desorption rate on the powder surface get into equilibrium. We took 2 ml of the sample at 0, 5, 10, 15, 30, 60, 120 and 180 min from the beginning of the UV-light irradiation with Osram's Ultra Vitalux bulb with approximate solar spectrum without UVC at 20 °C, see Figure 36c. All taken samples were immediately centrifuged

with 10000 rpm, with Minispin centrifuge from Eppendorf, to remove TiO_2 powder from the liquid, see Figure 36d-f. Degradation of the caffeine was measured with PerkinElmer's UV/Vis/NIR spectrophotometer Lambda 950.

The photocatalytic activity was determined using PerkinElmer UV-Vis spectrophotometer Lambda 950 with a 150-mm sphere in absorbance mode. Measurements were performed from 300 nm to 800 nm for resazurin, see Figure 34b, and from 230 nm to 300 nm for caffeine, see Figure 34c.

When resazurin is changing into resorufin, resazurin peaks labeled by 1, 2 and 4 in Figure 34b decrease, resorufin peak labeled by 3 in Figure 34b increases. But after a while it also starts to decrease because resorufin is not the final product in photocatalysis of resazurin. Determining the photocatalytic effect is not done from the second peak labelled by 3 and 4, because it is combined from resazurin and resorufin parts and the deconvolution could bring along new error. This error could be avoided if the effect would be calculated from the surface area under the first peak labelled by 1 and 2, which is pure resazurin. On the other hand, caffeine has only one peak, see Figure 34c, under which we calculated the surface area to follow the changes in concentration of the remaining, i.e. not yet degraded, caffeine.

3.9 Band gap estimation

With UV-Vis spectrophotometer Lambda 950 from PerkinElmer with a 150-mm sphere in reflectance mode we estimated the band gap values for anatase anatase and other photocatalytic active materials (ZnO). Absorbance spectrum, $A(\lambda)$, see Figure 20, where λ is the wavelength of the incident light, and A the measured intensity, we transformed measurement into $[A(\hbar\omega)\bullet\hbar\omega]^2$, Equation 14, where $\hbar$ is the reduced Plancks constant, $\omega=2\pi\nu$ the angular frequency of the light. From linear plots of the characteristic curve we estimated the band gap value from the projection of the intersection of both linear plots.[122]

3.10 BET measurement

Brunauer-Emmet-Teller (BET) analysis was performed with Gemini 2370 V5 instrument. With adsorption of N_2 gas on a solid surface of tested materials, we estimated the surface area in unit m^2g^{-1}.

4 Results

4.1 Nucleation and growth of nanocrystals

In starting aqueous suspensions, after sol-gel synthesis, the first precipitate (probably titanium-based hydroxides and/or oxyhydroxides) was always amorphous, see Figure 36a. In some areas of HRTEM images it was possible to observe ordered structures of one to few nanometres in size (red circle in Figure 36a), represented by their distinct lattice fringes. Although the material did not appear to be very beam sensitive, crystallization of these areas could still be triggered by electron irradiation.

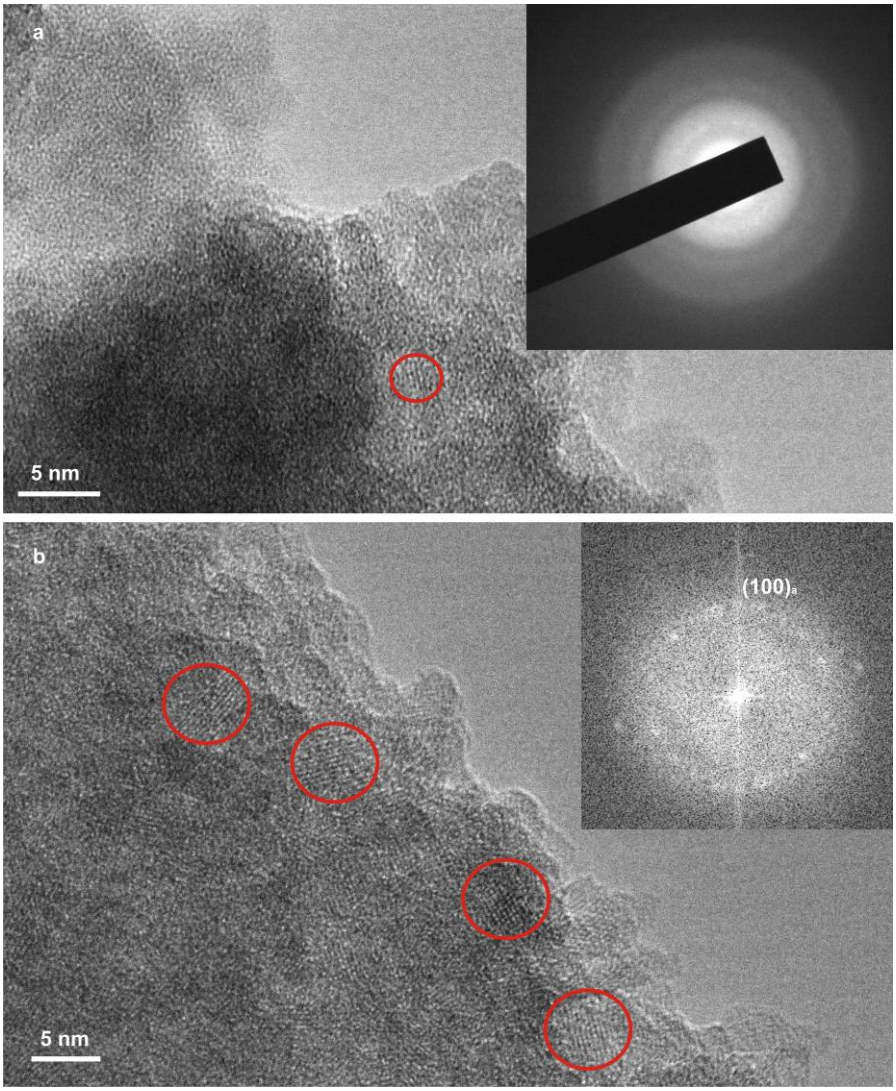

Figure 36: *HRTEM micrographs of amorphous sol-gel material before and after aging*. a) HRTEM micrograph of amorphous TiO_2 before hydrothermal synthesis with selected area electron-diffraction pattern (SAED) in the inset. b) HRTEM micrograph of starting TiO_2 9 months after precipitation with fast Fourier transform (FFT) indicating formation of anatase crystals.

Crystallisation started spontaneously at room temperature in the sol-gel amorphous suspension, see Figure 36b, if the suspension is kept for a prolonged time. Aging was followed up to 9 months. The material started to crystallise, red circles in Figure 36b, in anatase form, see the Fourier transform of the HRTEM micrograph on the inset in Figure 36b where spots representing (100) planes in anatase are labelled.

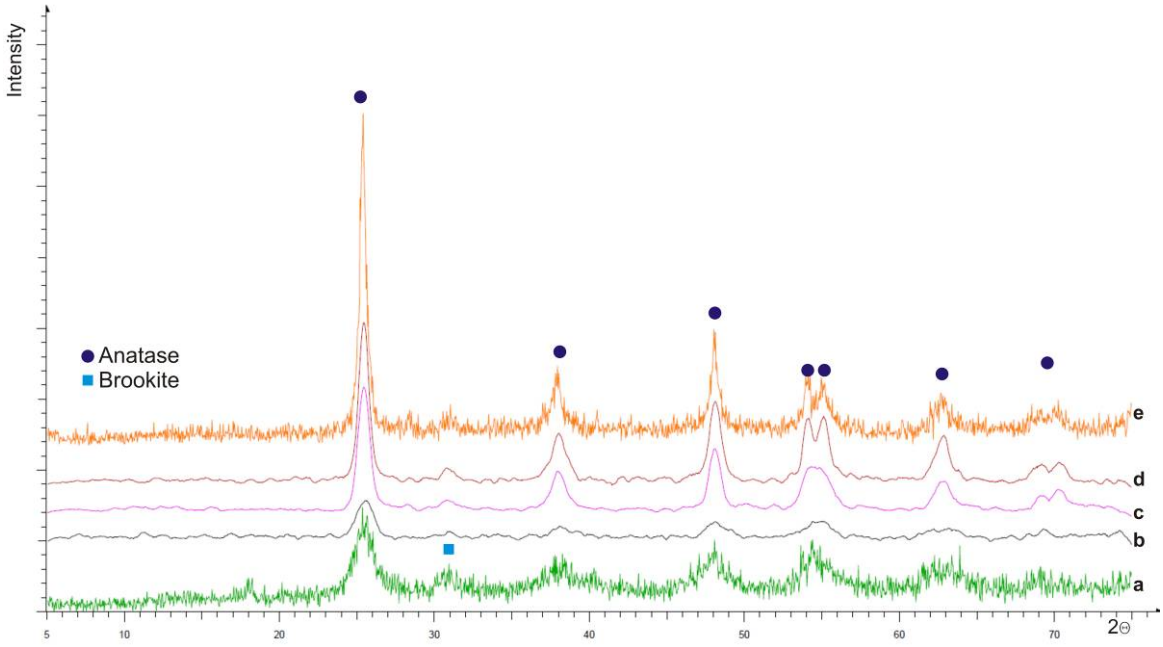

Figure 37: *XRD pattern of TiO_2 prepared with sol-gel and hydrothermal synthesis on 100 and 200 °C for 50 h, 100 h and 150 h*. XRD pattern of material prepared a) with sol-gel and left to age for 9 months in the dark at room temperature, b) with hydrothermal synthesis at 100 °C for 100 h, with hydrothermal synthesis at 200 °C for c) 50 h, d) 100 h and e) 150 h. The circles correspond to anatase and the squares to brookite XRD lines.

From the XRD pattern, Figure 37a, using the Scherrer equation, Equation 1, it was calculated that the average anatase particle size is 6.1 nm (with a Scherrer constant of 0.89, i.e., we approximated the crystals to be spherical). An estimation of the particle size from the TEM micrographs gave the value of 3 ± 1 nm. For determination of the particle size using TEM micrographs we first measured the area of projected surface of the particle, after which the diameter of a circle with the equivalent area was calculated). The difference in the average particle size is due to the XRD that cannot detect very small crystals, while with TEM we can see all, regardless to their size.

Starting powder, Figure 36a, mixed with distilled water, was exposed to hydrothermal conditions for various temperatures and times. Using TEM we followed the evolution of anatase crystals. The samples prepared at 100 and 150 °C for 100 h are shown in Figure 38a and b respectively. Samples prepared at 200 °C for 50 h, 100 h and 150 h are shown in Figure 40a-c, respectively.

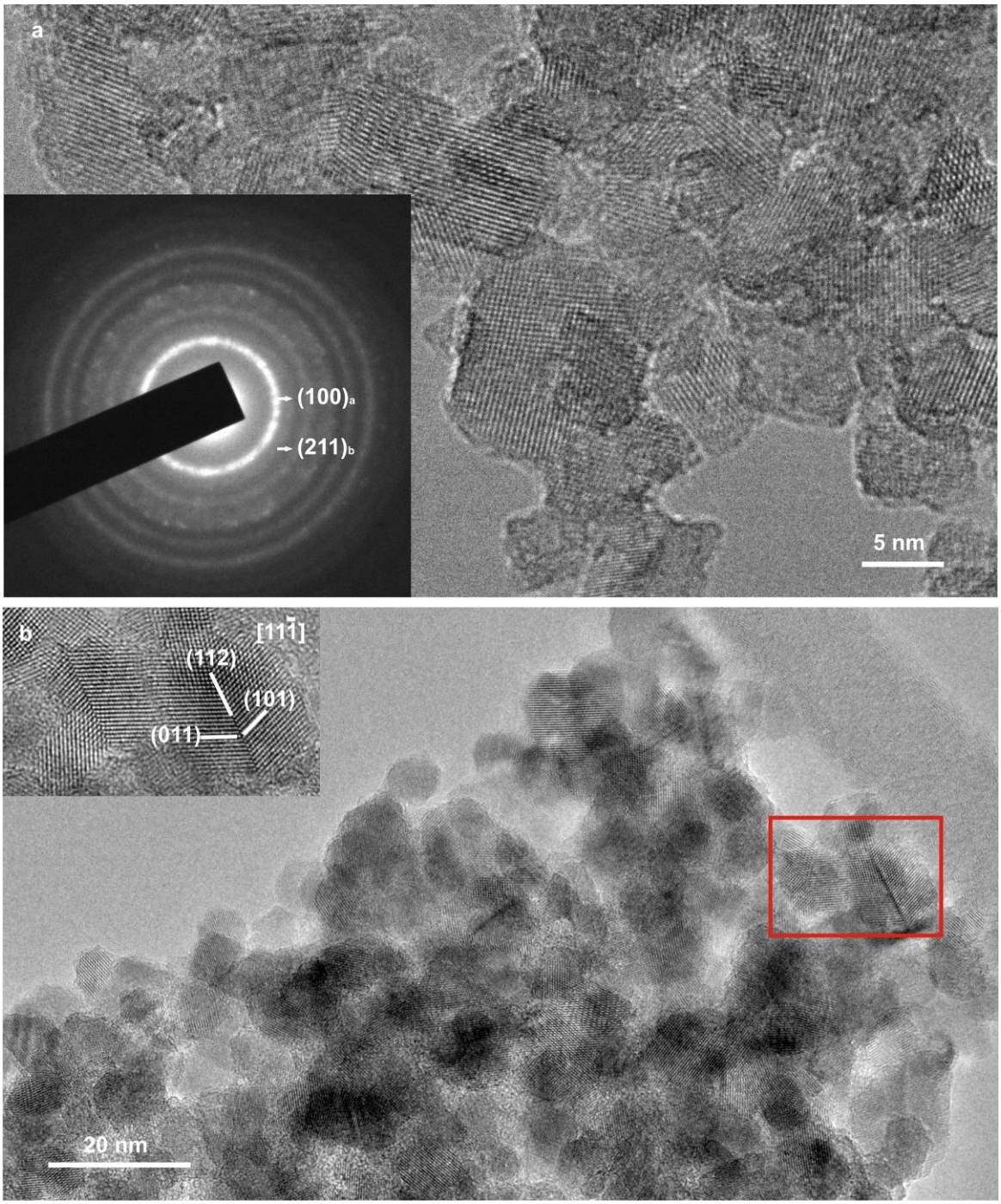

Figure 38: *HRTEM micrograph of hydrothermally treated material for 100 h at 100 °C and 150 °C*. a) HRTEM micrograph of TiO_2 after hydrothermal synthesis at 100 °C for 100 h with SAED (a – anatase planes, b – traces of brookite) on the inset. Particles started to form and to shape into irregular blocky-like crystals. b) HRTEM micrograph of TiO_2 after hydrothermal synthesis at 150 °C for 100 h with magnified twin crystal in [11-1] zone axis on the inset.

In the sample treated at 100 °C for 100 h, the particles nucleated in form of irregular blocky crystal grains (see Figure 38a). They are slightly rounded while their morphology is still not well defined. Diffuse circles on SAED (inset in Figure 38a) indicate that the crystals are relatively small. Weak diffraction rings at certain d-values confirmed the presence of minor crystalline brookite form in the sample.

From the XRD pattern, Figure 37b, it was calculated that the average anatase particle size is 7.1 nm. An estimation of the particle size from the TEM micrographs, gave the

value of 7 ± 2 nm, which is in agreement with XRD result.

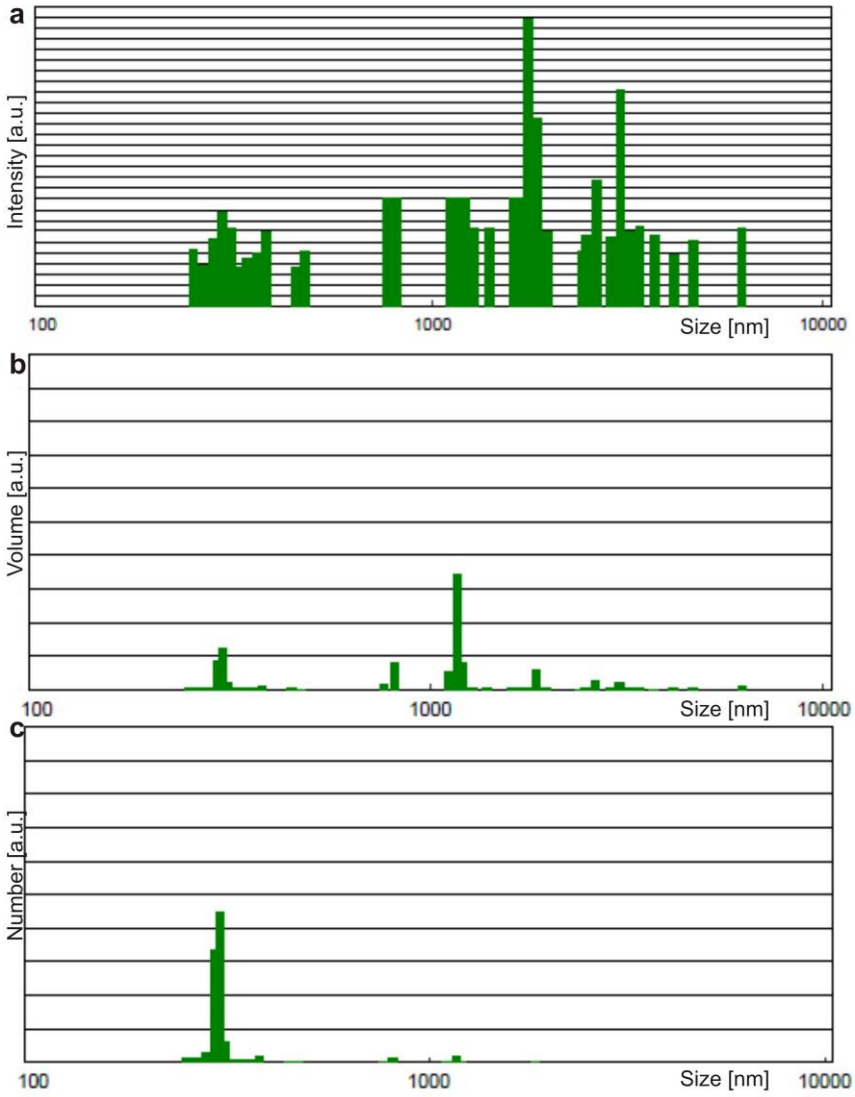

Figure 39: *DLS statistical method for determining the aggregates sizes for sample hydrothermally treated for 100 h at 100 °C*. a) Dependence of intensity of the aggregate' size, b) dependence of volume of the aggregate' size, c) dependence of the number of aggregates of aggregate' size.

With dynamic light scattering (DLC) aggregate sizes were measured with statistical method for the hydrothermally prepared sample at 100 °C for 100 h (see Figure 39) according to the intensity, volume and number of aggregates. Even if crystals are ~7 nm, aggregates measure several 100 nm, which makes them environmentally safer.

After the hydrothermal synthesis at 150 °C for 100 h, Figure 38b, we found few {112} twins within anatase crystals, which show a tendency to become elongated along the twin plane. At the twin boundary we were not able to detect any other element except Ti and O when investigating with TEM/EDXS. As the twin boundaries in anatase are known to possess a local rutile structure, we may anticipate that the twins are formed under conditions close to the anatase-rutile phase transition[123]. The average particle size of this sample calculated from the XRD spectrum is 7.3 nm, the average particle size measured from TEM micrographs is 10 ± 3 nm. The difference between TEM and XRD measurement of particles' size is in the error.

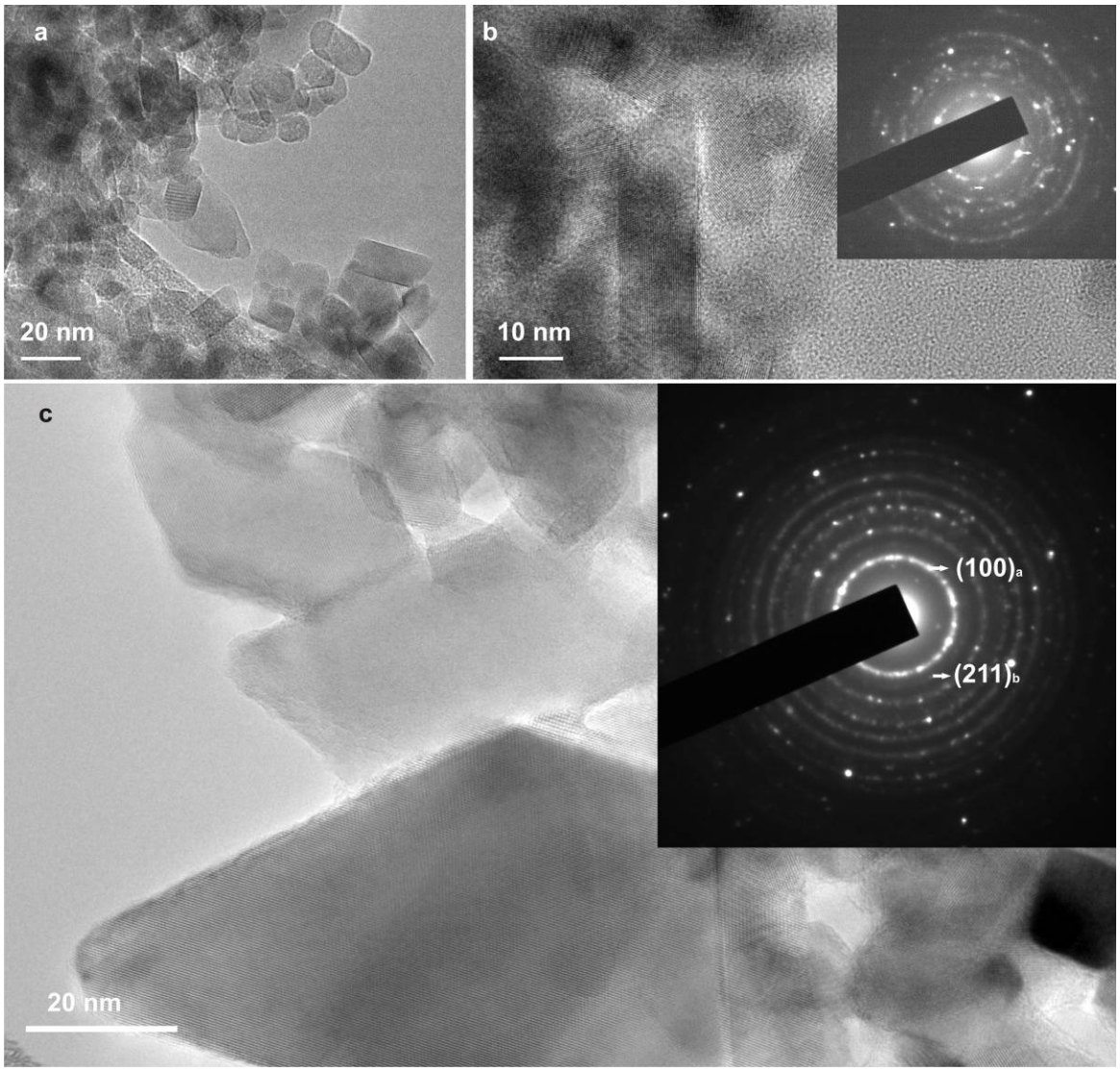

Figure 40: *HRTEM micrographs of hydrothermally treated material for at 200 °C for 50 h, 100 h and 150 h*. HRTEM micrograph of TiO_2 after hydrothermal synthesis at 200 °C for a) 50, b) for 100 h, c) 150 h. With increased time, an increase in numbers of pointed bipyramidal anatase crystals appeared. On the inset are SAED of TiO_2 anatase and still present feeble brookite reflections (a – anatase planes, b – traces of brookite).

The hydrothermal synthesis at 200 °C for 50 h resulted in better defined crystals, which showed irregular blocky and somewhat rod-like morphology, as can be seen in Figure 40a.

By analysing the XRD patterns, Figure 37c, the crystal size was found to be on average 11.9 nm, while based on TEM measurements, the average particle size was 15 ± 5 nm. The discrepancy in the mean particle size may be due to their rod-like habit.

Extending the duration of HT synthesis at 200 °C to 100 h produced even more defined crystal morphology while their longitudinal nature was even more pronounced in comparison to the initial blocky crystals (see Figure 40b). From the XRD pattern, Figure 37d, and the Scherrer equation the crystals are on average 14.4 nm in size, while the TEM gave us a particle size of 17 ± 5 nm. When the time of HT synthesis was prolonged by an additional 50 h, to 150 h in total, the crystals' final shape according to our TEM observations becomes bipyramidal (with irregular blocky and rod-like crystals still present), see Figure 40c. The crystal surfaces are well defined. From the XRD pattern, Figure 37e, and the Scherrer equation the crystals are on average 17.8 nm in size, while

the TEM measurements gave 20 ± 13 nm. All differences between TEM and XRD measurement of particles' size are in the error.

All the calculated (from XRD with the Scherrer equation) and measured (from TEM micrographs) particle sizes are summarised in Table 14. We can see that with an increasing temperature and synthesis time the particles grew.

Average particle sizes obtained by XRD and TEM analysis do not deviate much where particles were small with just irregular blocky shape i.e. spherical in first approximation. With the start of the crystal shape transformation from irregular blocky into elongated or bipyramidal, the difference between TEM and XRD average particle size analysis becomes noticeable due to the increased deviation of morphology from the isotropic (spherical) shape. The reason for that is the method used for particle size determination from TEM images.

Table 14: *Average particle sizes of TiO_2 crystals*. Average particle sizes in the samples prepared from the initial suspension that was HT treated at various temperatures and times, and average particle sizes in 4 samples prepared with cyclic (Table 13) HT synthesis starting from the initial suspension. Average particle sizes were calculated from the Scherrer equation and measured from the TEM micrographs. TEM measurements error is defined as standard deviation, whereas the error made using Scherrer equation is estimated to ~ 20 %.

Sample prepared from initial suspension with sol-gel synthesis and left to age				
T [°C]	t [h]	$<d_{Scherrer}> \pm \Delta_S$ [nm]	$<d_{TEM}> \pm \Delta$ [nm]	Dominant shape of crystals
~20	9 months	6.1 ± 1.2	3 ± 1	irregular areas in amorphous matrix
Samples prepared with hydrothermal synthesis from initial suspensions				
T [°C]	t [h]	$<d_{Scherrer}> \pm \Delta_S$ [nm]	$<d_{TEM}> \pm \Delta$ [nm]	Dominant shape of crystals
100	100	7.1 ± 1.4	7 ± 2	irregular blocky
150	100	7.3 ± 1.4	10 ± 3	irregular blocky
200	50	11.9 ± 2.4	15 ± 5	irregular blocky, rod-like
200	100	14.4 ± 2.8	17 ± 5	rod-like
200	150	17.8 ± 3.6	20 ± 13	bipyramidal
Samples prepared with cyclic hydrothermal synthesis, 100 h at each temperature				
T [°C]		$<d_{Scherrer}> \pm \Delta_S$ [nm]	$<d_{TEM}> \pm \Delta$ [nm]	Dominant shape of crystals
40		12.2 ± 2.4	17 ± 5	irregular blocky, rod-like
50		12.4 ± 2.4	19 ± 7	irregular blocky, rod-like
80		12.6 ± 2.6	14 ± 5	rod-like
200		12.8 ± 2.6	20 ± 6	rod-like

During the cyclic experiment, we started with a sol-gel derived material, HT treated at 40 °C for 100 hours. After cooling, we took a sample for TEM studies, and returned the rest of the material for the next HT cycle at higher temperature. We repeated this procedure up to 100 °C in 10 °C steps. Two final experiments were done at 150 °C and 200 °C. In all runs the HT treatment time was 100 hours. At as low as 40 °C well defined blocky anatase crystals were produced (Figure 41). Some of the crystals were already rod-like at 40 °C.

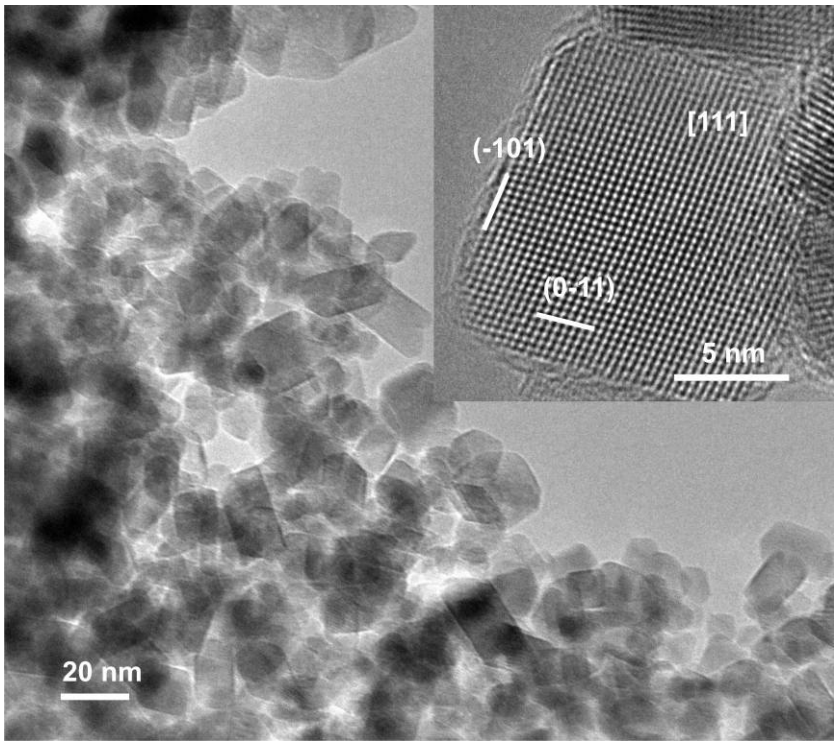

Figure 41: *TEM micrograph of TiO_2 prepared with HT synthesis at 40 °C for 100 h*. TEM micrograph of the sample prepared via HT synthesis at 40 °C for 100 hours. On the inset is HRTEM image of irregular blocky-like crystal in [111] zone axis.

When continuing the cyclic experiment, step by step, with the increment of 10 °C, at 80 °C (Figure 42) there were mostly rod-like crystals, but some irregularly developed blocky crystals remained.

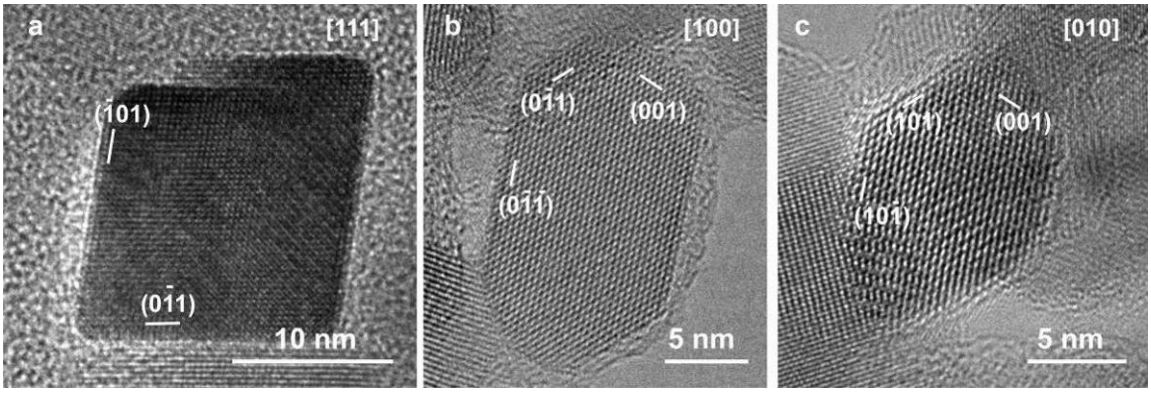

Figure 42: *HRTEM micrograph of TiO_2 prepared with HT (cyclic) synthesis at 80 °C for 100 h*. HRTEM images of rod-like crystal in three different zone axis a) [111], b) [100] and c) [010] grown during hydrothermal synthesis at 80 °C.

In Table 14, the measured crystal sizes for samples, which were hydrothermally prepared with cyclic heating are presented. It is obvious that the crystals were not growing with increasing temperature; they just reshaped.

According to the XRD analysis (Figure 43) and the electron-diffraction patterns we always found some brookite in addition to anatase. Comparing the measured intensities with the theoretical intensities of the peaks we concluded that there are just traces of brookite. Even in the starting suspension that was allowed to age for several months, a small amount of brookite was found in addition to the anatase.

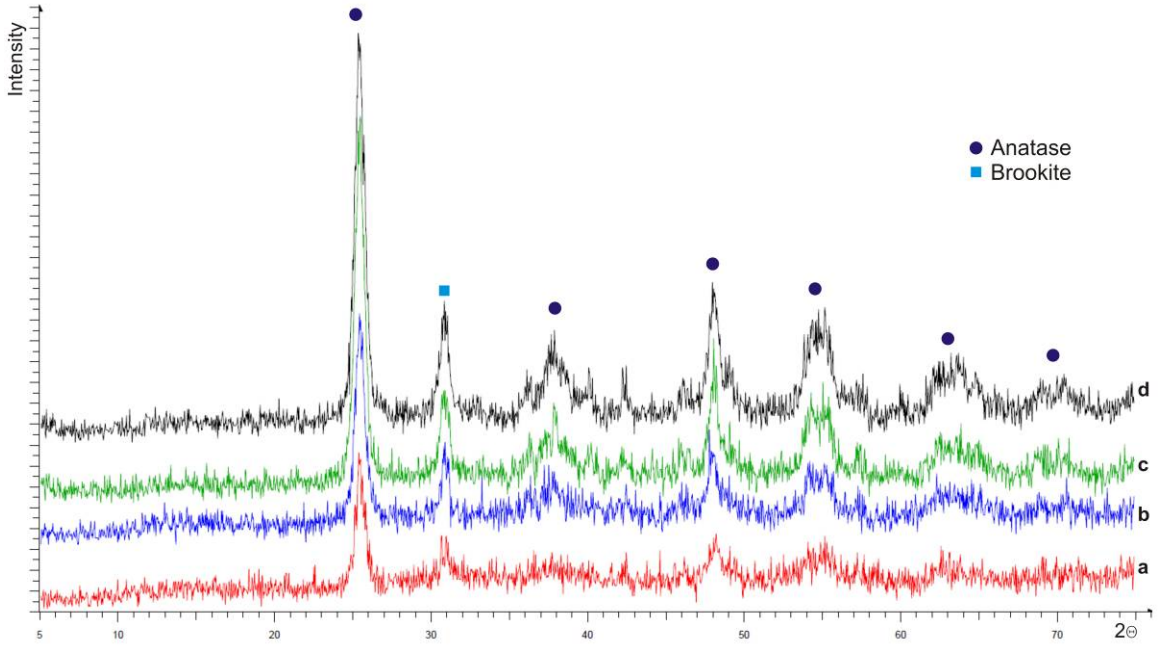

Figure 43: *XRD pattern of TiO_2 prepared with cyclic HT synthesis (Table 13)*. XRD spectra of TiO_2 prepared with the cyclic HT synthesis (a) at 40 °C, (b) at 50 °C, (c) at 80 °C and (d) at 200 °C. In all runs the heating time was 100 hours. The circles correspond to anatase and the squares to brookite XRD lines.

Sample HT treated at 200 ºC for 150 h (see Figure 40) was heated in TEM to find the temperature of transformation from anatase, brookite into rutile. We followed the transformation with observing the electron diffraction pattern (SAED). At 600 ºC, there were still both metastable TiO_2 crystal forms present (anatase and brookite). At 800 ºC, there was just anatase left, at 850 ºC, rutile appeared, but anatase was still present, at 900 ºC, there was just rutile. The transformation we followed was done in vacuum, which represents specific conditions where the reduction of Ti ions, from Ti^{4+} to Ti^{3+}, is possible. However, also in the literature we can find that anatase prepared with HT synthesis is more stable and has higher transformation temperature (above 800 ºC)[124] in comparison to anatase prepared at normal conditions without additives conversion from anatase to rutile ends at 600 to 700 ºC[125].

4.2 Self-assembly and formation of hierarchical structures

Self-assembled micro samples were investigated with SEM, FEG-SEM and TEM to define the morphology, shape and crystallinity, which was investigated also with XRD.

Solvothermally prepared samples in glycerol at 180 ºC for 24 h were amorphous (see Figure 44a) flower-like structures (see Figure 45) which were deposited inside spherical to oblate shapes geodes (see Figure 45c). Results later on showed that amorphous flower-like structures (see Figure 44a) showed no photocatalytic activity, but as micro structures can be easily removed from suspensions by filtration or just with letting everything to sediment. In this way they represented the good starting point for creation of photocatalytic material.

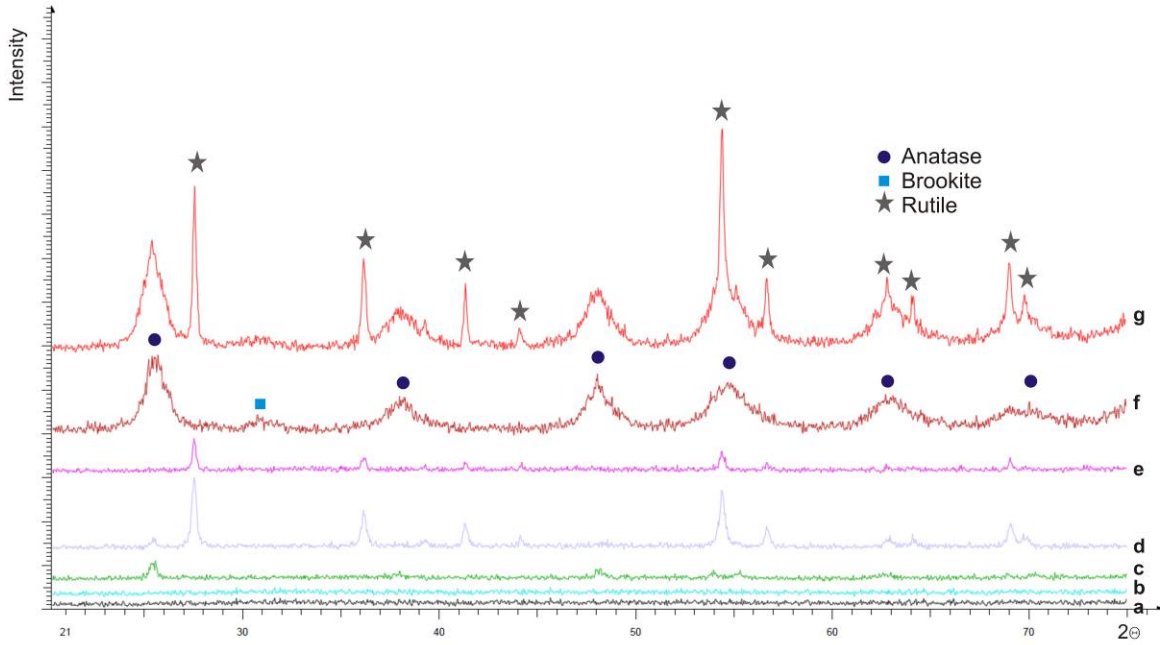

Figure 44: *XRD pattern of TiO_2 materials*. XRD spectra of a) in glycerol solvothermally prepared amorphous material at 180 ºC for 24 h, which was calcined at b) 300 ºC, c) 350 ºC d) 550 ºC and on e) 600 ºC. Calcined material was hydrothermally treated in the second step at 120 ºC for 12 h f) using material calcined at 300 ºC , g) material calcined at 550 ºC .

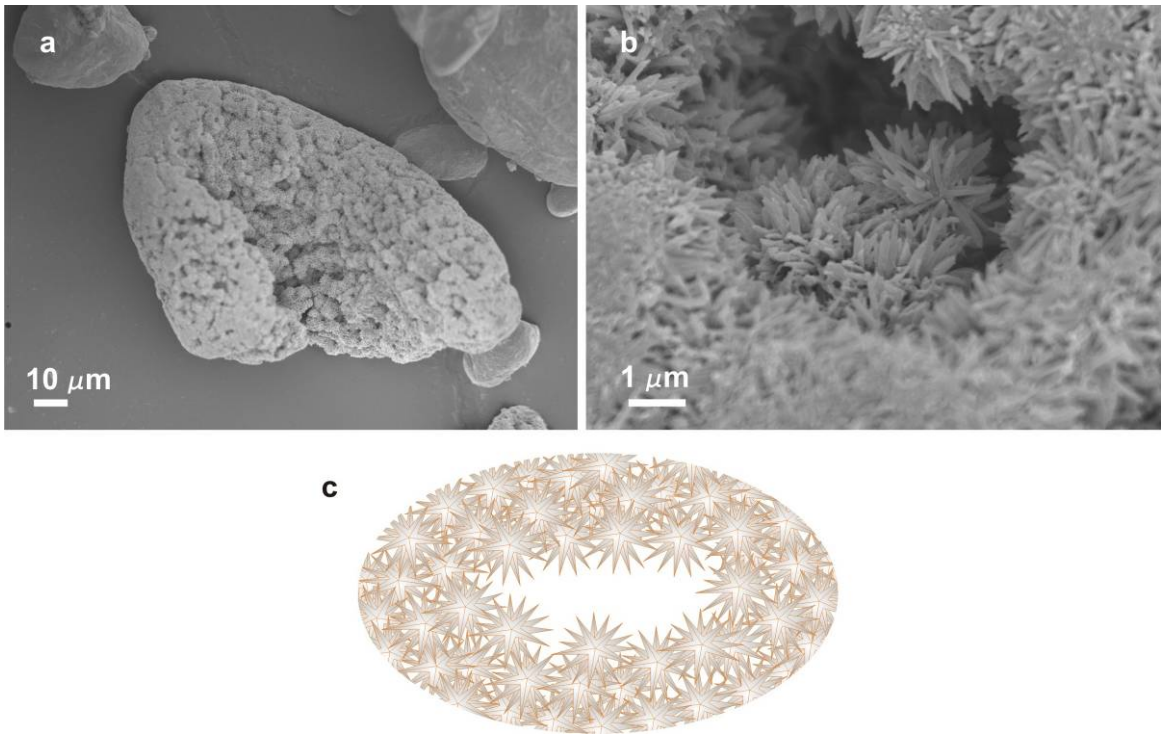

Figure 45: *FEG-SEM micrographs of material prepared with ST synthesis at 180 °C for 24 h*. a, b) FEG-SEM micrograph of solvothermally prepared material in glycerol at 180 ºC and 24 h. Flower-like structures were found inside geode-like structures. c) Schematically represented geodes, which were partially removed when cleaning the sample with ethanol and water with stirring, centrifuging at 5000 rpm for 5 min and removing of supernatant.

To find out which compound is building the amorphous flower-like particles we performed FTIR analysis of as-prepared and thermally treated samples. For comparison

FTIR spectra of pure glycerol and anatase nanoparticles were recorded. It was found that in this structure there were still some organic compound present (Figure 46c), which have to be removed prior to use the material as catalyst. We removed organic compound with calcination in air at different temperatures. After calcination at 300 °C the organic compounds were completely removed (see Figure 46d). In Figure 46c bands around 1000 cm^{-1} and 3000 cm^{-1} to 3500 cm^{-1} correspond to bands in glycerol in Figure 46b. These bands are not present in the Figure 46d (powder calcined at 300 ºC for 48 h), where we can find new bands around 2000 cm^{-1} which can also be seen on the Figure 46a (anatase). This band already exists in solvothermally prepared sample before it was calcined (see Figure 46c).

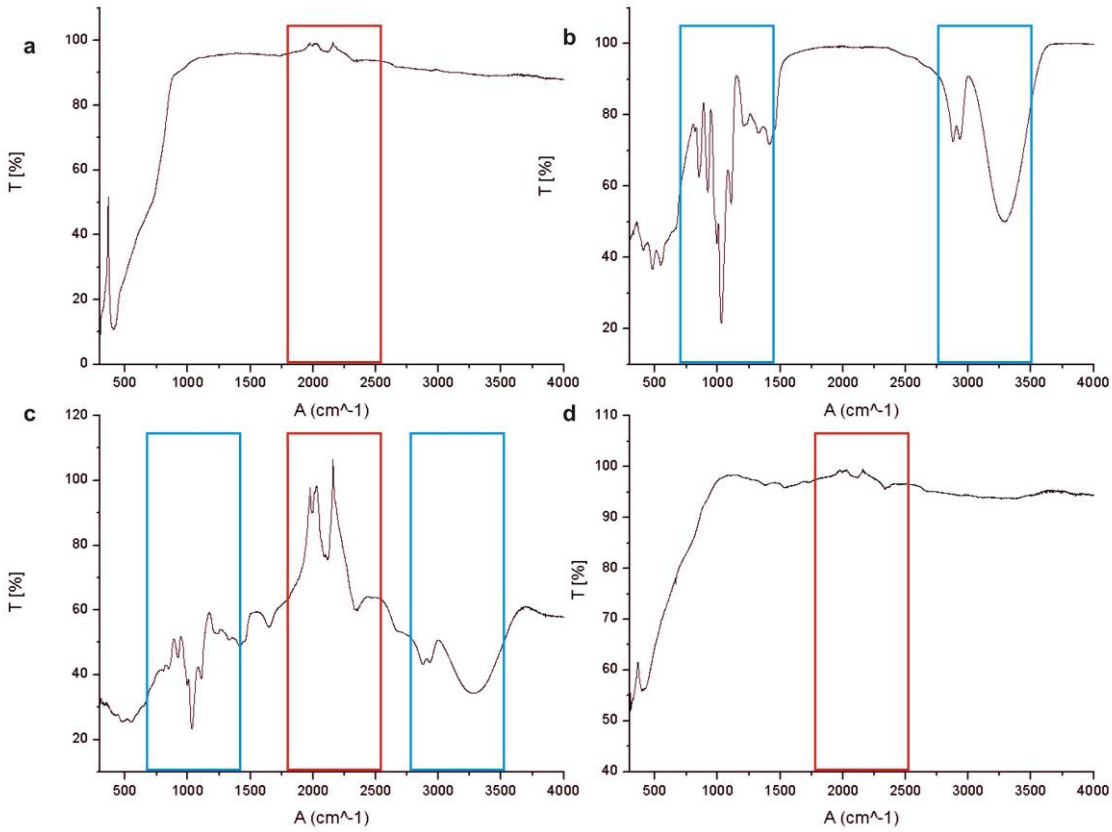

Figure 46: *FTIR spectra*. FTIR spectra recorded in attenuated total reflectance (ATR) mode of a) anatase, b) glycerol, c) sample prepared solvothermally in glycerol at 180 ºC for 24 h, d) which was calcined at 300 ºC for 48 h.

According to the literature [126] the solvothermally prepared amorphous flower-like structures at 180 ºC for 24 h were titanium oxyhydrate (see Figure 47a). With ST synthesis at 200 ºC for 24 h (see Figure 47b) material was crystalline. The peaks most probably correspond to titanium-glycerolate, which is not listed in any structure database. Some of the peaks can be listed as zinc, iron, manganese and cobalt glycerolate, other do not belong to any know structure. Therefore we presume that we prepared titanium glycerolate.

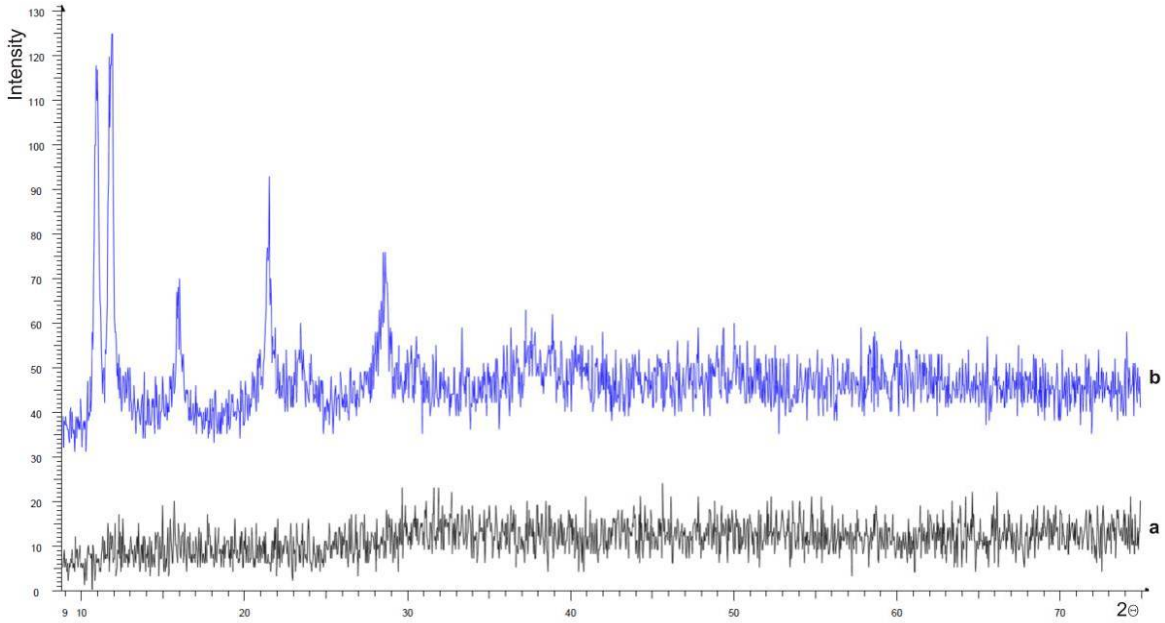

Figure 47: *XRD pattern of Ti-glycerolate materials*. XRD patterns of in glycerol solvothermally prepared a) amorphous material at 180 ºC for 24 h, and b) crystalline material prepared at 200 ºC for 24 h.

Calcination of flower-like forms at 300 ºC left structures intact (Figure 48a) and in amorphous phase (see diffraction pattern on the inset of the Figure 48a and XRD pattern in Figure 44b), while at 350 ºC conversion from amorphous to anatase phase started (see Figure 44c). At 550 ºC we observed conversion from anatase to rutile, where still both crystal modifications were present in the sample (see Figure 44d). Calcination at 600 ºC on the other hand results just in rutile phase (see Figure 44e).

Flower-like structures were consisted of rolled/twisted thin amorphous sheets (see Figure 48b) until structures started to crystallise (see Figure 49a, b) at 350 ºC.

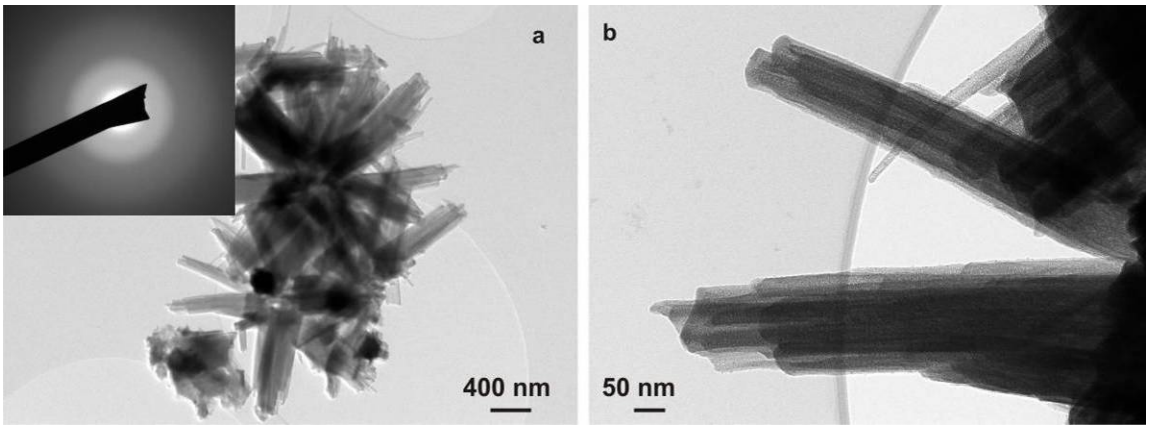

Figure 48: *TEM micrographs of flower-like amorphous structures prepared with ST synthesis at 180 °C for 24 h*. Sample prepared solvothermally in glycerol at 180 ºC for 24 h, cleaned and dried at 60 ºC for 24 h and calcined at 300 ºC for 48. a) Flower-like structure with SAED of amorphous nanosheets on the inset, b) HRTEM detail of one nanofeature consisted of rolled/twisted amorphous thin sheets.

At 350 ºC (see Figure 49a, b) there were some single-leafs, but even higher calcination temperature did not extensively damage flower-like structure (see SEM micrograph of material calcined on 550 ºC in Figure 49c and on 600 ºC with additional hydrothermal

synthesis in Figure 51b).

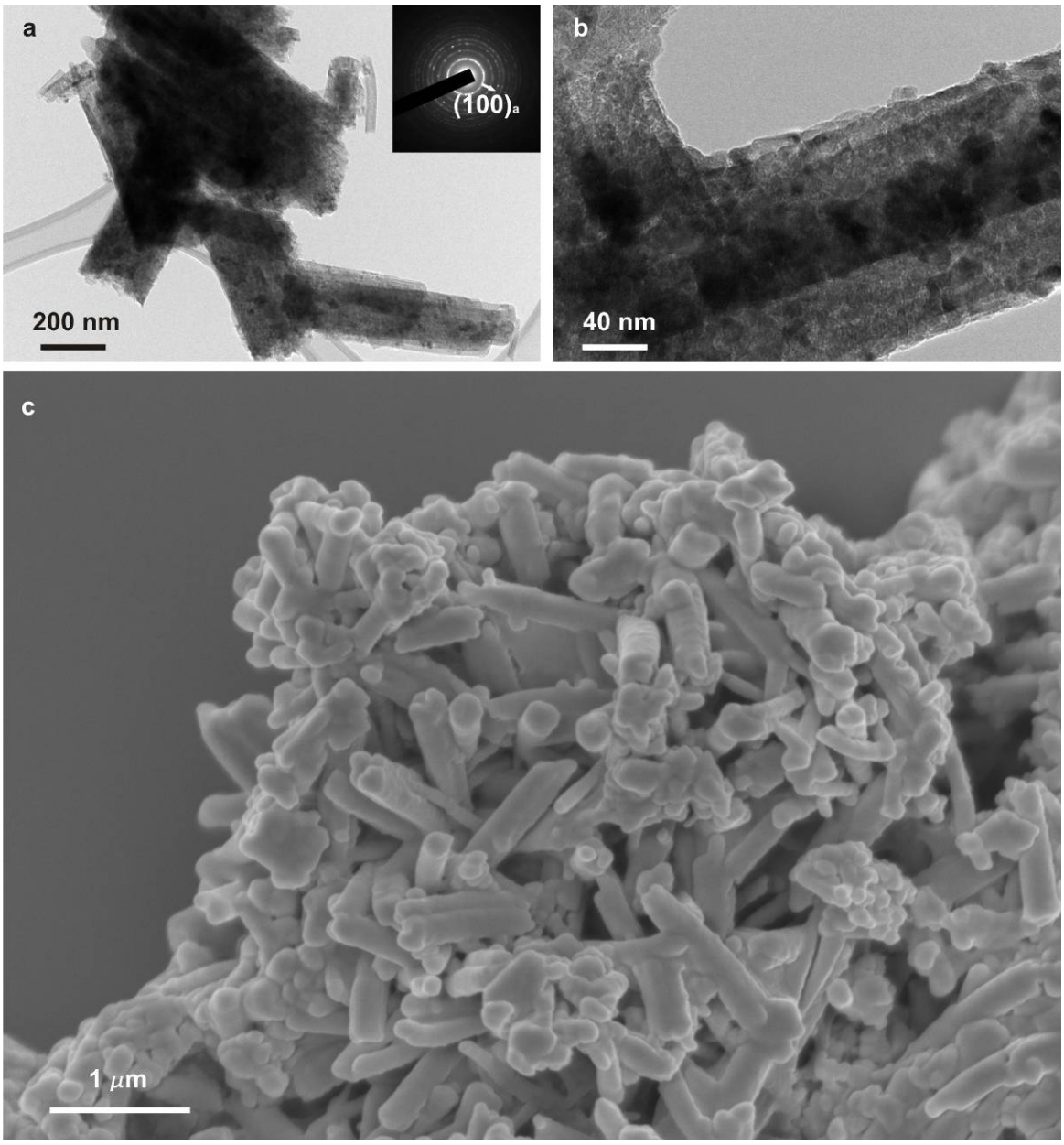

Figure 49: *TEM and SEM micrographs of TiO_2 prepared with calcination after ST synthesis*. Sample prepared solvothermally in glycerol at 180 ºC for 24 h, cleaned and dried at 60 ºC for 24 h, a, b) calcined at 350 ºC for 48 h, c) at 550 ºC for 48 h and observed under a, b) TEM, c) FEGSEM. a, b) Some flower-like structures were reshaped (damaged) already at 350 ºC, anatase crystals started to form, as seen on the diffraction pattern on the inset. c) However, at 550 ºC a lot of flower-like structures still remained intact.

The average diameter of the flower-like structures before calcination was according to SEM and TEM micrographs 1.8 μm, the average leaf length was 0.9 μm and the average leaf width was 150 nm. After calcination regardless to the temperature the average diameter of the flower-like structures was 2.8 μm, the average leaf length was 1.4 μm and the average leaf width was 300 nm.

To improve the photocatalytic properties, which is shown later on, of the sample we tried to use the flower-like structures as a substrate where nanoparticles of anatase would grow. With this aim we performed another hydrothermal synthesis at 120 ºC for 12 h, but this time in distilled water with the addition of 0.5 ml of titanium isopropoxide (TO) and

the calcined flower-like structures. Expected formation of anatase and traces of brookite took place (see Figure 44f, g) at intrinsic pH at around 5[97].

Flower-like substrate that was calcined at 300 ºC, was covered with anatase crystals (see Figure 50a and Figure 44f). The average size of the crystals was according to TEM micrographs 10 nm in diameter, the average diameter of the flower-like structure was 2.9 μm, leaf length 1.5 μm and leaf width 350 nm. From the diffraction patterns, shown on the inset of the Figure 50c, we presume that the whole flower structure crystallised and that anatase crystals on its surface are not just attached but are grown from the amorphous flower-like substrate.

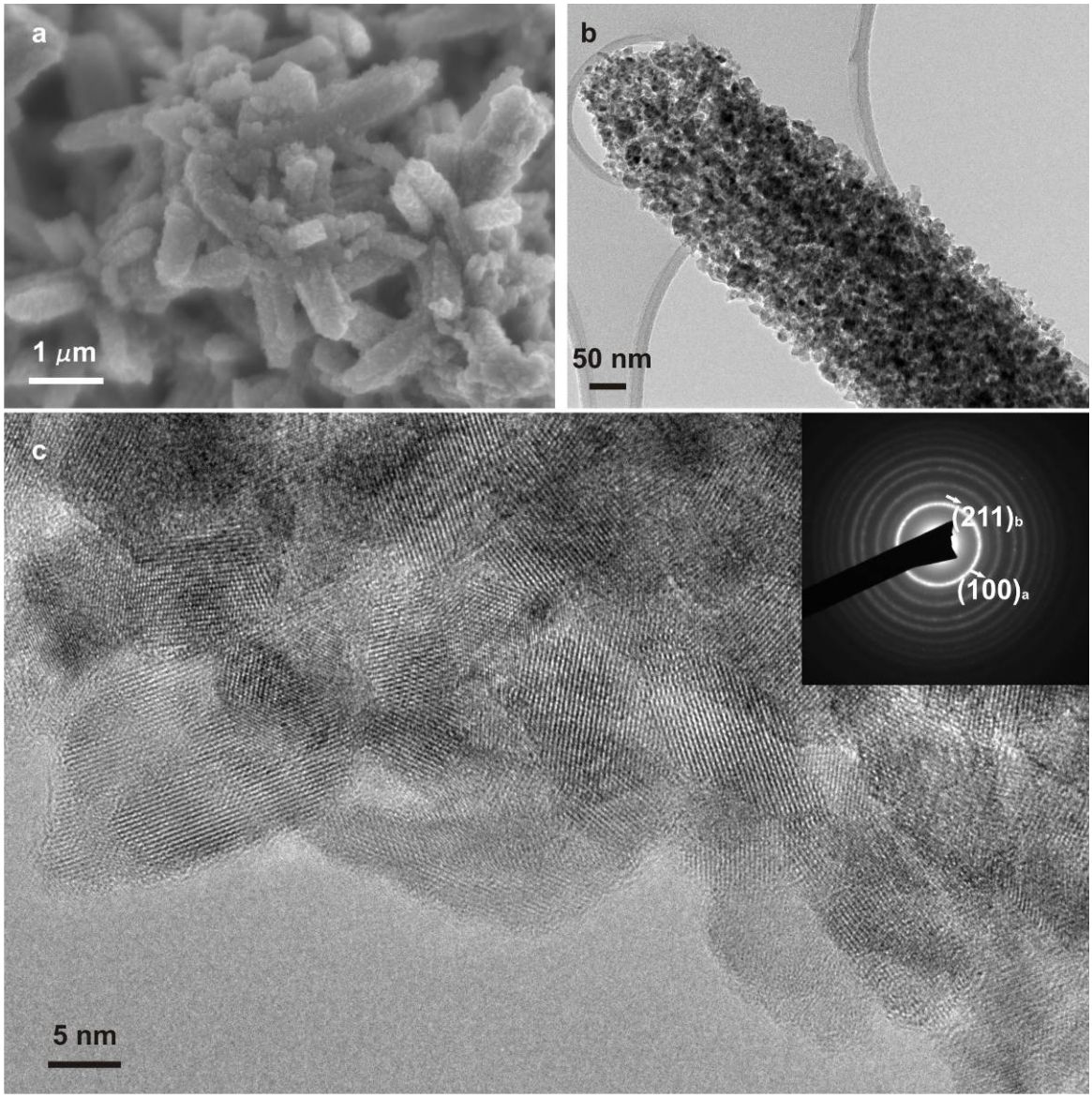

Figure 50: *FEG-SEM and TEM micrographs of TiO_2 prepared with HT synthesis using solvothermally prepared and afterwards calcined material*. a) FEG-SEM micrographs, b) TEM and c) HRTEM micrographs of sample prepared from 0.1 g of flower-like particles, calcined at 300 ºC with additional hydrothermal synthesis at 120 ºC for 12 h with addition of 0.5 ml TO. On the inset is SAED of TiO_2 anatase and feeble brookite reflections (a – anatase planes, b – traces of brookite).

Flower-like substrate, that was calcined at 550 ºC, was not covered with any crystals (see Figure 51) and did not change any outer dimensions. The average size of the crystals building flowers was according to TEM micrographs 60 nm in diameter, the size of the

anatase crystals, which were not even attached to flower-like structure's surface, was 10 nm in diameter. From the diffraction patterns on the inset of the Figure 51b we can confirm that building blocks of the flowers are big rutile crystals, while anatase product on the inset of the Figure 51c is nano.

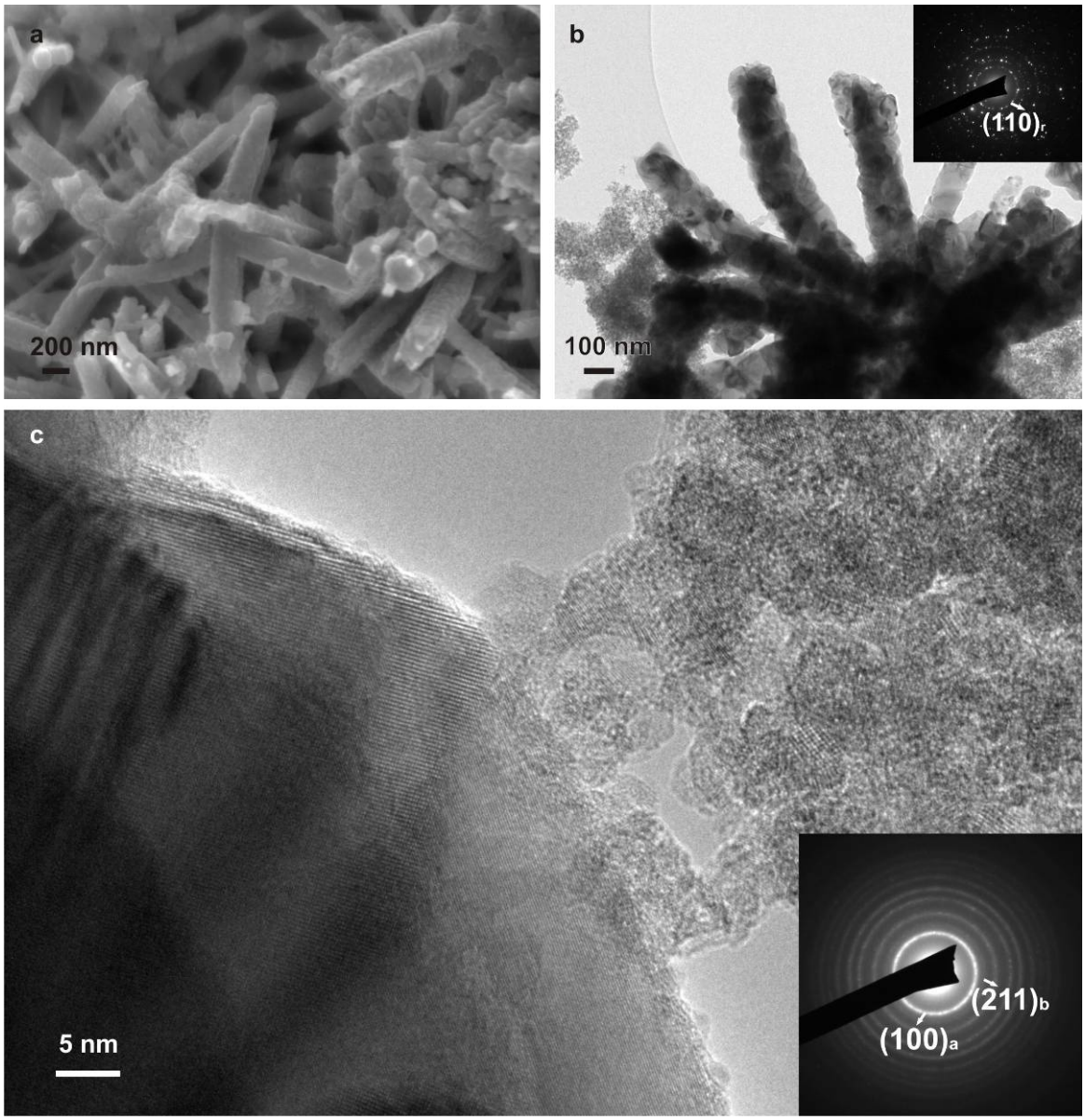

Figure 51: *FEG-SEM and TEM micrographs of TiO_2 prepared with HT synthesis using solvothermally prepared and afterwards calcined material*. a) FEG-SEM micrographs and b, c) TEM micrographs of sample, prepared from 0.1 g of precalcined flower-like powder at 550 ºC with additional hydrothermal synthesis at 120 ºC for 12 h with the addition of 0.5 ml Ti (IV) isopropoxide. Electron diffraction pattern on b) belongs to rutile flower-like structures, on c) to anatase nanopowder.

All measured (from TEM micrographs) particle sizes of flower-like structures are presented in Table 15. This time the calculation of the sizes using Scherrer equation was not possible because structures were much bigger than 100 nm, which is the limit of the reasonable calculations of the average particle sizes in the specific crystal directions.

Structures grew with calcination, regardless to calcination temperature (compare second and third column in the Table 15, where in the third column are results for all temperatures after calcination). HT treatment of amorphous sample, calcined at 300 ºC,

lead to increase of the sizes of the flower-like structures, while when using non-amorphous calcined material, new material did not even attach onto flower-like structures.

Table 15: *Average particle sizes of flower-like structures*. Average particle sizes in the samples prepared with ST synthesis, before and after calcination, and after additional HT treatment. D is diameter of flower-like structure, L is length of flower-like structure's leaf, W is width of flower-like structure's leaf. Average particle sizes were measured from the TEM/SEM micrographs. Measurement error is defined as standard deviation.

Dimension	before calcination	after calcination	after HT treatment	
	amorphous	all T	300 °C	550 °C
<D> [μm]	1.8 ± 0.05	2.8 ± 0.05	2.9 ± 0.05	2.8 ± 0.05
<L> [μm]	0.9 ± 0.1	1.4 ± 0.1	1.5 ± 0.1	1.4 ± 0.1
<W> [nm]	150 ± 10	300 ± 10	350 ± 10	300 ± 10
<W> [nm]	150 ± 10	300 ± 10	350 ± 10	300 ± 10

Table 16: *Average particle sizes of flower-like structures*. Average particle sizes in the samples prepared with ST synthesis, before and after calcination, and after additional HT treatment. d_1 is diameter of the crystallites building up the flower-like structure, d_2 is diameter of crystals on the surface of the flower-like structures, d_3 is the diameter of the crystals in the surrounding of the flower-like structure, a stands for anatase, r for rutile and b for brookite crystals. Average particle sizes were measured from the TEM/SEM micrographs. Measurement error is defined as standard deviation.

Dimension	after calcination		after HT treatment	
	300 °C	550 °C	300 °C	550 °C
<d_1> [nm]	amorphous	60 (r)	/[1]	60 ± 5 (r)
<d_2> [nm]			10 ± 1.5 (a, b)	/
<d_3> [nm]			10 ± 1.5 (a, b)	10 ± 1.5 (a,b)

After hydrothermal synthesis with precalcined flower-like particles and TO addition (at various temperatures), beside recrystallised starting flower-like particles a porous material with parallel pores was found as the side product (see Figure 52). In the case of hydrothermal synthesis using TO, without the addition of precalcined powders, no such porous material was found.[97]

[1] Measurement of the diameter of the crystallites building up the flower-like structure calcined at 300 °C and afterwards hydrothermally treated, could not be measured, because the material was fully covered by hydrothermally prepared anatase.

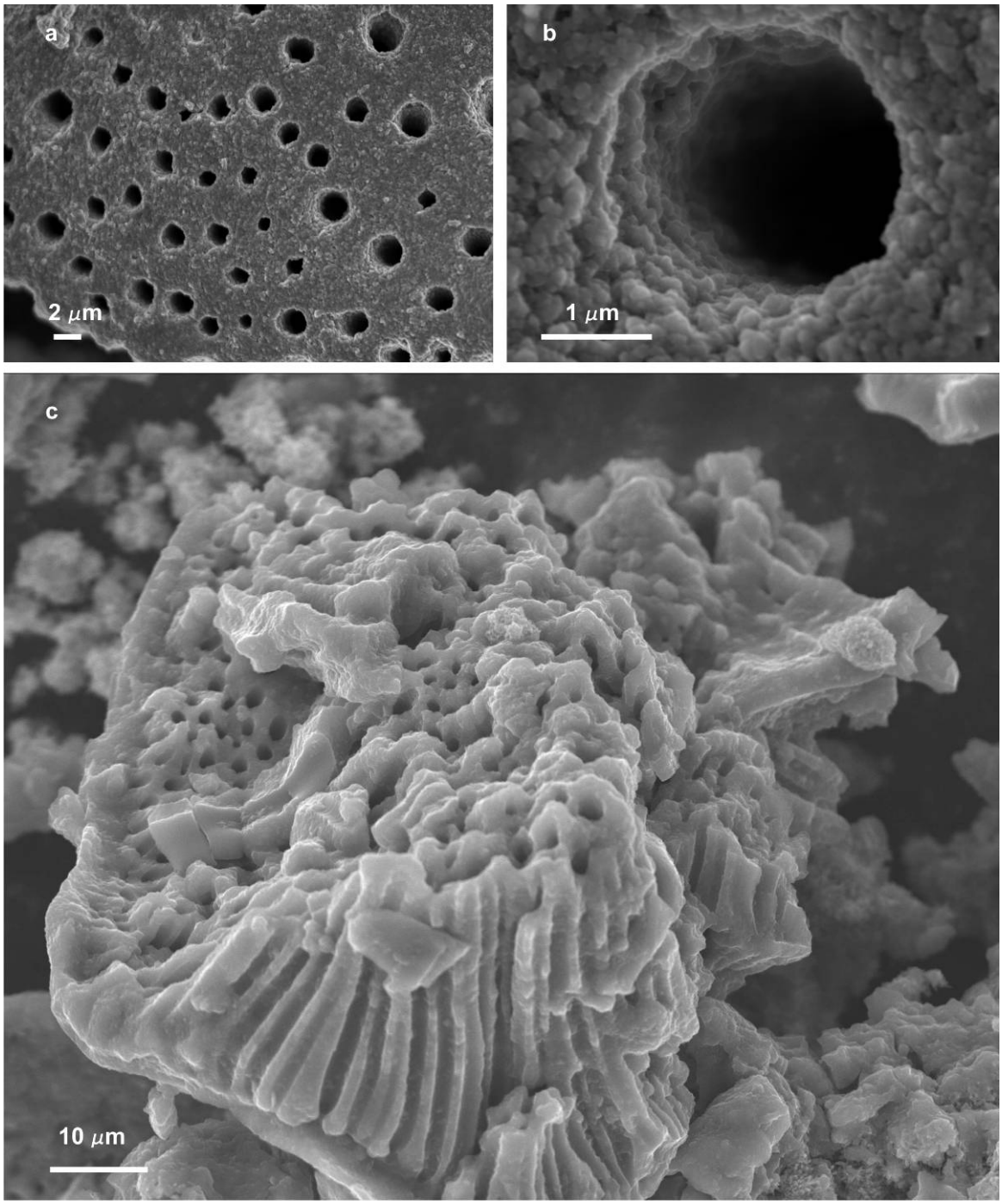

Figure 52: *FEG-SEM micrographs of TiO_2 porous material*. a, b) FEG-SEM and c) SEM micrographs of samples, prepared from 0.1 g of precalcined flower-like particles at a, b) 300 ºC and c) 550 ºC with additional hydrothermal synthesis at 120 ºC for 12 h with the addition of 0.5 ml TO.

Porous material had micron-sized pores (ranging from 0.5 μm to 3.5 μm in diameter, i.e. in the range of the flower-like structures, 5 μm to 60 μm in the length) and was built from 100 nm sized anatase aggregates (estimated from SEM micrographs), which were made from 10 nm anatase crystals (estimated from XRD and TEM micrographs).

All measured (from SEM, TEM micrographs) sizes of flower-like structures are presented in Table 17. From Scherrer equation (from XRD measurements) we could estimate just the size of the crystals building up the pores structures. Because the porous material was never synthesised alone (there were always flower-like structures present),

this was not possible.

With DLS we could estimate the aggregates building up the porous structure, but the porous structure was hard to break apart, i.e. we could measure all the sizes of the porous material just with TEM/SEM micrographs.

Table 17: *Average sizes of the porous material*. Average sizes in the samples prepared with ST synthesis, calcined, and hydrothermally treated. TEM/SEM micrographs were used for estimations of the range of pores' diameter, D_p, and pores' length, L_p. For estimation of the aggregates size building up the structure, d_a, and crystal size building up the aggregate, d_b, we used TEM micrographs. Measurements error is defined as standard deviation.

Dimension	after HT treatment
D_p [μm]	0.5 – 3.5
L_p [μm]	5 – 60
$<d_a>$ [nm]	100 ± 15
$<d_b>$ [nm]	10 ± 1.5

4.3 Photocatalysis

4.3.1 Anatase nanoparticles

Photocatalytic effect represents the most important property of synthesized TiO_2. For quick determination of catalysts activity we used blue resazurin (Rz), which decolorizes into pink resorufin (Rf), i.e. the change happens in visible part of the spectrum.

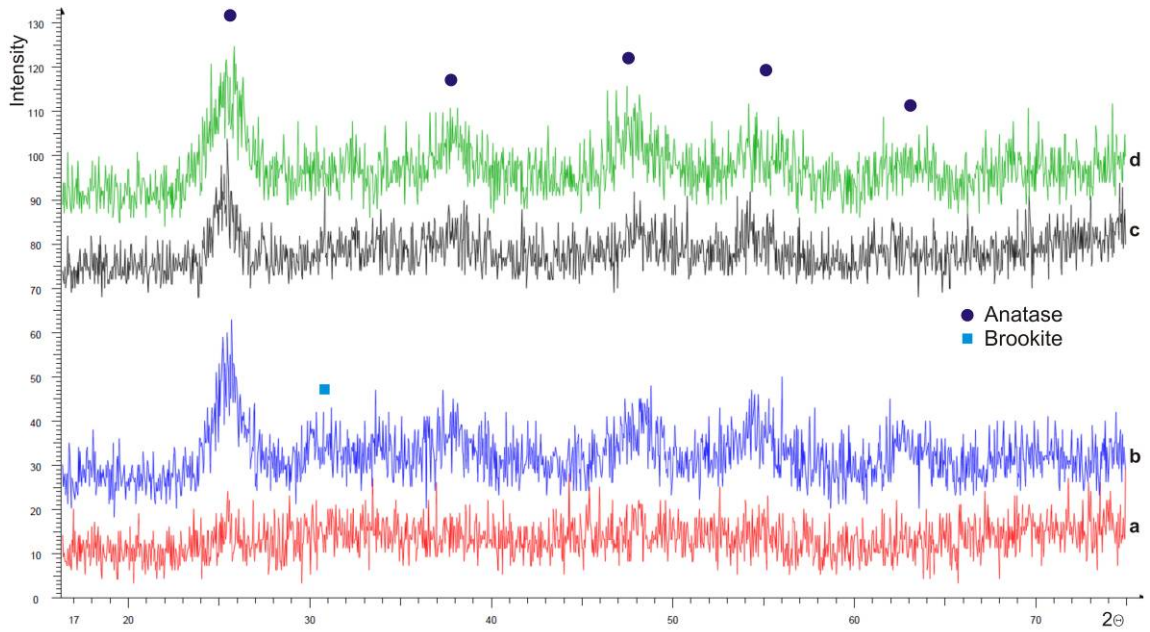

Figure 53: *XRD pattern of TiO_2 prepared with SG and HT synthesis*. XRD pattern of TiO_2 prepared with sol-gel synthesis in a) distilled water and c) ethanol. Powder samples were hydrothermally treated at 150 °C for 48 h using powder prepared with SG in b) distilled water and aged, and prepared in d) ethanol.

To compare the photocatalytic efficiency of nano structures prepared with different techniques and solutes, we prepared samples with sol-gel technique from TO in distilled

water and ethanol with standard procedure, washed the samples with distilled water till constant pH and electrical conductivity, and dried material in air at room temperature. It started to crystallise in anatase form when prepared in ethanol (see Figure 53c), while material prepared in distilled water was always amorphous (for photocatalytic test we used aged sample from Figure 36b, which started to crystallise in anatase form). Sol-gel prepared material was afterwards hydrothermally treated at 150 ºC for 48 h. After hydrothermal synthesis material was nanocrystalline anatase, with small amount of brookite (see Figure 53b and c).

From XRD using Scherrer equation we calculated average particle sizes for crystals prepared with ST and HT synthesis. Results are presented on Table 18. With HT synthesis crystals formed and grew from SG prepared material. If material was left to age, crystals formed and grew spontaneously. From amorphous material prepared in distilled water average particle size after HT synthesis was 4.0 nm, while when starting from TiO_2 prepared in ethanol, crystals grew from 3.2 nm to 4.7 nm.

Table 18: *Average particle sizes and photocatalytic effect of TiO_2 crystals*. Material prepared with sol-gel in ethanol and distilled water, were additionally hydrothermally treated. Error made using Scherrer equation is estimated to ~ 20 %. Decomposition of organic compound (photocatalysis) was tested with blue colour resazurin (Rz) irradiated with artificial solar spectrum without UVC part for 2 h.

Synthesis	Solute	crystalline phase	$<d_{Scherrer}> \pm \Delta_S$ [nm]	degradation [%]
SG	water	amorphous	/	/
SG + aging	water	anatase	6.1 ± 1.2	29
SG	ethanol	anatase	3.2 ± 0.6	26
HT	water	anatase	4.0 ± 0.8	51
HT	ethanol	anatase	4.7 ± 0.9	46

Photocatalytic effect of samples prepared with SG and with HT synthesis was tested with resazurin (Rz) decomposing into resorufin (Rf) where we followed surface area under peaks 1 and 2 from Figure 34b. All measurements were done after 2 hours of UV irradiation. Results are presented in the last column of Table 18. Sample prepared in distilled water and left to age for 9 months decomposed 29 % of Rz, sample prepared with SG in ethanol degraded 26 %, sample additionally HT treated degraded 51 % of Rz if initial material was prepared in distilled water, if it was prepared in ethanol the degradation of Rz was 46 %.

Resazurin degrades into resorufin quickly. The change happens in the visible part of the light spectrum, therefore we can use this method “on the spot”. But the method has also disadvantages: preparation of the resazurin for the test takes time, the degradation of resazurin is complicated and limited to testing in acidic conditions, calculating the photocatalytic effect from UV-Vis spectrophotometer curves, see Figure 34b, is challenging (peaks 1 and 2 are low, peaks 3 and 4 are consisted of resazurin and resorufin, which is changing further on).[72] To avoid disadvantages when using resazurin, we used caffeine, see Table 19 and Figure 54.

4.3.2 Hierarchical structures

To compare the photocatalytic efficiency of hierarchical structures to normal anatase nanoparticles, we used as photocatalysts HT prepared material in distilled water with TO (see Figure 40), as well ST synthesised, calcinated and HT prepared hierarchical

structures (see Figure 48-53). In Figure 54 is presented photocatalytic effect of HT prepared nanopowder in distilled water.

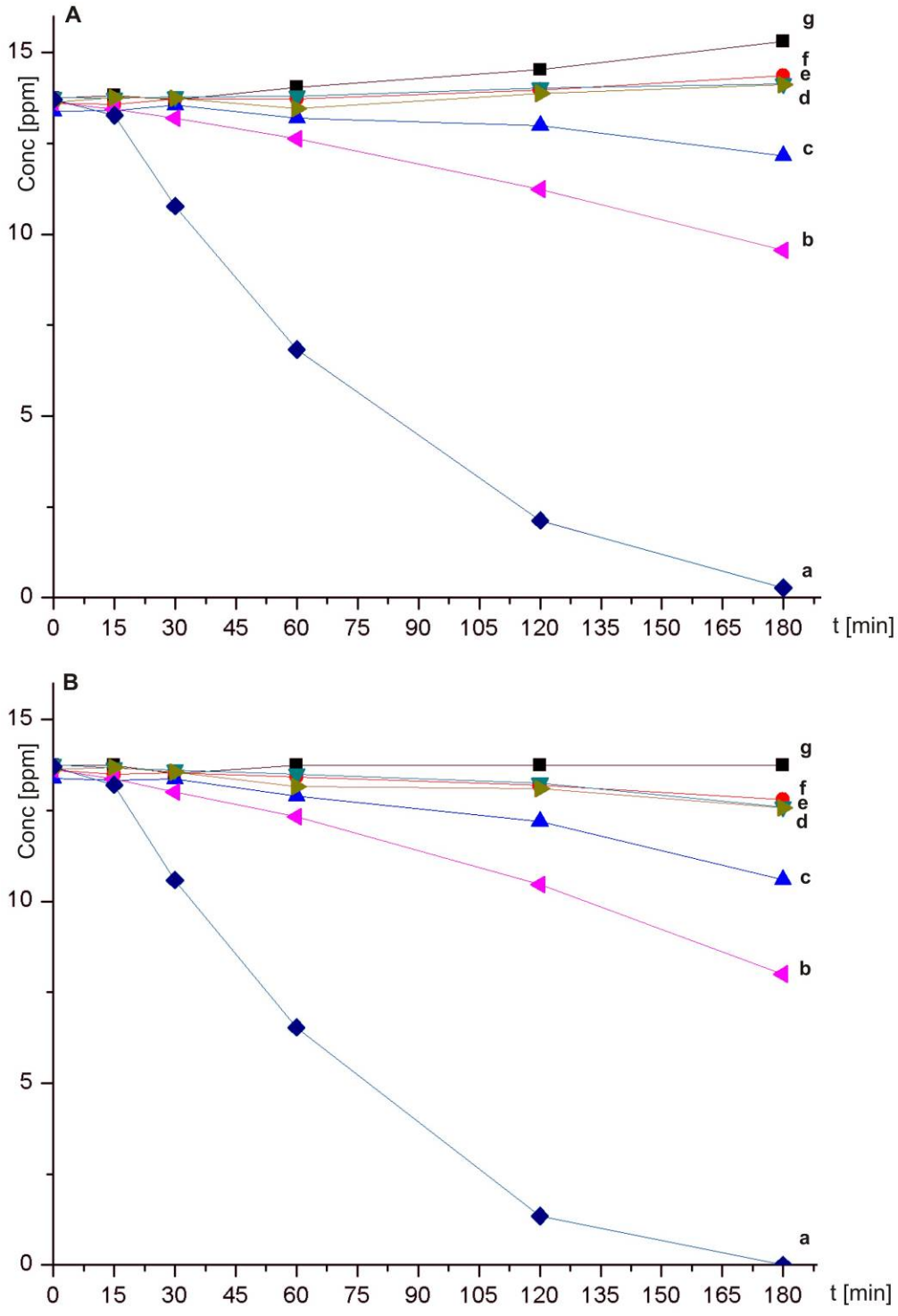

Figure 54: *Degradation of caffeine with and without catalyst*. A) Measurement, were evaporation had noticeable influence, and B) corrected measurement to exclude evaporation. Photocatalysis was tested with caffeine using a) commercial Degussa powder P25, b) powder hydrothermally treated TO at 200 ºC, c) sample calcined on 300 ºC and hydrothermally treated afterwards, d) sample calcined at 550 ºC, e) sample calcined at 550 ºC and hydrothermally treated, f) sample calcined at 350 ºC. Results were compared to g) photolysis of caffeine.

We always followed photolytic degradation (without the addition of TiO_2) besides

photocatalytic degradation of caffeine using prepared samples as photocatalysts. As reported in literature [127] caffeine is not degradable under UV light (photolysis). From Figure 54A a (photolysis of the caffeine) we can follow the evaporation which was for the all samples equal due to the equal conditions. With Equation 20-27 we have described the measured concentration with evaporation in all steps of photolysis.

$$c_N^B = \frac{m_0 - \sum_{j=1}^{N-1} \Delta m_j}{V_0 - \sum_{j=1}^{N} \Delta V_{izh\_j} - (N-1)\Delta V} \tag{20}$$

$$\Delta m_N = c_N^B \Delta V \tag{21}$$

$$c_N^A = \frac{m_0 - \sum_{j=1}^{N} \Delta m_j}{V_0 - \sum_{j=1}^{N} \Delta V_{izh\_j} - N\Delta V} \tag{22}$$

$$c_N^A = c_{N+1}^B \tag{23}$$

In photolysis concentration equations (Equation 20-23) c_N^B is the concentration of the caffeine before (B) N-th sampling (we took each time 2 ml of the liquid sample for the analysis, ΔV), c_N^A is the concentration of the resazurin after (A) N-th sampling, m_0 and V_0 are mass of the caffeine and volume of the solution before photolysis (and before photocatalysis), Δm_j represents the mass of the caffeine sampled on the j-th step, ΔV_{izh_j} volume of the evaporated distilled water on the j-th step (we calculated it from the first 15 min of the photolysis and considered it to be same for each 15 min).

From Equation 20-23 it is obvious that the measured concentration of the caffeine is higher due to the evaporation of water.

In eliminating the evaporation influence in the photocatalytic measurements, there was not only change in the concentration of the caffeine because of the evaporation, but also because of the degradation of the resazurin with photocatalysts, see Equation 24-27.

$$C_N^B = \frac{m_0 - \sum_{j=1}^{N-1} \Delta m_j - \sum_{j=1}^{N} \Delta m_j^D}{V_0 - \sum_{j=1}^{N} \Delta V_{izh\_j} - (N-1)\Delta V} \tag{24}$$

$$\Delta m_j = C_N^B \Delta V \tag{25}$$

$$C_N^A = \frac{m_0 - \sum_{j=1}^{N} \Delta m_j - \sum_{j=1}^{N} \Delta m_j^D}{V_0 - \sum_{j=1}^{N} \Delta V_{izh\_j} - N\Delta V} \tag{26}$$

$$C_N^A = C_{N+1}^B \tag{27}$$

In photocatalysis concentration equations (Equation 24-27) C_N^B is the concentration of the caffeine before (B) N-th sampling when photocatalysts are present, C_N^A is the concentration of the caffeine after (A) N-th sampling when photocatalysts are present, Δm_j^D represents the mass of the degraded (D) caffeine with photocatalysis just before sampling.

Δm_j from Equation 21 (instead of Equation 25) was included in Equation 24-26 from

which we calculated Δm_j^D, and used it to calculate the concentration of the caffeine in the ideal conditions without the evaporation. Results are shown in Figure 54B. Photocatalysis, due to the approximation of using Δm_j from photolysis, can be only higher from calculated values.

Calcined material at 350 ºC (see the curve f in Figure 54B), pure anatase, degraded 6 % of the caffeine in 3 h, while material calcined at 550 ºC (see the curve d in Figure 54B), found as anatase and rutile, degraded 7 % of the caffeine in 3 h. Hydrothermally treated sample that was calcined at 550 ºC (see the curve e in Figure 54B) increased degradation of the caffeine on 8 %.

Hydrothermally treated sample that was calcined at 300 ºC (see the curve c in Figure 54B), where calcination just removed organic compound from the flower-like powder (see FTIR in Figure 46) and left the shape intact (see Figure 45 of noncalcined powder and Figure 48 of on 300 º C calcined powder) and the material amorphous, degraded 21 % of the caffeine in the same time. This was the only material where flower-like structure consisted of nano anatase crystals after hydrothermal synthesis (see Figure 50).

Material prepared with hydrothermal synthesis at 200 ºC using just TO as a precursor degraded on the other hand 41 % of caffeine (see the curve b in Figure 54B), while commercial powder P25 degraded 99 % (see the curve a in Figure 54B). However, the hydrothermally treated calcined material was the one that was much more easily removed from the liquid after use due to micro-sized structures.

BET surface (see Table 19) of material calcined at 300 ºC and afterwards hydrothermally treated was 185 m^2g^{-1}, while material calcined at 550 ºC and afterwards hydrothermally treated was lower, i.e. 136 m^2g^{-1}. The difference between samples is about 50 m^2g^{-1}. BET surface area for P25 is 53 m^2g^{-1} according to the literature[128,129].

Table 19: *BET and photocatalytic results for various samples.* BET and photocatalytic results for: anatase crystals prepared from TO that was HT treated at 200 °C for 150 h; calcined flower-like structures that were hydrothermally treated at 120 °C for 12 h; commercial powder P25.

Sample	BET [m^2g^{-1}]	caffeine decomposition [%]
calcination at 300-600 °C	/	0
calcination at 300 °C + HT	185.3	21
calcination at 550 °C + HT	135.7	8
HT 200 °C, 150 h	/	41
P25	53.0	99

Band gap measurements were performed with UV-Vis spectrophotometer in reflectance mode. Measured intensity, A, was multiplied by the incoming light energy, $\hbar\omega$, squared for direct allowed band gaps, square rooted for indirect allowed band gaps, and plotted versus the incoming light energy, $\hbar\omega=hc/\lambda$, where h is Planck's constant, λ incoming light wavelength.[122]

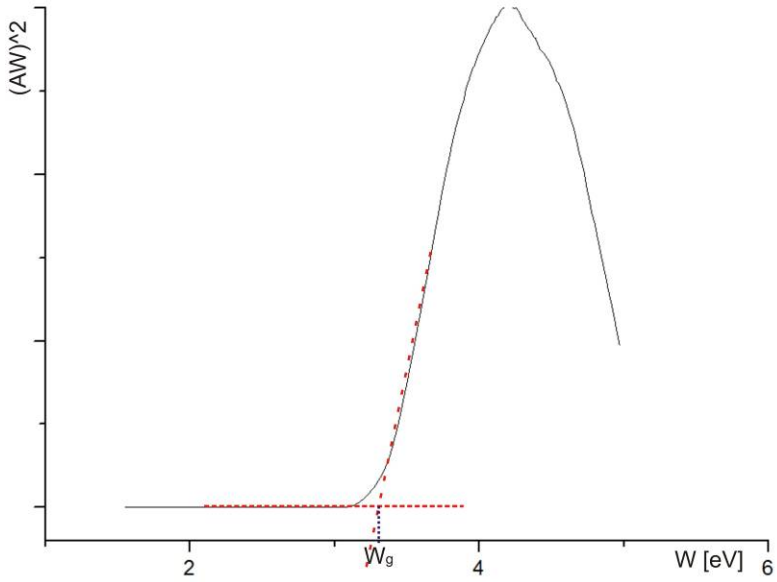

Figure 55: *Band gap measurement*. Band gap estimation for commercial powder P25. Linear plot intersection with the x-axis represents the band gap. Results are presented in Table 20.

HT treated samples prepared with TO consist of anatase and brookite. Anatase has indirect band gap, while brookite has direct band gap. We calculated both and presented results in Table 20. For flower-like structures calcined at 300 °C and afterwards hydrothermally treated we could calculate just direct band gap because graph for indirect band gap could not be plotted by 2 straight lines. However its direct band gap was estimated to 2.9 eV. Flower-like material calcined on 550 °C and also afterwards hydrothermally treated had a bit bigger band gap with the value 3.0 eV and with indirect band gap 2.9 eV. The same band gap values for direct and indirect band gap had also crystals prepared only with HT synthesis at 200 °C for 150 h. We compared band gaps of prepared materials to band gap of Degussa P25, which has direct band gap 3.4 eV, indirect band gap 3.0 eV. Calculated band gap values for anatase, see Table 8, vary from 1.9 to 3.7, while measured anatase band gap is supposed to be 3.2 eV.

Table 20: *Band gap (W_g) values of prepared samples in comparison with P25.* E_g results for: anatase crystals prepared from TO that was HT treated at 200 °C for 150 h; commercial powder P25.

Sample	direct allowed E_g [eV]	indirect allowed E_g [eV]
calcination at 300 °C + HT	2.9	/
calcination at 550 °C + HT	3.0	2.9
HT 200 °C, 150 h	3.0	2.9
P25	3.4	3.0

5 Discussion

5.1 Nucleation and growth of nanocrystals

From Table 14 we can see that the size of the hydrothermally prepared crystals increased with the synthesis temperature and time from around 6 to 20 nm, while when performing cyclic hydrothermal synthesis (Table 13) the crystals just reshaped into final bipyramidal form.

With lower temperature and/or shorter time of hydrothermal synthesis the crystals had blocky appearance, and less defined surfaces. This is in agreement with Cho et al.[130], who observed that the longer the time and the higher the temperature of hydrothermal synthesis, the more defined and larger the final bipyramidal crystals are. On the contrary, if the temperature and/or time increased, then rod-like, asymmetrical and truncated bipyramidal crystals with better defined surfaces were obtained. If the temperature and time increased even more, bipyramidal anatase crystals developed. In order to explain this behaviour we have for the first time reconstructed the actual crystal morphology based on our HRTEM observations of nanoparticles in different zone-axis and proposed a possible growth mechanism linking the observed evolution of crystals through a sequence of HT runs.

Figure 56 shows a set of observed three-dimensional shapes of anatase nanocrystals reconstructed for the first time from experimental HRTEM images viewed along different crystallographic projections: [100], [010] and [111]. Because TEM images only show a projection of the objects, individual crystal was carefully tilted into specific crystallographic orientation in order to observe its projected shape. From different orientations recorded on different, but morphologically alike, anatase crystals within the same sample it was possible to obtain a true 3D morphology of nanocrystals that are typical for the specific sample. For example, asymmetrically shaped truncated bipyramid shown in Figure 56a reflects the three unique projections displayed in Figure 42, while crystal shapes a–d in Figure 56, which always coexisted, could explain shapes of particles observed in Figure 41. On the other hand crystal shapes e-f in Figure 56 were observed only in Figure 40.

Figure 57 shows schematics of the evolution of bipyramidal anatase crystals. On the left side, an expected, “ideal” growth from a regular truncated bipyramid is shown. However, such evolution of crystal morphology was not confirmed. On the right side, is experimentally observed growth model, which was reported for the first time. In the initial stage of growth small, irregular blocky anatase nuclei are formed. Most of the surfaces of the crystals are of the {101} type, while some fractions of {001} surfaces are commonly present. At higher temperatures (and prolonged processing times) these nuclei become rod-like stretching along one of the bipyramidal <101> directions. Elongation along any of these axes results in a fairly uncommon habit for anatase with asymmetrically developed {101} planes, as shown in Figure 56 (c, d). On these crystals, pinacoidal {001} faces are much smaller than that on the initial crystallite, but still present. Many rod-like crystals tend to lose {001} facets and acquire a pointed habit. Rod-like anatase crystals further develop into somewhat wedge-shaped platy ones with

almost absent base pinacoids, shown in Figure 56 (a, b) (this growth variant is not shown in Figure 57 for simplicity).

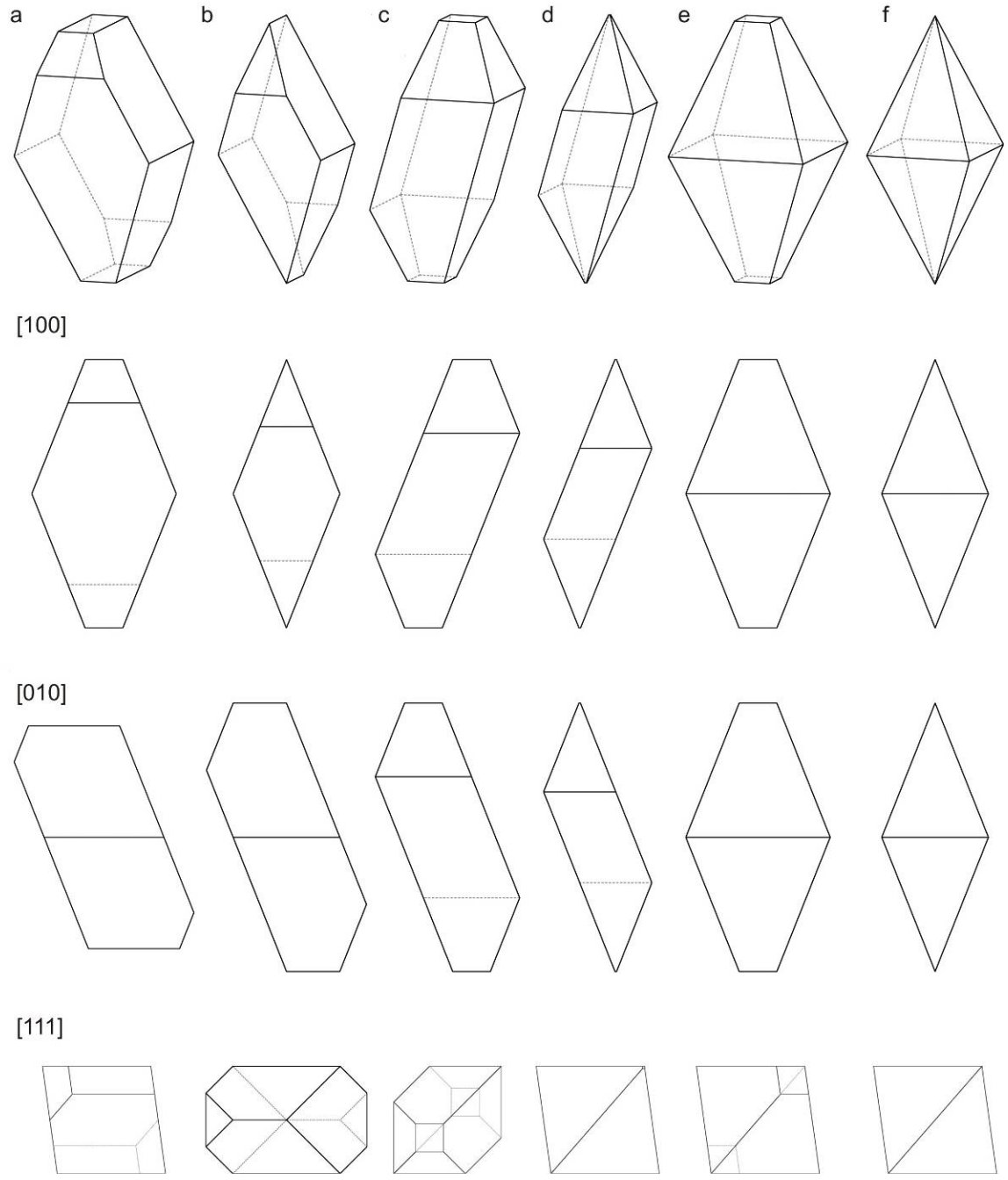

Figure 56: *Morphology of HT synthesized rod-like anatase crystals*. 3D models and their corresponding projections viewed along [100], [010] and [111] axes reconstructed for the first time from experimental HRTEM micrographs. a, b) Wedge-shaped crystals, c, d) elongated rod-like crystals, e, f) bipyramidal crystals, a, c, e) are truncated crystals, b, d, f) their non-truncated pairs respectively. In examined samples it was possible to find both variants, truncated and non-truncated and even combination of both i.e. one end of the crystal was truncated, a), c) or e), while the other end was not, b), d) or f) respectively.

The crystals in this growth stage are still fairly disproportional compared to what an idiomorphic anatase crystal ought to appear. In the final growth stage, if enough time is given to the crystals to reach their equilibrium shape, the crystals evolve into plain tetragonal bipyramids with prevailing {101} faces.

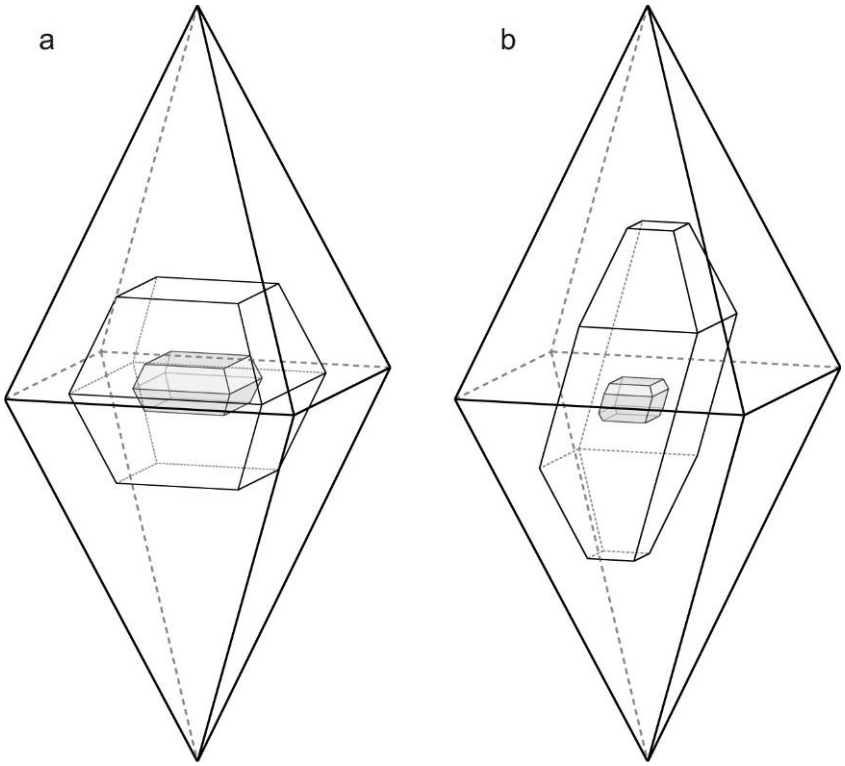

Figure 57: *The growth mechanism of bipyramidal anatase crystals*. a) Expected (ideal) growth from regular truncated bipyramid, and for the first time b) experimentally observed growth from irregular blocky nucleus into rod-like or wedge-shaped and finally into idiomorphic bipyramidal crystal. Irregular blocky-pinacoidal nuclei, centre of b), are seen in Figure 38a, final bipyramids in Figure 40c, elongated rod-like crystals, middle growth stage, were observed in samples in Figure 41 and Figure 42.

We have shown that in the initial stages of growth, anatase crystals adopt uncommon morphologies, which are a combination of basic crystallographic forms typical for anatase, however these forms are not developed symmetrically as determined by the surface energy values for these particular planes. The asymmetry and abnormal growth into rod-like and wedge-shaped crystals is most probably a consequence of inhomogeneous supply of building material due to high competition among numerous (relatively) rapidly growing randomly oriented nanocrystals. This leads to highly nonequilibrium conditions in the initial growth stages. Close to equilibrium, all crystals tend to adopt simple bipyramidal morphology. The surface energy values, W_S, of {101}, {100} and {001} planes are 0.91 J/m^2, 1.28 J/m^2 and 1.43 J/m^2 respectively[131]. In the experiments, we did not use any additives that would preferentially attach to certain surfaces, and thus modify the surface energies of these forms. Namely, many additions are known to favour certain crystallographic forms to grow, like in the case of the addition of fluorine ions that attach on the {001} planes, and hence lower the energy of this plane[132]. In our case, the system would tend to lower the surface energy by minimizing the area of the high-energy {001} planes. As a result, regular bipyramid, surrounded with low-energy {101} planes should grow. The formation of rod-like irregular (asymmetrical) bipyramids as the intermediate morphology could be explained with rapid tendency of diminishing the area of {001} planes.

Transformation from hydrothermally prepared anatase into rutile which was studied in situ with heating in TEM started at ~850 °C and was complete at ~900 °C. The temperature of the conversion from anatase to rutile at in situ experiments happens in wide temperature range.[133]

Anatase synthesised with sol-gel, solvothermal synthesis in glycerol and calcined at 300 °C, when organic phase is removed and the flower-like morphology stays unchanged, was amorphous, see Figure 44b. Calcination at even higher temperature led to formation of anatase phase (at 350 °C) and rutile phase. At temperatures higher than ~550 °C rutile started to from, at ~600 °C the rutile was only remaining TiO_2 crystal phase. The difference in the temperatures of the transformation from anatase to rutile was 300 °C in the benefit of the hydrothermal synthesis. The temperature of transformation from anatase, prepared with HT synthesis, into rutile, is in agreement with literature, where the transformation was done in conventional manner (heating of loose powder in the air).

From XRD from Figure 37 and Figure 43 we can conclude that in distilled water when using TO and performing hydrothermal synthesis, the resulting product always contain anatase with a small amount of brookite.

5.2 Self-assembly of microstructures

The formation of flower-like structures inside the bigger aggregates could be tentatively explained with the sequence of several steps for the first time. First step is the slow and partial hydrolysis of titanium-iso-propoxyde to amorphous titanium oxy-hydroxide and parallel formation of titanium glycerolate aggregates, which were never reported before. These aggregates (geodes), few 100 μm in size were porous and amorphous if prepared at 180 °C and partially crystalline in the case of preparation at 200 °C (Figure 47). During the solvothermal process the hydrolysed Ti-hydroxide based particles are dissolving and reacting with the glycerol (matrix solvent). Due to concentration gradient between outside and inside areas of the geodes there is a mass flow through the geodes where amorphous, foil-like forms of glycerolate are formed. To minimise the surface energy the foils are rolled and twisted. Most probably those elongated, rolled “leafs” have equal high surface charge prohibiting their aggregation in dense forms. Contrary, in order to minimise the contact areas between leafs and due to stearic effects the leafs forms the flower (or sea-urchin)-like morphologies. We never found flower-like particles outside the geodes after the solvothermal treatment supporting the proposed mechanism of their formation. With thorough washing in water and alcohol the flower-like particles were released from the geodes.

Calcination of flower-like particles resulted in the formation of anatase and/or rutile, depending on firing temperature (Figure 44), but due to relatively large anatase particles formed and due to coarsening of the shape the photocatalytic effect of this material was poor.

The verification of our original idea, to form hierarchical structures where flower-like forms would be used as a substrate for second-step hydrothermal synthesis was quite successful. When still amorphous flower-like structures were used (calcined at 300 °C), around 10 nm sized anatase nanoparticles grew on leafs in ordered manner, forming rows of particles (see Figure 50b). The BET specific surface area of this material is quite large, 185 m^2/g and the photocatalytic efficiency the highest among hierarchically structured materials we synthesised (curve c in the Figure 54B).

If already crystallised flower-like particles after calcination at 350 °C (Figure 49b), consisting mainly of anatase were used as a starting material for the second-step hydrothermal synthesis, the results were not so good. The morphology and the shape remains practically unchanged implicate that there was no additional deposition on nano-anatase particles. The BET surface area was lower (136 m^2/g) and photocatalysis negligible (curve e in the Figure 54B).

Interesting findings was also the material consisting of parallel, one micron sized pores (Figure 52) which was a by-product during the second-step hydrothermal synthesis

(regardless of the crystallinity of flower-like particles). The preparation of the porous material with μ-sized substrates was never reported before. According to experiments (see Figure 58) we presume that pores were created after the autoclave was put into the furnace and before the constant temperature in the vessel was reached. The difference in the temperature can be the only driving force for the mass flow, the not-uniformly distributed flower-like material on the bottom of the vessel the only reason for creation of µm-sized pores in the material. We observed the dependence of the pores size (µm) on the amount of the flower-like structures under the hydrolysed material. The more the flowers, the less the hydrolysed material above the flowers, the more the pores above the flowers and the bigger the pores above the flowers.

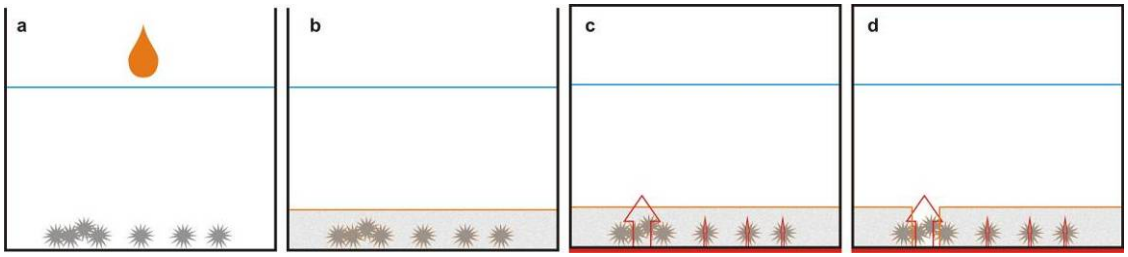

Figure 58: *Sketches of experimental observations of pores' formation*. a) Into the distilled water in the Teflon vessel we added calcined flower-like material. b) After addition of TO, hydrolysis took place, newly formed material (Ti-oxy-hydroxide) covered flower-like structures on the bottom of the vessel. c) The vessel was closed and put into furnace where it was in the contact with the surface with higher temperature at its bottom (before constant temperature was reached). d) Mass flow removed added material above the flower-like structures.

The reason for the stronger flow above the flower-like structures is the narrowing of the flow channels with flowers' needles. In Figure 59 there are sketches of minimal flow at the beginning "through" a) the flower, b) around the needle, around the spherical barrier c) with minimal mass flow, d) with heavy mass flow, and e) sketch of the mass flow when the channel narrows and consequently the pressure and the velocity of the mass flow increase. If there are more narrow channels i.e. more flower-like structures, there is more powerful mass flow (see Figure 59e) with which pores are crated. During the hydrothermal synthesis the viscosity of hydrolysed product increased, freezing the pores inside. The approach of the pores creation is therefore template-free with the transient hydrodynamic gradients, i.e. with the mass flow of the lighter particles, i.e. nanoparticles[134,135]. Creation of pores with flower-like structures is a negative to the possible creation of pores when spherical particles, which have volume filled with material, would be used. In the case of the flower-like structures the pressure, due to the flow and the channel narrowing, is bigger inside the vertical surface area covered by the flower-like structure. In the case of the spherical particles, the pressure is larger in the circumference perpendicular to the mass flow.

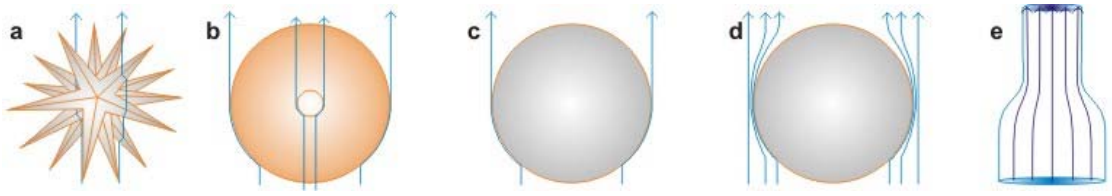

Figure 59: *Sketches of laminar mass flow*. Sketches of laminar mass flow (if there is just one stream) around a) flower-like structure b) its needle and c) sphere. d) Laminar mass flow around the sphere where there are uniform streams all over the available area. e) Increase of the mass flow velocity happens if the channel narrows. This happens in the case of the overlapping of the flower-like structures tiling in multiple layers.

5.3 Photocatalytic effect

G. Tian et. al.[126] solvothermally (glycerol and ethanol) prepared flower-like structures, calcined it on 450 ºC transforming the structure into anatase, that showed much better photocatalytic effect comparing to commercial powder P25 (consists of rutile, anatase and amorphous phase), while our solvothermally (glycerol) prepared and calcined material did not show any noticeable effect, unless additionally enriched with nanoanatase via second hydrothermal synthesis.

Side product after all hydrothermal synthesises hierarchical was porous material, which could not be split from flower-like structures, consisted from anatase nano crystals and therefore . We expected increased photocatalytic effect due to porous material, but according to Figure 54g (photocatalysis of the caffeine with material calcined at 550 ºC and hydrothermally treated afterwards), we concluded, that in liquid media porous material,

did not work as photocatalysts i.e. the only photocatalytic material that showed photocatalytic effect in liquid media was the flower-like structure enriched with anatase nanocrystals.

If we compare surfaces of the porous structures (see Figure 52) and flower-like structures calcined at 550 ºC (see Figure 51), we can presume that BET surface area of the flower-like structure is smaller due to the surface's weak diversification. BET specific surface area according to literature of porous titania can vary from more than 300 m^2g^{-1} to below 1 m^2g^{-1} when calcined[136].

The difference between the BET surface areas of our tested samples is only due to flower-like structure which is in the case of the material calcined at 300 ºC (with additional hydrothermal synthesis) covered with nanoanatase, while the flowers calcined at 550 ºC (with additional hydrothermal synthesis) have no nanoanatase particles on the surface. Flower-like structures with nanoanatase on the surface can therefore be used for photocatalysis in the liquid media, while porous material might be successfully used in the gas-phase photocatalysis[137].

Smaller photocatalytic activity in liquid of all our samples when compared to P25, even if it has much smaller BET surface area, is most probably due to the better dispersion of P25 in the liquid comparing to our 100-times bigger structures and optimised structure (composition with anatase, rutile and amorphous phase).

Nanoanatase prepared with hydrothermal and solvothermal (in ethanol) synthesis degraded ~20 % more resazurin than material prepared with SG synthesis in the same solute (see Table 18), because anatase crystals were after HT treatment more crystallised, with more defined morphology and shape, and with less amorphous material on the surface. Degradation after SG and after HT treatment was ~5 % better with material prepared in water than with material prepared in ethanol, most probably because morphology and shape of crystals in ethanol were less defined from crystals prepared in distilled water. Also crystals prepared in water were not perfectly defined, but were better from crystals prepared in ethanol.

6 Conclusions

TiO_2 in the anatase crystal modification was prepared via hydrothermal synthesis at temperatures from 20 °C to 200 °C and times from 50 h to 150 h. Particle size and morphology were determined from XRD pattern and electron microscopy images. From high-resolution TEM images, the shape of crystals and growth was reconstructed for the first time. It was found, also for the first time, that in the initial stages of growth anatase crystals adopt uncommon morphologies, which were a combination of basic crystallographic forms typical for anatase, however these forms were not developed symmetrically as determined by the surface energy values for these particular planes. The asymmetry and abnormal growth into rod-like and wedge-shaped crystals was most probably a consequence of inhomogeneous supply of building material due to high competition among numerous (relatively) rapidly growing randomly oriented nanocrystals. This leads to highly nonequilibrium conditions in the initial growth stages. Close to equilibrium at higher temperatures and times all crystals tend to adopt simple bipyramidal morphology.

With the time and temperature of the synthesis, the crystals grew from around 6 to 20 nm and were transformed into a final bipyramidal shape through several intermediate stages, including blocky-pinacoidal, elongated rod-like and wedge-shaped morphologies. In the initial stage of growth, small, irregular blocky anatase nuclei are formed. Most of the surfaces of the crystals are of the {101} type, while large fractions of {001} surfaces are commonly present. At higher temperatures (and prolonged processing times), these nuclei become rod-like stretching along one of the bipyramidal <101> directions. Elongation along any of these axes results into fairly uncommon habit for anatase with asymmetrically developed {101} planes. On these crystals pinacoidal {001} faces are much smaller than that on the initial crystallite, but still present. Many rod-like and wedge-shaped crystals tend to lose {001} facets and acquire pointed habit. The crystals in this growth stage are still fairly disproportional compared to what an idiomorphic anatase crystal ought to appear. The formation of rod-like irregular (asymmetrical) bipyramids as the intermediate morphology could be explained with rapid tendency of diminishing the area of {001} planes. In the final growth stage, if enough time is given for the crystals to reach their equilibrium shape, the crystals evolve into plain tetragonal bipyramids with prevailing {101} faces.

In situ transformation in TEM of hydrothermally prepared anatase into rutile started at ~850 °C and was complete at ~900 °C. Anatase synthesised with sol-gel, solvothermal synthesis in glycerol and calcination started to transform into rutile at ~550 °C, while at ~600 °C the rutile was only remaining TiO_2 crystal. The difference in the temperatures of the transformation from anatase to rutile was 300 °C in the benefit of the hydrothermally synthesized material, which was tested in situ in TEM.

Nanocrystals tend to aggregate into bigger structures to minimize the high surface energy.[138] The aggregates prepared with sol-gel and hydrothermal route are up to several hundreds nm big. They are hard to completely break apart even with ultrasonic treatment, because surface was not treated with any surfactants that would help avoiding agglomeration. Agglomeration is completely random and dependent mainly on Brownian motion, therefore unique micro structures were formed from nanocrystals. During

solvothermal synthesis, amorphous and crystalline Ti-glycerolate flower-like structures were formed. For the first time it was observed that these structures form in the geodes with self-assembly. Structures were consisted of twisted/rolled nanosheets that contained high amount of organic phase, which was removed with calcination already at 300 °C without destroying the flower-like morphology and without crystallisation. Flower-like structures were approximately 10^3 bigger from anatase crystals prepared with hydrothermal route.

With assisted assembly using amorphous flower-like material as a substrate in additional hydrothermal synthesis with TO we prepared environmentally more suitable photocatalytic material which might be used for waste water remediation and air purification. The resulting material consisted of flower-like structures covered with 10 nm sized anatase nanocrystals (perspective for water purification), that was not yet published before, and microporous material exhibiting parallel micron-sized pores (perspective for air cleaning), which were created with mass flow influenced by barriers on the bottom of the Teflon cartridge, i.e. by μ-sized flower-like structures, which was also never before synthesised in this way, and also never before synthesised in any easier way. Diameter of the pores was in the range of the diameter of the flower-like structures, length of the pores up to 50 μm. BET surface area was ~3.5-times larger than BET specific surface area of commercial powder TiO_2 powder P25. Band gap of nanocrystals was much smaller from P25, i.e. 3.0 eV, which is 0.4 eV less than band gap of P25. P25 is photocatalyst just in UV spectrum, while our material might be active also in the visible part of the solar spectrum with direct allowed band gap 3.0 eV, which unfortunately also speeds up the recombination of the charge carriers when compared to the band gap of P25.

7 Acknowledgements

This work was financially supported by the Slovenian Research Agency under Grant No. 1000-08-310086 and project J2-4309.

I am very grateful to the entire Department of Nanostructured Materials, K7, from the Jožef Stefan Institute, for giving me an opportunity to work in a very good multidisciplinary team. I am thankful also to all the co-workers for all the nano-debates which helped me with my research. A very big thank you goes to young researchers and students working with TiO_2 and other semiconductors for all the debates.

Special gratitude goes to my supervisor, Asst. Prof. Dr. Goran Dražić, for all the encouragement, advice, explanations, support and for all the time he used to help me understand especially the chemical and material part of my postgraduate research. I am thankful for all the knowledge he passed on to me, from theory to practical usage of many different apparatus and electron microscopes. I am very grateful that I got the opportunity to work with the most patient and understanding supervisor with a very wide knowledge from many different research fields.

I am also grateful to Asst. Prof. Dr. Aleksander Rečnik for helping me solve many microstructural difficulties, for all the explanations about crystallography, and for all the help with transmission electron microscopes.

At the end, I would also like to thank my parents, who stood by me all the time during my PhD studies.

8 References

1. Statistični urad Republike Slovenije. 7 miljard prebivalcev Zemlje. Available at: http://www.stat.si/novica_prikazi.aspx?id=4317. 02. 07. 2013.
2. Delo in dom. Le še odstotek pitne vode. Available at: http://www.deloindom.si/le-se-odstotek-pitne-vode. 02. 07. 2013.
3. Shen P, Hwang SL, Chu HT, Yui ZF, Pan C, Huang WL. On the transformation pathways of alpha-PbO2-type TiO_2 at the twin boundary of rutile bicrystals and the origin of rutile bicrystals. Eur. J. Mineral. 2005; 17 (4): 543–552.
4. El Goresy A, Chen M, Gillet P, Dubrovinsky L, Graup G, Ahuja R. A natural shock-induced dense polymorph of rutile with α-PbO2 structure in the suevite from the Ries crater in Germany. Earth Planet. Sci. Lett. 2001; 192 (4): 485–495.
5. Sato H, Endo S, Sugiyama M, Kikegawa T, Shimomura O, Kusaba K. Baddeleyite-Type High-Pressure Phase of TiO_2. Science. 1991; 251 (4995): 786–788.
6. El Goresy A, Chen M, Dubrovinsky L, Gillet P, Graup G. An ultradense polymorph of rutile with seven-coordinated titanium from the Ries crater. Science. 2001; 293 (5534): 1467–70.
7. Simons PY, Dachille F. The structure of TiO_2II, a high-pressure phase of TiO_2. Acta Cryst. 1967; 23: 334–336.
8. Marchand R, Brohan L, Tournoux M. A new form of titanium dioxide and the potassium octatitanate K2Ti8O17. Mater. Res. Bull. 1980; 15 (8): 1129–1133.
9. Latroche M, Brohan L, Marchand R, Tournoux M. New hollandite oxides: TiO_2(H) and K0.06TiO_2. J. Solid State Chem. 1989; 81 (1): 78–82.
10. Akimoto J, Gotoh Y, Oosawa Y, Nonose N, Kumagai T, Aoki K, Takei H. Topotactic Oxidation of Ramsdellite-Type Li0.5TiO_2, a New Polymorph of Titanium Dioxide: TiO_2(R). J. Solid State Chem. 1994; 113 (1): 27–36.
11. Dubrovinskaia NA, Dubrovinsky LS, Ahuja R, Prokopenko VB, Dimitriev V, Weber HP, Osorio-Guillen JM, Johansson B. Experimental and Theoretical Identification of a New High-Pressure TiO_2 Polymorph. Phys. Rev. Lett. 2001; 87 (1): 275501–275505.
12. Mattesini M, de Almeida JS, Dubrovinsky L, Dubrovinskaia L, Johansson B, Ahuja R. High-pressure and high-temperature synthesis of the cubic TiO_2 polymorph. Phys. Rev. B. 2004; 70 (21): 212101–212105.
13. Dubrovinsky LS, Dubrovinskaia NA, Swamy V, Muscat J, Harrison NM, Ahuja R, Holm B, Johansson B. Materials science: The hardest known oxide". Nature. 2001; 410: 653–654.
14. Kalanasundaram K. Dye-Sensitized Solar Cells. Lausanne: EPFL Press, CRC Press; 2010.
15. Wyckoff RWG. Crystal Structures 1, Second edition. New York: Interscience Publishers; 1963.
16. Di Paola A, Bellardita M, Palmisano L. Brookite, the Least Known TiO_2 Photocatalyst. Catalysts. 2013; 3 (1): 36–73.

17. Jolyon R. The mineral and locality database. Available at: http://www.mindat.org. 05. 07. 2013.

18. Pauling L. Selected Scientific Papers, Volume 1, Structure of complex ionic crystals. Singapore: World Scientific; 2001.

19. Winkler J. Titanium Dioxide, Physical properties. Hannover: Vincentz Network; 2003.

20. Zhang HZ, Banfield JF. Thermodynamic analysis of phase stability of nanocrystalline titania. J. Mater. Chem. 1998; 8: 2073–2076.

21. Gribb AA, Banfield JF. Particle size effects on transformation kinetics and phase stability in nanocrystalline TiO_2. Am. Mineral. 1997; 82: 717–728.

22. Hwu Y, Yao YD, Cheng NF, Tung CY, Lin HM. X-ray absorption of nanocrystal TiO_2. Nanostruct. Mater. 1997; 9 (1–8): 355–358.

23. Zhang HZ, Banfield JF. Understanding Polymorphic Phase Transformation Behavior during Growth of Nanocrystalline Aggregates: Insights from TiO_2. J. Phys. Chem. B. 2000; 104 (15): 3481–3487.

24. Zhang JH, Chan CK, Porter JF, Guo W. Micro-Raman spcetroscopic characterization of nanosized TiO_2 powders prepared by vapor hydrolysis. J. Mater. Res. 1998; 13 (9): 2602–2609.

25. AM Sackler. Nanoscience: Underlying Physical Concepts and Phenomena, Washington: National Achamedy of Science: 2001.

26. XS Ye, Sha J, Zhang LD. Thermoanalytical characteristic of nanocrystalline brookite-based titanium dioxide. Nanostruct. Mater. 1997; 8 (7): 919–927.

27. Kominami H, Kohno M, Kera Y. Synthesis of brookite-type titanium oxide nano-crystals in organic media. J. Mater. Chem. 2000; 10: 1151–1156.

28. Landmann M, Rauls E, Schmidt WG. The electronic structure and optical response of tutile, anatase and brookite TiO_2. J. Phys. Condens. Matter. 2012; 24 (19): 195503–195508.

29. Grätzel M, Rotzinger FP. The influence of the crystal lattice structure on the conduction band energy of oxides of titanium(IV). Chem. Phys. Lett. 1985; 118 (5): 474–477.

30. Mo SD, Ching WY. Electronic and optical properties of three phases of titanium dioxide: Rutile, anatase and brookite. Phys. Rev. B. 1995; 51: 13023–13032.

31. Park JY, Lee C, Jung KW, Jung D. Structure related photocatalytic properties of TiO_2. Bull. Korean Chem. Soc. 2009; 30 (2): 402–404.

32. Yin AY, Chen S, Yang JH, Gong XG, Yan Y, Wei SH. Effective band gap narrowing of anatase TiO_2 by strain along a soft crystal direction. Appl. Phys. Lett. 2010; 96: 221901–221903.

33. Bloss FD. An Introduction to the Methods of Optical Crystallography. New York: Holt, Rinehart and Winston: 1961.

34. Mineralogy Database. Available at: http://webmineral.com. 05. 07. 2013.

35. Scherrer P. Bestimmung der Grösse und der Inneren Struktur von Kolloidteilchen Mittels Röntgenstrahlen. Nachrichten von der Gesellschaft der Wissenschaften, Göttingen, Mathematisch-Physikalische Klasse. 1918; 2: 98-100.

36. Chen X, Mao S. Titanium Dioxide Nanomaterials: Synthesis, Properties, Modifications, and Applications. Chem. Rev. 2007; 107: 2891–2959.

37. Stadelman P. EMS, Electron Microscopy Simulation. Available at: http://www-

hrem.msm.cam.ac.uk/hrem/local/ems/. 14. 08. 2013.

38. Edwards HGM, Hassan NFN, Middelton PS. Anatase–a pigment in ancient work or a modern usurper?. Anal. Bioanal. Chem. 2006; 384 (6): 1356–1365.

39. Sasahara A, Tamura H, Tanaka K. The role of Rh on Pt-based catalysts: structure sensitive NO + H_2 reaction on Pt(110) and Pt(100) and structure insensitive reaction on Rh/Pt(110) and Rh/Pt(100). Catal. Lett. 1994; 28: 161–166.

40. Dobrushin RL, Kotecky R, Shlosman SB. Wulff construction: A global shape from local interaction. Providence: American Mathematical Society; 1992.

41. Ganghoffer JF. Thermodynamics of Surface Growth with Application to Bone Remodeling. Rijeka: InTech; 2011.

42. Natural Earth Paint, eco-friendly paint kits. Available at: http://www.naturalearthpaint.com/shop /titanium-white-rutile. 15. 07. 2013.

43. Cinkarna Celje. About Titanium Dioxide. Available at: http://www.cinkarna.si/si/files/default/tio2/tdma_about_tio2__20120914.pdf. 14. 07. 2013.

44. Fujishima A, Hashimoto K, Watanabe T. TiO_2 Photocatalysis Fundamentals and Applications. Tokyo: Bkc Inc.; 1999.

45. Chen X, Mao S. Titanium Dioxide Nanomaterials: Synthesis, Properties, Modifications, and Applications. Chem. Rev. 2007; 107: 2891–2959.

46. Fujishima A, Honda K. Electrochemical Photolysis of Water at a Semiconductor Electrode. Nature. 1972; 238: 37–38.

47. Fujishima A, Kohayakawa K, Honda K. J. Electrochem. Soc. 1975; 122: 1487.

48. Foster HA, Ditty IB, Varghese S. Photocatalytic disinfection using titanium dioxide: spectrum and mechanism of antimicrobial activity. Appl. Microbiol. Biotechnol. 2011; 90: 1847–1968.

49. Chung CJ, Lin HI, Chou CM, Hsieh PY, Hsiao CH, Shi ZY, He YL. Inactivation of Staphylococcus aureus and Escherichia coli under various light sources on photocatalytic titanium dioxide thin film. Surf. Coat. Tech. 2009; 203 (8): 1081–1085.

50. Franco A, Nves MC, Ribeiro Carrott MML, Mendonca MH, Pereira MI, Monteiro OC. Photocatalytic decolorization of methylene blue in the presence of TiO_2/ZnS nanocomposites. J. Hazard. Mater. 2009; 161 (1): 545–550.

51. Mahalakshmi M, Vishnu Priya S, Arabindoo B, Palanichamy M, Murugesan V. Photocatalytic degradation of aqueous propoxur solution using TiO_2 and H zeolite-supported TiO_2. J. Hazard. Mater. 2009; 161 (1): 336–343.

52. Ollis DF, Pelizzetti E, Serpone N. Photocatalyzed destruction of water contaminants. Environ. Sci. Technol. 1991; 25 (9): 1522–1529.

53. Li J, Xu J, Dai WL, Li H, Fan K. Direct hydro-alcohol thermal synthesis of special coreshell structured Fe-doped titania microspheres with extended visible light response and enhanced Photoactivity.Appl. Catal. B-Environ. 2009; 85 (3–4): 162–170.

54. Fassier M, Chouard N, Peyratout CS, Smith DS, Riegler H, Kurth DG, Ducroquertz C, Bruneaux MA. Photocatalytic activity of oxide coatings on red clay substrates. J. Eur. Ceram. Soc.. 2009; 29 (4): 565–570.

55. Nishikawa H, Takahara Y. Adsorption and photocatalytic decomposition of odor compounds containing sulfur using TiO_2/ SiO_2 bead. J. Mol. Catal. A: Chem.. 2001; 172 (1–2): 247–251.

56. Sulekha.com B2B. TiO_2 Photocatalyst mosquito trap. Available at:

http://b2b.sulekha.com/tio2-photocatalyst-mosquito-trap_product_215209. 14. 07. 2013.

57. Ribeiro M, Monteiro FJ. Infection of orthopedic implants with emphasis on bacterial adhesion process and techniques used in studying bacterial-material interactions. Biomatter. 2012; 2: 176−194.

58. Suyama Y, Otsuki M, Ogisu S, Kishikawa R, Tagami J, Ikieda M, Kurata H, Cho T. Effects of light sources and visible light-activated titanium dioxide photocatalyst on bleaching. Dent. Mater. J. 2009; 28 (6): 693−699.

59. Maneerat C, Hayata Y, Egashira N, Sakamoto K, Hamai Z, Kuroyanagi M. Photocatalytic reaction of TiO_2 to decompose ethylene in fruit and vegetable storage. T ASAE. 2003; 46 (3): 725–730.

60. Dylla H. The effects of highway environmental conditions on photocatalytic pavement's ability to reduce nitrogen oxides. A Thesis Submitted to the Graduate Faculty of the Louisiana State University and Agricultural and Mechanical College in partial fulfillment of the requirements for the degree of Master of Science in The Interdepartmental Program in Engineering Science. 2011.

61. Baraton MI. Nano- TiO_2 for dye-sensitized solar cells. Recent Pat. Nanotechnol. 2011; 6 (1): 10–15.

62. Curulli A, Valentini F, Padeletti G, Viticoli M, Caschera D, Palleschi G, Smart (Nano) materials: TiO_2 nanostructured films to modify electrodes for assembling of new electrochemical probes. Sensor. Actuat. B-Chem. 2005; 111–112: 441–449.

63. Hagfeldt A, Vlachopoulos N, Grätzel M. Fast Electrochromic Switching with Nanocrystalline Oxide Semiconductor Films. J. Electrochem. Soc. 1994; 141 (7): 82−84.

64. Bai H, Liu Z, Sun DD. Hierarchically multifunctional TiO_2 nano-thorn membrane for water purification. Chem. Comm. 2010; 46 (35): 6542–6544.

65. Choi H, Stathatos E, Dionysiou DD. Sol–gel preparation of mesoporous photocatalytic TiO_2 films and TiO_2/Al_2O_3 composite membranes for environmental applications. Appl. Catal. B: Environmental. 2006; 63: 60–67.

66. EFSA. Opinion of the Scientific Panel on Food Additives, Flavourings, Processing Aids and materials in Contact with Food on a request from the Commission related to the safety in use of rutile titanium dioxide as an alternative to the presently permitted anatase form. The EFSA Journal. 2004; 163: 1–12.

67. Sensient. Cosmetics, Titanium Dioxide Overview. Available at: http://sensient-tech.com /cosmetics_sku_color/titanium_dioxide_overview.htm. 15. 07. 2013.

68. Yaghi OM, O'Keeffe M, Ockwig NW, Chae HK, Eddaoudi M, Kim J. Reticular synthesis and the design of new materials. Nature. 2003; 423: 705–714.

69. Gao G. Nanostructures & nanomaterials, Synthesis, Properties & Applications. London: Imperail College Press; 2004.

70. Suneel, SD. Wet Chemical Synthesis of nanomaterials. Available at: http://www.gitam.edu /eresource/nano/nanotechnology/bottamup%20app.htm. 14. 07. 2013.

71. Byrappa K, Adschiri T. Hydrothermal technology for nanotechnology. Prog. Cryst. Growth Charact. Mater. 2007; 53: 117–166.

72. Cho CH, Han MH, Kim DH. Morphology evolution of anatase TiO_2 nanocrystals under a hydrothermal condition (pH=9.5) and their ultra-high photocatalytic activity. Mat. Chem. Phys. 2005; 92 (1): 104–111.

73. Deng Q, Wei M, Ding X, Jiang L, Wei K, Zhou H. Large single-crystal anatase TiO_2 Bipyramids. J. Cryst. Growth. 2010; 312 (2): 213–219.

74. Wang KL, Wang G, Deng K, Tang D. Study on the shape control and photocatalytic activity of high-energy anatase Titania. Appl. Catal. B: Environmental. 2010; 100 (1–2): 378–385.

75. Chen Y, He X, Zhao X, Yuan Q, Gu X. Preparation, characterization, and growth mechanism of a novel aligned nanosquare anatase in large quantities in the presence of TMAOH. J. Colloid Interface Sci.. 2007; 310 (1): 171–177.

76. Barnard AS, Curtiss LA. Prediction of TiO_2 Nanoparticle Phase and Shape Transitions Controlled by Surface Chemistry. Nano lett. 2005; 5 (7): 1261–1266.

77. Feng H, Barbosa-Canovas GV, Weiss J. Ultrasound Technologies for Food and Bioprocessing, Food Engineering Series. Acoustic Cavitation. New York, Dordrecht, Heidelberg, London: Springer; 2011.

78. Nanotechnology. Available at: http://people.bath.ac.uk/acb40/Dreamweaver%20Website/nanometrologyandnanomanufacturing.html. 15. 07. 2013.

79. Suneel, SD. Role of Bottom-up and Top-Down approaches in Nano technology. Available at: http://www.gitam.edu/eresource/nano/NANOTECHNOLOGY/role_of_bottomup_and_topdown_a.htm. 15. 07. 2013.

80. Whitesides GM, Grzybowski B. Self-Assembly at All Scales. Science. 2002; 295 (5564): 2418–2421.

81. O'Mahony CT, Farrell RA, Holmes JD, Morris MA. Thermodynamics–Systems in Equilibrium and Non-Equilibrium. The thermodynamics of defect formation in self-assembled systems; 2011.

82. Dabbs DM, Aksay IA. Self-assembled ceramics produced by complex-fluid templation. Annu. Rev. Phys. Chem.. 2000; 51: 601–622.

83. Dhotel A, Chen Z, Delbreilh L, Youssef B, Saitre JM, Tan L. Molecular Motions in Functional Self-Assembled Nanostructures. Int. J. Mol. Sci. 2013; 14 (2): 2303–2333.

84. Colfen H, Antonietti M. Mesocrystals: Inorganic Superstructures Made by Highly Parallel Crystallization and Controlled Alignment. Angew. Chem. Int. Ed. Engl. 2005; 44 (35): 5576−5591.

85. Grzelczak M. Directed Self-Assembly of Nanoparticles. ACS Nano. 2010; 4 (7): 3591–3605,

86. Mali SS, Shinde PS, Betty CA, Bhosale PN, Lee WJ, Patil PS. Nanocoral architecture of TiO_2 by hydrothermal process: Synthesis and characterization. Appl. Surf. Sci. 2011; 257 (23): 9737–9746.

87. Hayashi K, Nakamura M, Makita Y, Fujiwara R, Kori T, Ishimura K. Synthesis and photocatalytic activity of sea urchin-shaped rutile TiO_2 nanocrystals. Mat. Lett. 2011; 65 (19–20): 3037–3040.

88. Wang W, Wang W, Xu HX. A Facile Method for Synthesizing TiO_2 Sea-Urchin Like Structures and Their Applications in Solar Energy Harvesting. Chinese Physics Letters 28 (2011) 0781031–0781034

89. Kong E, Chang Y, Park Y, Yoon Y, Park H, Jang H. Sea urchin TiO_2-nanoparticle hybrid composite photoelectrodes for CdS/CdSe/ZnS quantum-dot-sensitized solar cells. Phys. Chem. Chem. Phys. 2012; 14 (13): 4620–4625.

90. Cheng O, Pavlinek V, He Y, Yan Y, Li C, Saha P. Synthesis and electrorheological characteristics of sea urchin-like TiO_2 hollow spheres. Colloid. Polym. Sci. 2011; 289:

799–805.

91. Guo F, Su X, Hou G, Liu Z, Mei Z. Fabrication of superhydrophobic TiO_2 surface with cactus–like structure by a facile hydrothermal approach. Colloid. Surface. A: Physicochemical and Engineering Ascpects. 2012; 395: 70–74.
92. Tian G, Chen Y, Zhou W, Pan K, Tian C, Huanf X, Fu X. 3D hierarchical flower–like TiO_2 nanostructure: morphology control and its photocatalytic property. CrystEngComm. 2011; 13: 2994–3000.
93. Li Q, Liu B, Li Y, Liu R, Li X, Li D, Yu S, Liu D, Wang P, Li B, Zou B, Cui T, Zou G. Ethylene glycol–mediated synthesis of nanoporous anatase TiO_2 rods and rutile TiO_2 self–assembly chrysanthemums. J. Alloys Comp. 2009; 471 (1–2): 477–480.
94. Masuda Y, Ohji T, Kato K. Multineedle TiO_2 Nanostructures, Self–Assembled Surface Coatings, and Their Novel Properties. Cryst. Growth Des. 2010; 10 (2): 913–922.
95. Ye M, Liu HY, Lin C, Lin Z. Hierarchical Rutile TiO_2 Flower Cluster–Based High Efficiency Dye–Sensitized Solar Celly via Direct Hydrothermal Growth on Cundocting Substrates. Small. 2013; 9 (2): 312–321.
96. Wu J, Song X, Ma L, Wei X. Hydrothermal growth of multi–facet anatase spheres. J. Cryst. Growth. 2011; 319 (1): 57–63.
97. Horvat B, Rečnik A, Dražić G. The growth of anatase crystals during hydrothermal synthesis. J. Cryst. Growth. 2012; 347 (1): 19–24.
98. Wang X, Yu JC, Ho C, Hou Y, Fu X. Photocatalytic Activity of a Hierarchically Macro/Mesoporous Titania. Langmuir. 2005; 21 (6): 2552–2559.
99. Wang X, Caruso RA. Enhancing photocatalytic activity of Titania materials by using porous structures and the addition of gold nanoparticles. J. Mat. Chem. 2011; 21: 20–28.
100. Collins A, Carriazo D, Davis SA, Mann S. Spontaneous template–free assembly of ordered macroporous titania. Chem. Commun. 2004; 5: 568–569.
101. Yu BJ, Su Y, Cheng B. Template–Free Fabrication and Enhanced Photocatalytic Activity of Hierarchical Macro–/Mesoporous Titania. Adv. Funct. Mater. 2007; 17: 1984–1990.
102. Ohtani B, Prieto-Mahaney OO, Li D, Abe R. What is Degussa (Evonik) P25? Crystalline composition analysis, reconstruction from isolated pure particles and photocatalytic activity test. J. Photochem. Photobiol. A. 2010; 216 (2–3): 179–182.
103. Fujishima A, Honda K. Electrochemical Photolysis of Water at a Semiconductor Electrode. Nature. 1972; 238: 37–38.
104. Nowotny MK, Bogdanoff P, Dittrich T, Piechter S, Fojishima A, Tribursch H. Observations of p-type semiconductivity in titanium dioxide at room temperature. Mat. Lett. 2019; 64 (8): 928–930.
105. Silva AMT, Nouli E, Carmo-Apolinario AC, Xekoukoulotakis NP, Mantzavinos D. Sonophotocatalytic H_2O_2 degradation of phenolic compounds in agro-industrial effluents. Cat. Today. 2007; 124 (3–4): 232–239.
106. Kalebaila KK. Synthesis, characterization and assembly of metal chalogenide nanoparticles into nanostructured gels. Dissertation, AAI3277927.
107. Fassier M, Chouard N, Peyratout CS, Smith DS, Riegler H, Kurth DG, Ducroquertz C, Bruneaux MA. Photocatalytic activity of oxide coatings on red clay substrates. J. Eur. Ceram. Soc. 2009; 29 (4): 565–570.

108. Cho CH, Kim DK. Photocatalytic Activity of Monodispersed Spherical TiO_2 Particles with Diferent Crystallization Routes. J. Am. Ceram. Soc. 2003; 86 (7): 1138–1145.

109. Xu G, Zheng Z, Wu Y, Feng N. Effect of silica on the microstructure and photocatalytic properties of titania. Ceram. Int. 2007; 35 (1): 1–5.

110. Yoon J, Shim E, Bae S, Joo H. Application of immobilized nanotubular TiO_2 electrode for photocatalytic hydrogen evolution: Reduction of hexavalent chromium (Cr(V I)) in water. J. Hazard. Mater. 2009; 161 (2–3): 1069–1074.

111. Wang W, Gomes Silva C, Faria JL. Photocatalytic degradation of Chromotrope 2R using nanocrystalline TiO_2/activated-carbon composite catalysts. Appl. Catal. B: Environmental. 2006; 70 (1–4): 470–478.

112. Tryba B, Piszcz M, Grzmil B, Pattek-Janczyk A, Moravski AW. Photodecomposition of dyes on Fe- C-TiO_2 photocatalysts under UV radiation supported by photo-Fenton process. J. Hazard. Mater. 2009; 162 (1): 111–119.

113. Wang S, Gongm Q, Liang J. Sonophotocatalytic degradation of methhy orange by carbon nanotube TiO_2 in aqueous solutions. Ultrasonic Sonochemistry. 2009; 16 (2): 205–208.

114. Tian G, Fu H, Jing L, Tian C. Synthesis and photocatalytic activity of stable nanocrystalline TiO_2 with high crystallinity and large surface area. J. Hazard. Mater. 2009; 161 (2–3): 1122–1130.

115. Geng J, Yang D, Zhu J, Chen D, Jiang Z. Nitrogen-doped TiO_2 nanotubes with enhanced photocatalytic activity synthesized by a facile wet chemistry method. Mater. Res. Bull. 2009; 44 (1): 146–150.

116. Gomes Silva C, Wang W, Faria JL. Photocatalytic and photochemical degradation of mono-, di- and tri-azo dyes in aqueous solution under UV irradiation. Journal of Photochemistry and Photobiology A: Chemistry 181 (2006) 314–324

117. Sa J, Alcaraz Aguera C, Gross S, Anderson JA. Photocatalytic nitrate reduction over metal modifed TiO_2. Appl. Catal. B: Environmental. 2009; 85 (3–4): 192–200.

118. Garcia JC, Simionato JI, Carli da Silva AE, Nozaki J, Evelazio de Souza N. Solar photocatalytic degradation of real textile effluents by associated titanium dioxide and hydrogen peroxide. Sol. Energy. 2009; 83 (3): 316–322.

119. Dozzi MV, Selli E. Specific Facets-Dominated Anatase TiO_2: Fluorine-Mediated Synthesis and Photoactivity. Catalysts. 2013; 3 (2): 455–485.

120. Year 10 chemspace. Nano-properties. Available at: http://blogs.tps.vic.edu.au/year10chemspace/nano-properties/. 24. 07. 2013.

121. Hanaor DAH, Chironi I, Karatvhevtseva I, Triani G, Sorrell CC. Single and mixed phase TiO_2 powders prepared by excess hydrolysis of titanium alkoxides. Adv. Appl. Ceram. 2012; 111 (3): 149–158.

122. Jimenez AE, Santiago SG. Structural and optoelectronic characterization of TiO_2 films prepared using the sol–gel technique. Semicond. Sci. Technol. 2007; 22: 709–719.

123. Penn RL, Banfield JF. Formation of rutile nuclei at anatase {112} twin interfaces and the phase transformation mechanism in nanocrystalline Titania. Am. Mineral. 199; 84: 871–876.

124. Wang CC, Ying JY. Sol-Gel Synthesis and Hydrothermal Processing of Anatase and Rutile Titania Nanocrystals. Chem. Mater. 1999; 11 (11): 3113–3120.

125. Nolan NT, Seery MK, Pillai SC. Spectroscopic Investigation of the Anatase-to-Rutile Transformation of Sol-Gel-Synthesized TiO_2 Photocatalysts. J. Phys. Chem. C. 2009; 113 (36): 16151–16157.

126. Tian G, Chen Y, Zhou W, Pan K, Tian C, Huanf X, Fu H. 3D hierarchical flower-like TiO_2 nanostructure: morphology control and its photocatalytic property. CrystEngComm. 2011; 13 (8): 2994–3000.

127. Marques RRN, Sampaio MJ, Carrapico PM, Silva CG, Morales-Torres S, Dražić G, Faria JL, Silva AMT. Photocatalytic degradation of caffeine: Developing solutions for emerging pollutants. Catal. Today. 2013; 209: 108–115.

128. Saadoun L, Ayllon JA, Jimenez-Becerril J, Peral J, Domenech X, Rodriguez-Clemente R. Synthesis and photocatalytic activity of mesoporous anatase prepared from tetrabutyammonium-titania composites. Mater. Res. Bull. 2000; 35 (2): 193–202.

126. Bitenc M, Horvat B, Likozar B, Dražić G, Crnjak Orel Z. The imapct of ZnO load, stability and morphology on the kinetics of the photocatalytic degradation of caffeine and resazurin. Appl. Catal. B: Environmental. 2013; 136–137: 202–209.

130. Cho CH, Han MH, Kim DH. Morphology evolution of anatase TiO_2 nanocrystals under a hydrothermal condition (pH=9.5) and their ultra-high photocatalytic activity. Mat. Chem. Phys. 2005; 92 (1): 104–111.

131. Lei Y, Liu H, Xiao W. First principles study of the size effect of TiO_2 anatase nanoparticles in dye-sensitized solar cell. Modelling Simul. Mater. Sci. Eng. 2010; 18: 025004–025013.

132. Yang HG, Sun CH, Qiao SZ, Zou J, Liu G, Smith SC, Cheng MH, Lu GQ. Anatase TiO_2 single crystals with a large percentage of reactive facets. Nature. 2008; 453: 638–641.

133. Popović S, Skoko Ž, Gajović A, Furić K, Musić S. X-Ray diffraction study of thermal properties of titanium dioxide. Fizika A. 2005; 14 (1): 19–28.

134. Wang X, Caruso RA. Enhancing photocatalytic activity of Titania materials by using porous structures and the addition of gold nanoparticles. J. Mat. Chem. 2011; 21 (1): 20–28.

135. Collins A, Carriazo D, Davis SA, Mann S. Spontaneous template-free assembly of ordered macroporous titania. Chem. Commun. 2004; 568–569.

136. Yu BJ, Su Y, Cheng B. Template-Free Fabrication and Enhanced Photocatalytic Activity of Hierarchical Macro-/Mesoporous Titania. Adv. Funct. Mater. 2007; 17: 1984–1990.

137. Wang X, Yu JC, Ho C, Hou Y, Fu X. Photocatalytic Activity of a Hierarchically Macro/Mesoporous Titania. Langmuir. 2005; 21 (6): 2552–2559.

138. Yang B, Zhang P, Savage DE, Lagally MG. Self-organization of semiconductor nanocrystals by selective surface faceting. Phys. rev. B. 2005; 72: 2354131–2354134.

Index of Figures

Index of Tables

Index of Procedures

Appendix

ARTICLES AND OTHER COMPONENT PARTS

Original scientific article

Bitenc M, Horvat B, Likozar B, Dražić G, Crnjak Orel Z. The impact of ZnO load, stability and morphology on the kinetics of the photocatalytic degradation of caffeine and resazurin. App. Catal. B: Environmental. 2013; 136/137: 202–209.

Horvat B, Rečnik A, Dražić G. The growth of anatase bipyramidal crystals during hydrothermal synthesis. J. Cryst. Growth. 2012; 347: 19–24

Horvat B, Dražić G. Flower and coral-like hierarchically structured TiO_2 prepared by hydrothermal synthesis. Article to be published.

Published scientific conference contribution abstract (invited lecture)

Dražić G, Horvat B, Krivec M, Abram A. Photocatalytic TiO_2 - from hierarchical structures to a microreactor. V: 4rd IC4N - 2013, 4rd International Conference from Nanoparticles & Nanomaterials to Nanodevices and Nanosystems and NanoTechnology Transfer Workshop on: from the Lab to the Marketplace. 16-20 June 2013. Corfu, Greece. Book of abstracts. 2013; 32.

Published scientific conference contribution abstract

Horvat B, Dražić G. Anatase, brookite, rutile. V: Lisjak D (ur.), Dušak P (ur.), Kralj S (ur.), 7th Young Researchers' Day. 19 February 2013. Ljubljana, Slovenia. Program and abstract book. 2013; 34.

Horvat B, Rečnik A, Dražić G. Hydrothermal growth of anatase. V: Mihailović D (ur.), Kobe S (ur.), Kaučič V (ur.), Osterman N (ur.), Novak Tušar N (ur.), Žužek Rožman K (ur.), Šturm S (ur.). SLONANO 2012. 24-26 October 2012. Ljubljana, Slovenia. Book of abstracts. 2012; 27.

Horvat B, Rečnik A, Dražić G. The growth of TiO_2 anatase during hydrothermal synthesis. V: Žagar K (ur.), Lenart A (ur.), Pečko D (ur.). 6th Young Researchers' Day 2012. 27-28 Febraury 2012. Ljubljana, Slovenia. Program and abstract book. 2012; 32.

Horvat B, Dražić G. All three naturally existing TiO_2 crystals synthesized solvothermally. V: Godec M (ur.), Donik Č (ur.), Paulin I (ur.), Kocijan A (ur.). 20. jubilejna konferenca o materialih in tehnologijah. 17-19 October 2012. Portorož, Slovenija. Program and abstract book. 2012; 68.

Horvat B, Dražić G. Photocatalytic activity of sol-gel and hydrothermally prepared anatase. V: Abstracts: PAOT. Photocatalytic and Advanced Oxidation Technologies for Treatment of Water, Air, Soil and Surfaces. 4-8 July 2011. Gdansk, Poland. 2011; 149.

Horvat B, Krivec M, Dražić G. Comparison of hydrothermal and sol-gel synthesis of nano-anatase TiO_2 with additives. V: EMAS 2011. 12th European Workshop on Modern Developments and Applications in Microbeam Analysis. 15-19 May 2011. Angers, France. Book of tutorial and abstracts. 2011; 354.

Horvat B, Dražić G. Transmission electron microscopy study of TiO_2 anatase crystal morphology prepared by hydrothermal synthesis. Presented at Microscopy & Microanalysis 2011, 69th Annual Meeting of the Microscopy Society of America, 45th Annual Meeting of the Microanalysis Society, 44th Annual Meeting of the International Metallographic Society. 7-11 August 2011. Nashville, Tennessee, USA. Microscopy and Microanalysis. 2011; 1700–1701.

Horvat B, Krivec M, Dražić G. Primerjava hidrotermalne ter sol-gel sinteze nanoanataza TiO_2. V: Pribošič I (ur.), Krnel K (ur.). 5. dan mladih raziskovalcev. Ljubljana. February 2011. Program and abstract book. 2011; 55.

Verhovšek D, Kovačec U, Horvat B, Čeh M. Hidrotermalna sinteza TiO_2 nanodelcev in njihova uporaba v pastah za fotoelektrokemijske sončne celice = Hydrothermal synthesis of TiO_2 nanoparticles used for paste preparation for photoelectrochemical solar cells. V: Kravanja Z (ur.), Brodnjak-Vončina D (ur.), Bogataj M (ur.). Slovenski kemijski dnevi 2011. Portorož, 14-16 September 2011. Book of abstracts. 2011; 73.

Horvat B, Rečnik A, Dražić G. Microstructural investigation of hydrothermally prepared TiO_2 anatase, V: Su DS (ur.), Wrabetz S (ur.), Zhu B (ur.). International Symposium on Advanced Electron Microscopy for Catalysis and Energy Storage Materials. 17-20 January 2010. Berlin, Germany. Booklet of abstracts. 2010; 4.

Horvat B, Krivec M, Dražić G. Comparison of hydrothermal and sol-gel synthesis of nanoanatase TiO_2 = Primerjava hidrotermalne ter sol-gel sinteze nano-anataza TiO_2. V: Jenko M (ur.). 18. konferenca o materialih in tehnologijah = 18th Conference on Materials and Technology. Portorož, Slovenia. 15-17 November 2010. Program and abstract book. 2010; 47.

Krivec M, Horvat B, Dražić G. Preparation and photocatalytic properties of TiO_2 based microreactors = Priprava in fotokatalitične lastnosti mikroreaktorjev na osnovi TiO_2. V: Jenko M (ur.). 18. konferenca o materialih in tehnologijah = 18th Conference on Materials and Technology. 15-17 November 2010. Portorož, Slovenia. Program and abstract book. 2010; 49.

Horvat B, Rečnik A, Dražić G. Mikrostrukturna raziskava hidrotermalno sintetiziranega TiO_2. V: Kuščer D (ur.), Perc B (ur.). 4. Dan Mladih Raziskovalcev KMBO. Ljubljana, Slovenija. 11 February 2010. Program and abstract book. 2010; 40.

Horvat B, Dražić G. Crystalisation and shaping of TiO_2 anatase. V: International School of Crystallization 2010, ISC Granada. Granada, Spain. 24-28 May 2010. Program, abstract book, notebook, list of participants. 2010; 96.

Horvat B. Infiltrati fotokatalitičnega TiO_2. V: Kaluža B (ur.), Eleršič K (ur.), Pogorelc B (ur.), Šetina B (ur.), Vahčič M (ur.). 2. študentska konferenca Mednarodne podiplomske šole Jožefa Stefana = second Jožef Stefan International Postgraduate School Students Conference. 27 May 2010. Ljubljana, Slovenia. Abstract book. 2010; 52.

Horvat B, Rečnik A, Dražić G. Microstructural investigation of TiO_2 nano-atanase grown

under hydrothermal conditions. V: Mihailović D (ur.), Dominko R (ur.), Vilfan M (ur.). SLONANO 2009. 19-21 October 2009. Ljubljana, Slovenia. Book of abstracts. 2009; 95.

Horvat B, Silva AMT, Dražić G, Drnovšek N, Novak S. Meritve fotokatalitične aktivnosti TiO_2. V: Iskra J (ur.), Milošev I (ur.). 3rd Young Researchers' Day 2009. Ljubljana, Slovenia. 2009; 1.

Horvat B, Rečnik A, Dražić G. Hydrothermal synthesis of different shapes of nanoanatase TiO_2 = Hidrotermalna sinteza nanoatanaza TiO_2 različnih oblik. V: Jenko M (ur.). 17. konferenca o materialih in tehnologijah. 16-18 November 2009. Portorož, Slovenija. Program and abstract book. 2009; 54.

Horvat B, Dražić G. Rast fraktalov z DLA in fotokatalizo TiO_2. V: Šetina B (ur.), Junkar I (ur.), Kaluža B (ur.), Eleršič K (ur.). 1. študentska konferenca Mednarodne podiplomske šole Jožefa Stefana = first Jožef Stefan International Postgraduate School Student's Conference. 19-20 May 2009. Ljubljana, Slovenia. Abstract book. 2009; 22–23.

Horvat B, Drnovšek N, Rade K, Novak S, Dražič G. Preparation of nano-anatase TiO_2 = Priprava nano-anataza TiO_2. V: Jenko M (ur.). 1. mednarodna konferenca o materialih in tehnologijah pod pokroviteljstvom FEMS in IUVSTA = first International Conference on Materials and Technology sponsored by FEMS and IUVSTA. 13-15 October 2008. Portorož, Slovenia. Program and abstract book. 2008; 1.

MONOGRAPHS AND OTHER COMPLETED WORKS

Undergraduate thesis

Horvat B. Očem varni LIDAR: diplomsko delo. Ljubljana, Slovenia. 2008.

PERFORMED WORKS (EVENTS)

Unpublished conference contribution

Horvat B, Dražić G. Properties and microstructural investigation of TiO_2 nanoparticles, prepared by hydrothermal synthesis. Presented at EUROMAT 2009, European Congress on Advanced Materials and Processes. 7-10 September 2009. Glasgow, United Kingdom. 2009.